



EDEMOM

European Doctorate in Electronic Materials, Optoelectronics and Microsystems

XXV cycle

# STUDIES OF NANOSTRUCTURED MATERIALS FOR DYE SENSITIZED SOLAR CELLS (DSSC) ELECTRODES

Serena Gagliardi

University Supervisor: Prof. Gennaro Conte

ENEA Supervisors: Dr. Rossella Giorgi  
Dr. Mauro Falconieri

June 2013

## ABSTRACT

Exploitation of solar irradiation, in particular by development of photovoltaic technologies, is a widely recognized target for renewable energy production. Present R&D trends span from highly efficient expensive devices for aerospace industry to less efficient cheap devices for building integration. In last contest, where the coverage of buildings or greenhouses requires versatile shapes and colours and low production costs, the so-called Dye Sensitized Solar Cells (DSSC) have attracted a particular interest, starting from the publication of the seminal paper of Gratzel and O'Reagan in 1991. A DSSC is a photoelectrochemical system, as the ones studied since 1960s, based on a dye sensitized semiconductor, where a nanostructured high specific surface area porous titania electrode was introduced as a turning point to reach energy conversion up to 11%. The development of the photoanode functionality, depending on both the porous semiconductor and the dye, is one of the keys to improve the efficiency of DSSC. The research is directed on one side to the synthesis of highly absorbing dyes over a wide spectral range; on the other side to the development of novel semiconductor nanostructures providing better optical and electronic transport properties. Electrodes with the high specific surface necessary for efficient dye anchorage are usually produced by sinterization of titania nanobeads. However, several different shapes and morphologies are under investigations, in order to overcome the poor electron conduction characteristics of this kind of anodes. In particular, well-ordered vertically aligned titania nanotubes have been proposed, thanks to the long electron diffusion length predicted for this geometry. In parallel, research is in progress with the aim of producing sustainable devices based on widely available and cheap materials, focussing on the cathode. The last is a conductive surface functionalized with Pt nanoclusters, enabling both electron conduction and catalysis of the reduction reaction occurring in the iodine-based electrolyte that provides electrochemical carrier transport in the device. Since carbon is known to be a catalyst for the iodine reduction, several efforts are devoted to exploit carbon based catalysts for Pt substitution at the DSSC cathode.

This thesis deals with the study of DSSC photoanodes based on different nanostructured titania morphologies, and novel carbon-based cathode nanomaterials.

To this purpose, the procedure to fabricate small lab-scale devices based on both commercial and novel materials was set-up, and the devices were routinely characterized by current-voltage measurements under AM1.5 standard illumination. Moreover, a great effort was devoted to the standardization of the protocols to prepare photoanodes and cathodes, and to assemble the complete device, in order to allow meaningful comparison of performances.

As novel material for the cathode, carbon nanostructures were made on purpose by CVD on different substrates, characterized, and then tested in complete devices. The efficiency of the cells with carbon-based cathodes is still low compared to those obtained with standard materials, and work is in progress in order to synthesize carbon nanostructures with improved catalytic performance.

For the study of photoanodes, a simple model, based on geometrical considerations, was developed in order to calculate the specific surface of both conventional spherical nanoparticles -based electrodes, and new photoanodes based on tubular nanostructures (titania nanotubes, TNT). The knowledge of the specific surface enables to estimate the dye (N719) load on the electrode and then, neglecting light diffusion phenomena as a first approximation, the photoanode optical absorption. From the absorption of the electrode is finally possible to estimate the short circuit current density under standard solar illumination. To take into account the light diffusion in the mesoporous film, an absorption enhancement factor was considered. In order to calculate the maximum achievable short circuit current density, a statistical ray approach was used to simulate the case of limit light trapping. In parallel, the experimental measure of the diffuse and collinear optical transmittivity and reflectivity of a NP-based electrode enabled quantification of the real enhancement factor of the absorption coefficient as a function of the wavelength.

The experimental values of the short circuit current density, obtained by measuring the characteristics of a complete cell, were discussed and compared to the values predicted by applying the optical model.

Novel photoanodes based on titania TNT grown on transparent electrodes (fluorine doped tin oxide coated glasses, FTO) were prepared and tested in complete cells. A large bibliography shows the possibility to grow by electrochemical process titania TNT with controlled variable morphologies, up to tens of microns of length from titanium foils. Nevertheless, in order to fully exploit the solar irradiation, growth of TNT on FTO is mandatory. For this purpose, different electrochemical conditions were applied to synthesize TNT from Ti films sputtered on FTO. Tubular structures were easily produced, but the interface Ti-FTO is severely damaged by the anodization process, so that film peeling remains a challenge for most of the conditions. TNT films up to 3.5  $\mu\text{m}$  thick were obtained in carefully chosen anodization conditions and tested as photoanodes in real cells, showing, however, conversion efficiency lower than that attainable from standard NP-based devices.

In conclusion, small lab-scale DSSC, based both on conventional and novel materials, have been fabricated and characterized. The performances of devices using cathodes based on carbon nanostructures were measured, pointing out the necessity of improving the catalytic properties, in order to reach the standard Pt nanoparticles characteristics. The optical functionality of photoanodes was assessed. The light scattering properties of practical photoanodes were experimentally quantified and related to illuminated IV characteristics of real cells. Several photoanodes were realized by electrochemical processing of Ti films on FTO, and used to assembly complete devices. Complete characterizations of the cells, jointly with the optical model, pointed out the necessity of overcoming the technological bottlenecks in the anodization process, in order to produce high specific surface morphologies.

## OUTLINE

*Chapters 1 and 2* introduce the photovoltaic principles and the current state of the art, mainly focusing on Dye Sensitized Solar Cells and related materials.

Chapters 3 to 6 report the experimental results obtained in:

*Chapter 3* assembling and characterizing standard devices on the lab scale.

*Chapter 4* synthesis and characterizations of carbon-based counter electrodes, their application in DSSC and the device characterization, after the review of the inherent literature.

*Chapter 5* optical modelling and the characterizations. After a brief introduction to the photophysics of active layers and light management strategies based on light trapping. The optical functionality of photoanodes in DSSC is discussed-

*Chapter 6* optical modelling, synthesis and characterizations of photoanodes based on TiO<sub>2</sub> nanotubes. The I-V characteristics of devices based on the novel electrodes are reported and discussed.

## CONTENTS

Chapter 1. Photovoltaic technology .....	8
1.1. Motivation for photovoltaic.....	8
1.2. Solar irradiation .....	10
1.3. Photovoltaic devices: operating principles and characteristics .....	11
1.4. Present status of pv manufacturing.....	15
1.5. Material availability at tw/yr manufacturing .....	31
1.6. Future outlook .....	31
Chapter 2. Dye sensitized solar cells .....	34
2.1 structure and working principle.....	34
2.1. Dssc materials.....	39
2.2. Advantages of the dsscs.....	46
Chapter 3. Practical cell assembly and characterization.....	48
3.1. Device components.....	48
3.2. Device assembly and sealing.....	54
3.3. Cell characterization .....	55
Chapter 4. Carbon nanostructures as cathode materials .....	58
4.1. State of the art.....	58
4.2. Synthesis and characterization of carbon nanowalls .....	70
4.3. Device characterization .....	79
4.4. Discussion.....	82
Chapter 5. Photophysics of conventional anodes .....	84

5.1. Theoretical background and review .....	84
5.2. Photoanode optical functionality .....	91
5.3. Discussion.....	101
Chapter 6. Unconventional photoanode .....	103
6.1. State of the art and motivations .....	103
6.2. Optical modelling of nanotubes photoanode .....	105
6.3. Titania nanotubes synthesis and characterization.....	108
6.4. Device characterizations.....	111
6.5. Discussion.....	113
List of achronyms .....	116
References .....	117
List of publications and conference presentations .....	127

# Chapter 1. Photovoltaic technology

*This chapter explains the motivations of the efforts that modern research activity spends for the development of photovoltaic technology. After recalling the main concepts relative to solar irradiation and device operation, the different technologies on the PV field are briefly introduced and compared, pointing out bottlenecks and sketching possible developments.*

## 1.1. MOTIVATION FOR PHOTOVOLTAIC

All the energy used in the world, with the only exception of nuclear energy and, partly, of the geothermal energy, rises from the sun. Also when fossil fuels are used, we use solar energy accumulated for ages through photosynthesis and subsequent biological and chemical processes.

At present, the global power consumption currently stands at approximately 15 TW, the vast majority of which is generated by the combustion of fossil fuels. The associated release of CO<sub>2</sub> from these anthropogenic sources has dramatically altered the composition of the atmosphere and may detrimentally impact global temperature, sea levels and weather patterns.

The terawatt challenge is the effort to supply up to 30 TW of carbon-free power by the mid-21st century. While all renewable resources will be important, only solar can meet this level of demand, because the practical global potential of other renewable energy sources such as wind, hydroelectric, bio-mass, and geothermal is estimated to be less than 10 TW (Lewis 2007).



Assuming that all this power will be supplied by photovoltaic (PV) panels with 30 year lifetimes, this translates into PV production rates of  $\sim 1$  TW/yr. Solar energy, up to 600TW, may be harvested through its conversion to heat (solar thermal), electrons (PV), or chemicals (solar fuels).

Solar photovoltaics has been growing at an average rate of  $>40\%/yr$  over the past decade, with annual shipments exceeding 8 GW in 2009 and a dramatic increase in the following years: at the end of 2011, when more than 69 GW of photovoltaics were installed worldwide and at the end of 2012, when this amount has risen to 101 GW.

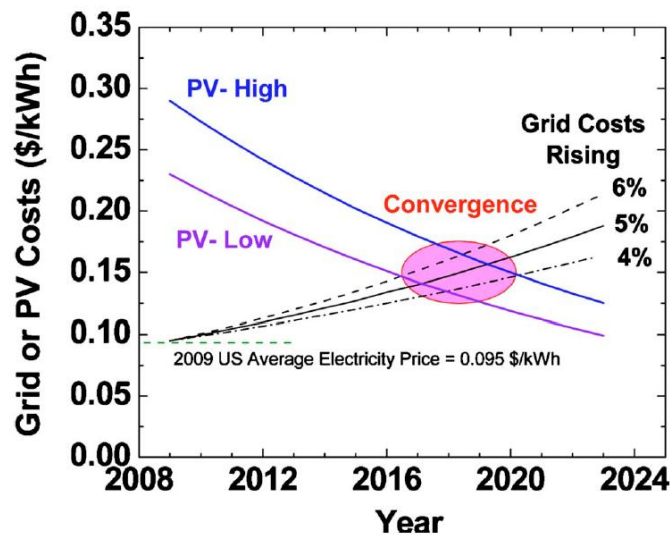


Fig. 1.1. Projected convergence of the cost of electricity produced by PV and the conventional grid prices (Wolden et al. 2011).

Figure 1.1 compares the cost of solar electricity with that produced by conventional sources. In 2009, the average cost of grid-supplied electricity in the United States was 9.5 ¢/kWh, and this value will continue to rise due to increased demand or at potentially higher rates if measures such as carbon taxation are introduced. The current price of electricity generated using solar cells remains two to three times greater than grid-supplied electricity, but PV costs continue to decrease. A crossover, commonly called “grid parity”, is expected during this decade. We note that projected grid parity does not require any technological

breakthroughs but is simply an extrapolation of the learning curve that the PV industry has been following for several decades, along with the inevitable increase in the cost of fossil fuel derived electricity (Surek 2005).

Despite this amazing success, PV manufacturing must be further expanded by two orders of magnitude to TW/yr production levels in order to transform our society from one that relies on burning fossil fuels to one that uses sustainable energy sources. The challenge is daunting, but the opportunities are equally boundless. The sun continuously provides power to the planet with an average flux of  $1000 \text{ W/m}^2$ . If one assumes 10% net conversion efficiency (generation, transportation, and storage),  $\sim 10^{12} \text{ m}^2$  would be required to supply 30 TW of clean energy.

## 1.2. SOLAR IRRADIATION

Sun can be approximated to a black body at the temperature of 5800 K, so its irradiation spectrum can be described by Planck's distribution. As it passes through the atmosphere, solar radiation is attenuated by scattering and absorption; the more atmosphere through which it passes, the greater is attenuation. The air mass coefficient defines the direct optical path length through the Earth atmosphere, expressed as the ratio relative to the path length vertically upwards. If  $L_0$  is the zenith path length of a beam travelling in the atmosphere, and  $L$  is the path length of a beam incident with an angle  $\theta$  relative to the normal to Earth surface, the air-mass (AM) coefficient is defined as

$$AM = \frac{L}{L_0} \approx \frac{1}{\cos\theta}$$

AM0 corresponds to the extraterrestrial radiation, without atmospheric attenuation. Since many of the world's population centres, and hence solar installation industry, lie in

temperature latitude ( $\theta=48^\circ$ ) the standard reference spectrum AM1.5 was chosen as the standard irradiation condition to test solar cells. The 5762K black body radiation and the AM0, AM1.5 solar spectra are reported in Fig. 1.2.

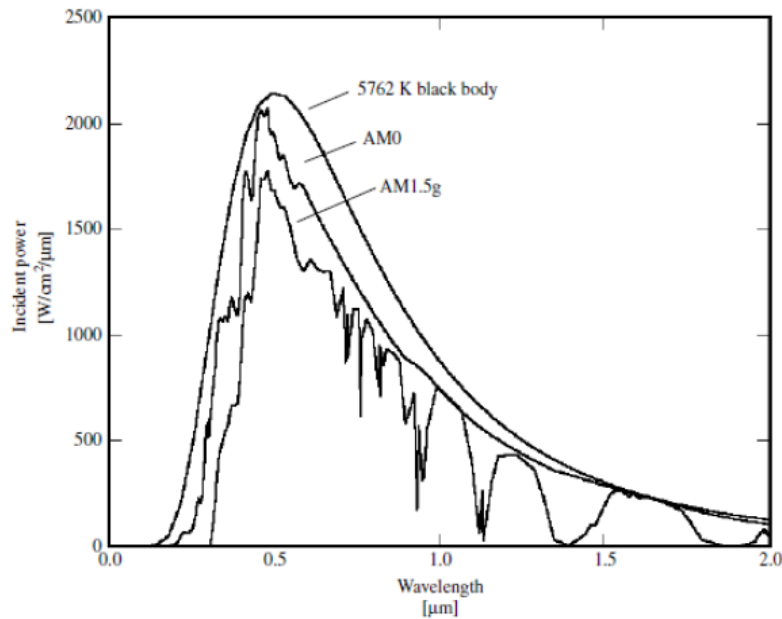


Fig. 1.2. The solar radiation spectra: the 5762 K black body radiation, the extraterrestrial solar (AM0) and the standard terrestrial (AM1.5) (A. Luque, 2003).

### 1.3. PHOTOVOLTAIC DEVICES: OPERATING PRINCIPLES AND CHARACTERISTICS

The first solid-state solar cell was developed at Bell labs in 1954. It was based on a silicon p-n junction. Under illumination, the p-n junction absorbs photons with energy  $h\nu > E_g$  and

electrons from the valence band are excited in the conduction band leaving holes to the valence band; electrons are therefore accumulated in the n-type material and holes in the p-type material, generating photovoltage between the opposite sides of the pn-junction. When the p-n junction is closed on an external load a current flows in the circuit. The main physical processes involved in the operation of a photovoltaic cell are:

- i) light absorption,
- ii) charge separation,
- iii) charge collection.

The physical or chemical processes behind these principal steps vary between different types of solar cells and photovoltaic materials. The efficiency of a solar cell depends on the efficiency of each of the mentioned steps (respectively  $\eta_{LH}$ ,  $\eta_{CS}$ ,  $\eta_{COL}$ ) and is maximized by the materials selection and the cell design.

An ideal p-n junction solar cell is assumed to have ideal I-V diode characteristics; since under illumination the cell generates a constant current ( $I_{SC}$ ) the equivalent circuit of the ideal device is represented in Fig.1.3, where the constant current source is in parallel with the junction. The I-V characteristic of such a device is given by:

$$I = I_{dark} [\exp (-qV/kT-I)] - I_{sc} \quad (1)$$

Where  $q$  is the electron charge,  $T$  the absolute temperature and  $k$  Boltzmann's constant and  $I_{dark}$  the saturation current of diode in dark.

From the I(V) characteristics, the open circuit voltage  $V_{OC}$  results to be:

$$V_{oc} = \frac{kT}{q} \ln \left( \frac{I_{sc}}{I_{dark}} + 1 \right) \approx \frac{kT}{q} \ln \left( \frac{I_{sc}}{I_{dark}} \right) \quad (2)$$

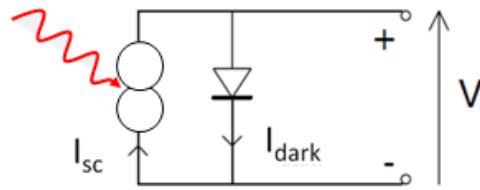


Fig.1.3. Equivalent circuit describing an ideal solar cell under illumination.

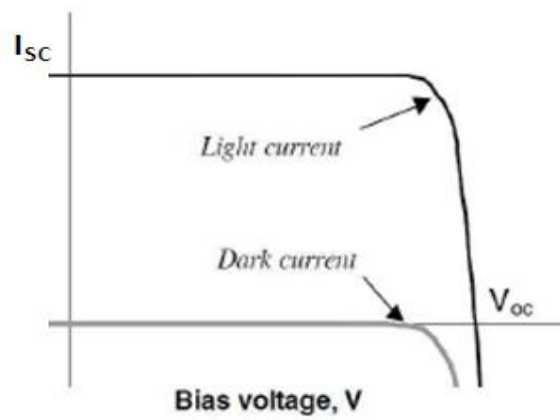


Fig.1.4. Current to voltage characteristic of ideal solar cell in the dark and under illumination.

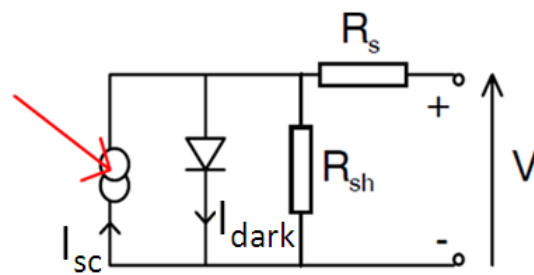


Fig. 1.5. Equivalent circuit of a non-ideal solar cell.

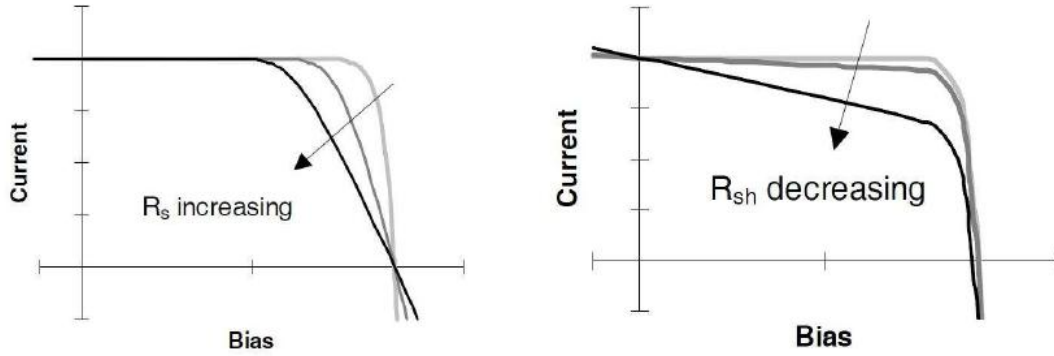


Fig. 1.6. Current voltage characteristics of a non ideal solar cell.

The curve described by equation (2) passes through the fourth quadrant and therefore a power can be extracted. The usual representation is that reported in Fig. 1.4 which is an inversion about the voltage axis. In real cells a fraction of the power is dissipated through the resistance of the contacts and through leakage currents related to shunting paths for the current. These effects are equivalent electrically to two parasitic resistances in series ( $R_s$ ) and in parallel ( $R_{sh}$ ) with the cell (see fig. 1.5) who affect the I-V characteristic as sketched in Fig.1.6.

The external efficiency  $\eta$  of a solar cell in converting light of any arbitrary spectral distribution into useful power is given by

$$\eta = \frac{P_{out}}{P_{in}} = \frac{I_M \cdot V_M}{P_{in}} \quad (3)$$

where  $V_M$ ,  $I_M$  are the voltage and current at the maximum power, as shown in Fig. 1.7.

The power output of a solar cell is given by:

$$P_{out} = V_M \cdot I_M = FF \cdot V_{oc} \cdot I_{sc} \quad (4)$$

where FF is the fill factor that is a measure of the quality of the cell.

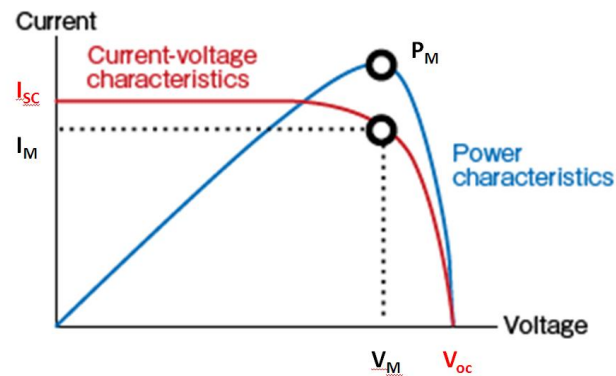


Fig. 1.7. Characteristic of a solar cell, where the relevant PV parameters are indicated.

#### 1.4. PRESENT STATUS OF PV MANUFACTURING

In 2003 various forms of silicon accounted for >99% of the PV market, and manufacturing was lead by Japan and Europe (A. Goetzberger 2003). Today, crystalline silicon (c-Si) still accounts for 85% of the market, but China has become the world's leading manufacturer. Table 1 lists the top 10 crystalline Si manufacturers and their output in 2009 (Mehta 2009).

Rank	Company	Country	2009 module production (MWdc)
1	Suntech Power	China	704
2	Sharp	Japan	595
3	Yingli Green Energy	China	525
4	Kyocera	Japan	400
5	Trina Solar	China	399
6	Sunpower	US	398
7	Canadian solar	Canada	326
8	Solarfun	China	313
9	Solar World	Germany	288
10	Sanyo	Japan	260

**Table 1-1. Top 10 crystalline silicon manufacturers in 2009** (Mehta 2009).

A second major change in the past decade has been the emergence of cadmium telluride (CdTe) thin-film technology, which was a negligible contributor in 2003, but in 2009 its share of the global PV market amounted to 13% production rate. While a part of this market share has come at the expense of c-Si, it has also eroded the foothold of competing thin-film technologies such as amorphous silicon (a-Si:H).

Figure 1.8 displays the champion overall power conversion efficiencies for laboratory solar cells and commercial modules for the established PV manufacturing technologies. In addition to efficiency, materials and manufacturing costs are the greatest levers controlling the cost of solar power. In most cases, the champion cells have seen little or no improvement over the past decade while economies of scale and advances in manufacturing science and technology have fueled the expansion of PV through cost reduction and module performance improvements. Figure 1.8 shows that the PV technologies are at different points in their respective learning curves when compared to the Shockley-Queisser (SQ) limit of  $\approx 33\%$  solar energy conversion efficiency for single junction devices (W. Shockley 1961). Since the band-gap energy dependence of the Shockley-Queisser limit is flat around the maximum, the theoretical efficiency limits for these technologies are only marginally different and are not a deciding factor in their competitiveness with each other. Nevertheless, record single crystal (c-Si) cells have matured to within 90% of their SQ limit, while commercial thin-film modules harvest about 35% of their potential.



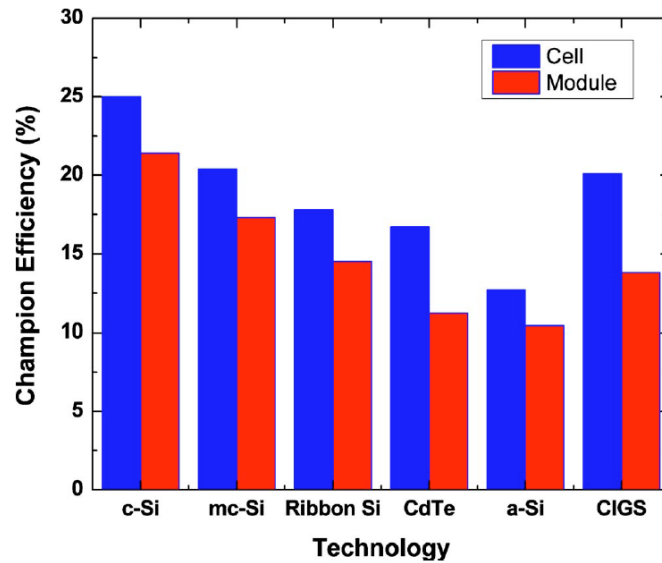


Fig. 1.8. Champion efficiencies reported for cells and commercial modules for the established PV manufacturing technologies (Wolden 2011).

### 1.1.1. Silicon

Silicon is the most developed and well-understood semiconductor in the world, benefiting from decades of development by the integrated circuit (IC) industry. Techniques to control and manipulate its properties are well established. Silicon has proven field stability, and it is the most abundant semiconductor in the world. Multicrystalline silicon (mc-Si) remains the leading PV product, though its market share has ebbed from values as high as 65% earlier in the decade. The combination of higher efficiency, lower polysilicon prices, and improvements in wire cutting technology has reduced wafer thicknesses and kept single crystal (c-Si) silicon competitive. The issues that limit the c-Si technology today remain quite similar to those described by Goetzberger *et al.* in their detailed 2003 review article (A. Goetzberger 2003). The cost of the silicon feedstock remains the biggest lever impacting manufacturing costs. Reducing the cost of silicon is being pursued through a number of avenues including improving the feedstock, the production of kerfless wafers, the development of ultrathin silicon, as well as the use in bifacial cells.

### *Silicon feedstock*

To date, purification techniques for silicon have been dictated by the IC industry, which employs electronic grade silicon with purity levels of less than 1 ppb. A significant shift occurred a few years ago when the PV industry surpassed the IC industry as the largest consumer of refined silicon. Electronic grade silicon is produced primarily using the energy intensive (>120 kWh/kg) Siemens process (G. del Coso 2007). New production strategies such as fluidized bed technology are being investigated, to upgrade metallurgical grade silicon, potentially reducing these energy requirements by up to a factor of 5 (Pizzini 2010). Though less expensive, these techniques often retain higher levels of metals such as Fe and Al than electronic grade silicon. While these impurities would be catastrophic in IC manufacturing, such low levels may be tolerable in solar cells.

### *Kerfless wafers*

Improvements in wire-saw technology have enabled the reduction of wafer thicknesses to 180  $\mu\text{m}$  at present. However, over 50% of the silicon is lost as silicon sawdust or Kerf. While this material can be recycled, it would be desirable if the wire-sawing step could be eliminated. Kerfless wafer could potentially reduce Si use from an industry average of about 6-3 g/W at current wafer thicknesses. Techniques for the direct production of wafers from the melt were invented in the 1970s (Ciszek 1972) (T. F. Ciszek 1982), and after decades of development they have now reached the market. The two closely related techniques are edge-defined film-fed growth (EFG) and string ribbon silicon technologies. The elimination of wafer sawing makes this the most energy efficient mode to produce c-Si, and companies using these methods claim that energy payback times have been reduced to 1 year. The quality of the material produced by these techniques is somewhat inferior to standard block-cast mc-Si but is continuously improving with champion laboratory cells now reaching power conversion efficiencies over 18% while 4.5% efficient modules are already on the market (D. S. Kim 2006) (Schott Solar, Albuquerque, NM, 2010). Passivation of surface and bulk defects is critical to achieving high efficiency, and this is

usually achieved through the deposition of a hydrogen-rich silicon nitride layer, which also serves as an antireflection coating.

#### *Ultrathin silicon*

The term ultrathin silicon (ut-Si) refers to solar cell technology where the photon absorbing silicon layer is on the order of 5-50  $\mu\text{m}$  thick. Because silicon has an indirect band gap, it is often assumed that silicon must be thicker than 100  $\mu\text{m}$  to effectively absorb light (Smestad 2002). However, simulation studies have shown that  $\approx 40$   $\mu\text{m}$  is ideal for obtaining maximum performance (Wolf 1980) (M. J. Kerr 2002). Green's calculations showed that a 19.8% efficient device could be obtained with only 1  $\mu\text{m}$  of single crystal silicon with state-of-the-art surface passivation (Green 1999). If one could produce such materials using a Kerfless process, it would result in an order of magnitude reduction in material cost with respect to today's state-of-the-art wafers: thus, ut-Si would merge the benefits of crystalline silicon with those of thin-film solar cells. Thin silicon is also amenable to use of bifacial architectures, which harvest light from both directions. There are a few general approaches to the fabrication of ut-Si. The first strategy employs heteroepitaxial growth followed by liftoff or removal of a sacrificial substrate. One complication is identifying low-cost substrates with appropriate properties for these types of processes. A related approach involves deposition a-Si directly on glass followed by thermal recrystallization. The third approach involves "peeling" ultrathin silicon layers off of silicon ingots using techniques such as stress-induced liftoff (F. Dross 2007). A new process has been recently introduced where this is achieved through a combination of ion implantation and thermal treatment, producing Kerf-free wafers as thin as 25  $\mu\text{m}$ .

#### *Module efficiency*

While crystalline silicon solar cell science and technology is considered to be mature, there remains room to further enhance its efficiency, particularly at the module level (typical modules fall  $\approx 20\%$  short of record values with respect to both  $V_{oc}$  and  $J_{sc}$ ). Efforts to address this include improvements in front side texturing, integration of back side reflectors, and use of advanced antireflection coatings. Another strategy is to reduce the level of shadowing associated with front contacts by either reducing the linewidths or by

completely eliminating them using back side contacting schemes. Another problem is that the quantum efficiency in the blue region of the spectrum is limited by high absorption and associated recombination in the vicinity of the front emitter. This issue is being addressed through the use of selective emitter designs and improved passivation strategies.

#### *Amorphous and nanocrystalline silicon*

Solar cells based on hydrogenated amorphous silicon (a-Si:H or a-Si) were first reported in 1976 (D. E. Carlson 1976). Silicon layers are deposited by plasma-enhanced chemical vapor deposition (PECVD) using mixtures of  $H_2$  and  $SiH_4$ . Hot-wire chemical vapor deposition has been offered as an alternative but has yet to be implemented in large-scale manufacturing. The addition of dopants to a-Si leads to the creation of additional recombination centers that hinder performance. Because of this effect *p-i-n* device structures are almost always used. Benefiting from synergies with the IC industry, a-Si was rapidly commercialized and the first PV products appeared in the early 1980s. Early devices rapidly surpassed 10% efficiency, but it was quickly recognized that these devices suffered from light-induced degradation through the now well known Staebler-Wronski effect (D. L. Staebler 1977): light exposure leads to a reduction of the solar cell efficiency over months which, eventually stabilizes at efficiencies around 6-7%. Nevertheless, for decades, a-Si was by far the most successful thin-film technology, achieving market shares approaching 10% early in the decade (A. Goetzberger 2003) before falling and being surpassed by CdTe a few years ago.

One of the most attractive features of a-Si is that devices can be deposited at low temperature ( $\leq 200$  °C), enabling the fabrication of lightweight flexible laminates on temperature sensitive substrates. This is a unique trait that provides a competitive advantage in markets such as consumer products and building integrated photovoltaics (BIPV). Though discovered much earlier (Marecek 1968), another major change that has occurred over the past decade is the integration of microcrystalline or nanocrystalline silicon (nc-Si) into device structures. The quality of PECVD deposited material is strongly influenced by the level of silane dilution in hydrogen, and high  $H_2$  dilution levels ( $>90\%$ ) lead to the formation of crystalline domains within the material. The primary advantage of

nc-Si is that it is much less susceptible to the Staebler-Wronski degradation. Another important feature is that a/nc-Si is the only thin-film PV technology that has proven amenable to the formation of multijunction devices. Most commercial devices are based on either tandem cells or even triple junction cells. A common configuration is the "micromorph" tandem, which pairs an a-Si top cell with a nc-Si bottom cell. Solar cells with record efficiencies are based on triple junctions that employ germanium alloys to further improve absorption in the red region of the solar spectrum (J. Yang 1997). A related success story has been the introduction of the a-Si/c-Si heterojunction with intrinsic thin layer (HIT) cell, which boasts 21% conversion efficiency (M. Taguchi 2005). The intrinsic a-Si:H layers appear to be important for passivation of the underlying c-Si material.

### 1.1.2. CdTe

The first reports of CdTe-related PV devices appeared in the 1960s (Cusano 1963), but the development of this technology was fitful, with many stops and starts. The early 1990s saw a flurry of improvement that brought efficiencies to levels that began to attract commercial interest (J. Britt 1993). CdTe has a number of intrinsic advantages as a light absorber. First, its band gap of 1.45 eV is well positioned to harness solar radiation. Its high optical absorption coefficient allows light to be fully captured using only 2  $\mu\text{m}$  of material. Like many II-VI compounds, CdTe sublimes congruently: it vaporizes homogeneously and the compound's thermodynamic stability makes it is nearly impossible to produce anything other than stoichiometric CdTe (Cusano 1963). Thus, simple evaporation processes may be used for film deposition.

Standard CdTe-based devices employ a superstrate configuration: production begins with a glass substrate followed by the successive deposition of the transparent conducting oxide (TCO,  $\text{SnO}_2\text{:F}$ ), the n-type window layer (CdS), the *p-type* CdTe absorber, and finally the back contact (ZnTe/Cu/C). With low manufacturing costs established, the biggest opportunities for CdTe lie in the improvement of device efficiency. Champion cells (Fig. 1.8) convert just over 50% of their SQ potential, while commercial modules are at  $\approx 11\%$

power conversion efficiency. Improving efficiency will require enhancements in both current and voltage. The former is perhaps the most straightforward route, as much of the blue region of the solar spectrum is absorbed in the TCO and CdS layers that make up the front contact. Top laboratory cells have replaced the FTO with advanced TCOs such as cadmium stannate (Wu 2004) and ITO (Compaan A. D. 2004). The more daunting challenge is improving the voltage. The open-circuit voltage ( $V_{oc}$ ) of champion CdTe cells is below that of similar band-gap PV materials. For example, the best  $V_{oc}$  obtained in CdTe is 230 mV shorter of GaAs devices that have a similar band gap. Short carrier lifetimes are at the root of this limitation. The combined effect of defects and grain boundaries limits minority carrier lifetimes in polycrystalline CdTe to a few nanoseconds even in the best devices. These lifetimes are very short compared to almost 1  $\mu$ s for epitaxial CdTe or hundreds of nanoseconds for copper indium gallium diselenide (CIGS). Sites and Pan (J. Sites 2007) showed through simulation that increasing the carrier lifetime or the use of a *p-i-n* device structures may be two viable routes to increase the efficiency to above 20%. A number of fundamental questions must be solved for CdTe PV to move beyond current records and approach 20% efficiency.

A final issue to be mentioned with respect to large-scale CdTe manufacturing is perceptions with respect to both cadmium toxicity and tellurium availability. The toxicity issue appears to be one of the public perceptions. Cadmium is indeed a toxic element, but the risk of exposure once incorporated into PV modules is minimal. Testing of module fate during fires, following standard protocols from the Underwriters Laboratory and the American Society of Testing Materials, showed that Cd emissions during fires are negligible as Cd is encapsulated in the glass-glass structure of the modules. Also early testing of leaking of Cd from broken CdTe modules has shown concentrations of the element in water collected over the course of a year to be below drinking water threshold (Steinberger 1998). Additional testing may be needed as module designs have changed since the 1990s. To their credit, all CdTe manufacturers are committed to 100% ownership of recycling, which in part is related to the issue of Te availability. One also notes that Cd will continue to be produced as a natural by-product of Zn mining. Perhaps the best

argument for CdTe PV is that it serves as a means to sequester this element in an environmentally beneficial manner.

### 1.1.3. CIGS

The first copper chalcopyrite PV devices were introduced in 1976 in the form of copper indium diselenide ( $\text{CuInSe}_2$  or CIS) by Kazmerski *et al.* (Kazmerski L. L. 1976) CIS has a band gap of 1 eV. However, the band gap may be continuously engineered over a very broad range (1-2.5 eV) by substituting either Ga for In or S for Se. The abbreviation CIGS is now used to describe this material as current manifestations often involve either four or all five elements. Much like CdTe, the development CIGS followed a combination of starts and stops. The early 1990s brought a rapid succession of improvements that elevated device efficiencies to over 16% (L. Stolt 1993) (A. M. Gabor 1994). While most PV technologies have recorded little or no improvement in champion cell performance over the past decade, CIGS has continued a steady advance and recently-crossed the 20% threshold, making it the clear efficiency-leader among thin-film technologies (M. A. Green 2010). Substrates include soda lime glass, metal foils, or high-temperature polyimide. The latter has garnered substantial interest for applications such as BIPV and portable power. In the case of deposition on flexible substrates it is critical to match the coefficient of thermal expansion, with highest efficiencies obtained on titanium and stainless steel foils. The insulating nature of PI is advantageous for monolithic integration, but process temperatures are limited to  $<450^\circ\text{C}$ , which limits efficiency.

The basic structure of the CIGS device is quite similar across manufacturers. Fabrication begins with the deposition of a Mo back contact followed by the p-type CIGS absorber (1-3  $\mu\text{m}$ ), a thin buffer layer (50-100 nm), with doped ZnO serving as the transparent front contact. Here the similarities end. The approaches to CIGS fabrication may be classified into three basic categories: coevaporation, selenization/sulfurization of metal films, and nonvacuum techniques (M. A. Contreras 1999) (K. Ramanathan 2005) (C. J. Hibberd 2010).

The nonvacuum strategies may be further divided into electrodeposition, particulate deposition, and solution processes. Electrodeposition has been around for decades and achieved cell efficiencies as high as 13.8% (Lincot et al. 2004), but concerns about up-scaling have limited commercial interest. The particulate route is currently the most actively pursued, with variations employing particles composed of CIGS, metal, metal oxides, and/or metal selenides.

#### *Material chemistry*

With five elements and numerous binary and ternary phases, the CIGS system presents much greater complexity than the PV technologies described previously. Extensive theoretical work has made great advances in understanding the electronic structure and role of defects in this system. These studies have been aided by improvements in advanced characterization techniques. Raman and time resolved photo-luminescence are becoming useful for identifying the presence of secondary phases and certain defects (M. A. Contreras 1999). It is well known that sodium plays a critical role in the morphology and electronic properties of CIGS. Some concerns remain about the use of ZnO as the front TCO and its potential impact on long-term device stability. Moisture exposure is particularly detrimental both to the TCO and the heterojunction itself. Encapsulation in glass partially alleviates this effect, but further development of transparent ultrabarrriers is required to improve the long-term stability of flexible CIGS solar cells. (G. L. Graff 2004). A longer-term concern is the availability and price of In. Recycling of this metal will alleviate constraints on CIGS long-term production, but research is needed to develop technologies for efficient and low-cost recycling of all the elements from the CIGS modules. The possibility of substituting indium/gallium with earth abundant alternatives such as zinc/ tin is discussed below.

#### **1.1.4. Organic photovoltaics**

Carbon is abundant, and the potential for high volume manufacturing of flexible photovoltaics has spurred extensive efforts to develop solar cells using organic semiconductors. Figure 1.9 charts the progress of champion cell efficiencies for the past 15



years. While most technologies have been relatively stagnant in their champion efficiency, organic PV has made great strides in the past decade, with Heliatek and Konarka being the current champions, each with devices certified at 8.3% (Heliatek 2010) (Konarka 2010). OPV devices are comprised of a heterojunction between an electron donor molecule (e.g., poly(3-hexylthiophene) or copper phthalocyanine) and an electron acceptor molecule (e.g., C60 or its derivatives such as phenyl-C61-butyric acid methyl ester). The essentially limitless varieties of candidate organic semiconductor materials may be categorized, as either solution processable (polymers, dendrimers, oligomers, or small molecules) or vacuum deposited (small molecules or oligomers). Although superficially similar to inorganic *p-n* junctions, the OPV junction is fundamentally different. Instead of directly creating an  $e^-/h^+$  pair, photon absorption produces an exciton, an uncharged excited state that must diffuse to a donor/acceptor interface in order to dissociate into a free  $e^-/h^+$  pair. In organic materials the exciton can typically diffuse only 5-10 nm before decaying to the ground state, a problem that limits performance and is typically referred to as the exciton bottleneck. There are two ways to deal with this. One can make a multilayer device that uses very thin donor/acceptor layers such that a majority of excitons can diffuse to a heterojunction interface. Otherwise, one can reduce the distance the exciton has to diffuse before reaching the heterojunction by mixing the donor and acceptor materials on a nanometer length scales to form a single-layer interpenetrating network called a bulk heterojunction. This approach is commonly used in solution-processable materials.

In the OPV device structure, the heterojunction active layer(s) is (are) sandwiched between a set of contact electrodes, with buffer layers likely to be present. In the bulk heterojunction approach an asymmetry in the device must be imposed by either using electrodes with different work functions (typically a front TCO contact modified with a conducting polymer poly(3,4-ethylenedioxythiophene) poly-(styrenesulfonate) and a back contact metal of Ca or Al) or by inserting a buffer layer that blocks carriers from leaving one side of the device. An oxide buffer layer is commonly inserted to block holes from leaving the device through the front TCO contact, which inverts the direction of operation of the device and allows the use of a high work function Ag back contact. In the vacuum

deposited multilayer approach, co-doping of buffer layers has been used to great effect to produce a true *p-i-n* structure that obviates the need for a mismatch in the contact work functions.

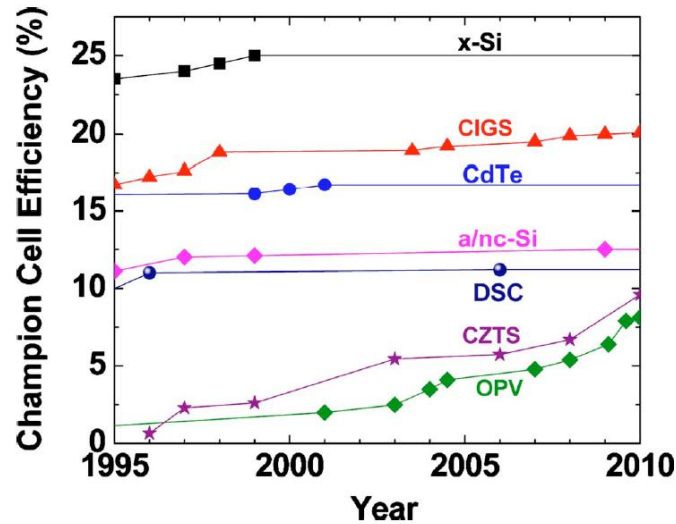


Fig 1.9. Evolution of champion cell efficiencies since 1995 for various PV technologies (Wolden et al. 2011).

There are several challenges to improve the efficiency of organic solar cells (Brabec C. J. 2010) (H. Spanggaard 2004). These are being addressed through the development of novel donor and acceptor materials, new buffer layers, and electrode geometries, innovative processing, and through the use of tandem architectures. A key issue is to significantly raise the short circuit current density ( $J_{SC}$ ) to above 20 mA/cm<sup>2</sup>. Present values are typically 10-12 mA/cm<sup>2</sup> with champion values approaching 17 mA/cm<sup>2</sup> (C. J. Brabec 2010). Advanced photon management strategies are also being pursued to increase optical absorption. A second challenge is to increase the open-circuit voltage. Key to this is achieving optimal band alignment of the device structure and minimizing the band offset between donor and acceptor molecules while maintaining efficient charge transfer. Third, the fill factors (FF) have to be increased beyond 0.7, which has been achieved in only a

few champion devices. Organic solar cells typically have poor FF relative to conventional *p-n* junctions. This is due to high series resistance and/or carrier recombination, as the carrier mobility in organic thin-films is lower than their inorganic counterparts. Simultaneous achievement of  $J_{SC}=20 \text{ mA/cm}^2$ ,  $V_{OC}=0.8 \text{ V}$ , and  $FF=0.7$ , leading to an efficiency of 11%, has not been achieved yet. Doing this in a single junction device will require simultaneous optimization of all the materials and interfaces. With existing materials and devices, the energy payback time for OPV has been estimated to be between 0.3 and 3 years. This relatively high level of uncertainty reflects the range of assumptions used for this still developing technology. However, an efficiency of closer to 15% may be needed to achieve a true grid-parity leveled cost of electricity of  $\sim \$0.07/\text{kW h}$ . Much work still needs to be done to demonstrate acceptable performance in large area modules.

Another important issue that has to be resolved is the stability of organic solar cells. The chemical, physical, and mechanical degradations that are predominant in OPV materials and devices have been well discussed (M. Jørgensen 2008). The current goal is to increase lifetimes from 3 to 5 years, which is expected to be sufficient for consumer applications. Due to the flexibility of organic synthesis, it can be estimated that there are on the order of  $10^{13}$  different material combinations that could be employed. Whether the right combination of properties (e.g., band gap, charge mobility, exciton diffusion length, etc.) exists and how to identify them remain open questions.

#### **1.1.5. Dye-sensitized solar cells**

Dye-sensitized solar cells are based on the photoelectro-chemical effect discovered by Bequerel in 1839. A relatively new concept, DSSC, was introduced by O'Regan and Gratzel in 1991. (B. O'Regan 1991). They proposed a device based on a hybrid material typically composed of organometallic dye molecules adsorbed on a mesoporous wide band-gap semiconductor and an electrolyte filling the pores. The dye provides high absorption in visible range, thus enabling efficient conversion of sunlight; the working mechanism of DSSC will be discussed in detail in the next chapter. Dye sensitization of oxides was well known at that time, and Gratzel's key innovations were in creating a

nanoparticles film with high surface area to improve light harvesting and in choosing components with appropriate kinetics for fast charge transfer and slow recombination. Gratzel's group rapidly optimized the device to over 10% within a few years of its introduction (M. K. Nazeeruddin 1993). This brought the attention of industry and today a number of small companies are engaged. Most current products are directed at the consumer market, for example, DSSC on flexible substrates that replace rechargeable batteries for portable electronics. A beneficial feature of DSSC is that their performance improves under diffuse and low light conditions (Tulloch 2004), enabling their use indoors and without direct solar exposure. Devices can be fabricated in a number of colors and levels of transparency, which is an attractive feature for architectural and architectural applications. Recent trends evolve to the Building Integrated PhotoVoltaics (BIPV) to replace conventional building materials in parts of the building envelope such as the roof, skylights or facades (F. -T. Kong 2007). According to how and where such systems are built, whether into the facade or in the roof, the BIPV systems are different (Luque A., Handbook of Photovoltaic Science and Engineering 2003). In the case of facade or roof systems the photovoltaic modules are added to the building after it is built. These low powered systems of up to some 10 kW are usually integrated into the south facade. Facade integrated photovoltaic systems could consist of different transparent module types. In such case a part of natural light is transferred into the building through the modules. Solar cells are available in different colours; therefore, there is no limitation for imagination of the architect or the designer. Such constructed buildings give the term architecture a completely new meaning.

Roof-integrated photovoltaic systems are integrated into the roof, that is covered with photovoltaic modules. It is possible to use tiles that integrate solar cells. Photovoltaic systems could be used for shadowing, where photovoltaic modules serve as venetian blinders. In some of such cases photovoltaic modules tilt angle could be adjusted manually or automatically allowing for shadowing the building and/or photovoltaic module efficiency optimization. Such systems are also known as "Shadow-Voltaic" systems. Even if the area-related investment costs of a PV building element is higher than the cost of

conventional high-end elements, the electricity generated and the benefit of architectural double uses may compensate for this difference within a reasonable time (Tulloch 2004). Manufacturing can also be done at low temperature using flexible substrates.

Unfortunately, the champion cell efficiency has been stagnant at ~11% for the past 15 years (Fig. 1.9). Higher efficiency values have been reported for small-area cells. In 2006, Chiba et al. achieved an AIST-validated efficiency of 11.1% using the so-called black dye, a ruthenium terpyridyl complex (coadsorbed with deoxycholic acid) and a masked area of 0.219 cm<sup>2</sup>. More recently, slightly higher efficiencies (up to 12.1%) have been reported for small-area (0.28 cm<sup>2</sup>) DSSC utilizing hexyl(thiophene)-conjugated bipyridine ligands.

With respect to manufacturing numerous module fabrication strategies are being pursued, which, in general, can be divided into monolithic or sandwich constructions. The former offers advantages with respect to material cost, while the latter may be more amenable to roll-to-roll processing. Substrates include glass, metal, and polymer foils, with best performance being obtained on glass. Critical issues include stability and the production of large area modules. At present minimodules with areas <100 cm<sup>2</sup> are used, with resistance losses being one of the major problems. The stability of a DSSC module is strongly related to the device encapsulation. Standard practices for lifetime and stability testing do not exist for DSSC. However, long-term light soaking at 55-60 °C under resistive load has shown that efficiencies remain above 80% of their initial value for over 25 000 h (Desilvestro 2011 ). These Dyesol data on ~ 1 cm<sup>2</sup> cell indicate that carefully encapsulated glass-based DSSC can last for over 20 years in a typical Middle European climate. The longest outdoor test of DSSC modules (110 cm<sup>2</sup>) by Toyota and Asin was 2.5 years, showing efficiency losses of 6% (relative) per year (N. Kato 2011). Faster degradation could be attributed to differences related to sealing methods, cell/module area, or environment. Hermetically sealing flexible DSSC is more challenging, and current products using DSSC on plastic substrates have lifetimes of only a few years. For outdoor applications, the sealing material must, for example, be mechanically and thermally stable, stable under UV exposure, and chemically inert to the electrolyte. Moreover, it should prevent mass transport between adjacent cells. The issue is so important that Hagfeldt *et al.* (A. Hagfeldt 2010) suggested

that the leading manufacturing approach for DSSC may be the one that provides the most functional encapsulation method. Replacing the liquid electrolyte with a gel or solid would greatly reduce encapsulation requirements, but these changes have resulted in decreased efficiency. Elimination of glass, implementation of roll-to-roll manufacturing methods, and increased lifetimes will be critical to economics particularly if device efficiency remains below 12%.

It is interesting to compare these “champion” efficiencies with those of competing thin-film technologies. All of these values are for cells that are 1 cm<sup>2</sup> in area. The most remarkable of these values is the 8.3% for organic cells, which are threatening to catch-up with DSSC. Clearly, competition is strong, and if the DSSC technology is to evolve into a mature and successful commercial one, the current efficiency bottleneck needs to be addressed.

The three main components in a DSSC, the Ru-based dye, the photoanode, and the iodine-based redox couple, have remained largely unchanged. Further optimization of any one of these components individually is not likely to yield significant improvements in efficiency. The recent review by Hamann *et al.* (T. W. Hamann 2008) provides an excellent overview of the complexity of the issues involved. First, the leading dye does not capture much light past 750 nm, and harvesting the red and near-infrared portions of the spectrum is needed to increase current densities. In addition, replacing Ru is an important long-term concern with respect to material availability. Second, the I<sub>3</sub><sup>-</sup>/I<sup>-</sup> redox couple is positioned with a 550 mV overpotential relative to dye regeneration. An alternative redox couple could potentially allow the  $V_{oc}$  to be improved by up to 300 mV, but recombination rates are typically much faster with non-iodine redox couples. A combination of these two changes could elevate device performance to >16%. However, as cautioned by Hamann *et al.* (T. W. Hamann 2008), this will most likely require simultaneous optimization of both dye and electrolyte and perhaps the development of new photoanodes with faster charge transport as well. Photoanode designs based on wide band gap semiconductor nanowires have been applied

to improve efficiency, but six years after their first introduction, their performance remains low.

## 1.5.MATERIAL AVAILABILITY AT TW/YR MANUFACTURING

Manufacturing solar cells at a rate of 1 TW/yr will be a colossal undertaking, and will be strongly conditioned by the availability of material resources. The two elements of concern most often discussed are tellurium and indium (Andersson 2000) (Green 2009). The former is a by-product of copper mining, while indium is a by-product of zinc extraction. Tellurium is one of the least abundant elements in the earth's crust, comparable to the platinum group metals. However, there is great debate and uncertainty in the assessments of Te resources, with the level of concern ranging from critical to manageable to nonexistent. Indium is also scarce, and there are concerns about its price and preferred use in higher value products such as flat panel displays. One concern is that rising demand will increase prices of indium and tellurium by several factors so that the absorber material will become more expensive and larger fraction of the material cost. Such a rise can quickly erode the cost advantages of CdTe and CIGS thin-film technologies.

## 1.6.FUTURE OUTLOOK

### *Redefining the boundaries of PV technologies*

Photovoltaic technologies are often classified as being either first generation (c-Si), second generation (thin film), or third generation concepts that have the potential to overcome the SQ limit such as devices that employ multijunctions, extract hot carriers, or involve multiple electron/exciton generation (Green 2001). In 2001, Green formally classified the potential of first, second, and third generation technologies with respect to both power conversion efficiency and manufacturing costs, and his diagram is reproduced in Fig. 1.10. The quotient of these two variables is proportional to the  $\text{cost}/W_p$ , which is reflected by the dashed lines in Fig. 1.10. The shaded ovals represent the original assessment of the three

generations provided by Green. Advocates of DSSC and OPV often describe these platforms as third generation concepts. However, it should be noted that Green did not make this distinction, limiting his definition to those concepts that can exceed the SQ limit. In practical terms DSSC and OPV should be considered thin-film technologies, ideally competing for the low-cost region of oval II in Fig. 1.10.

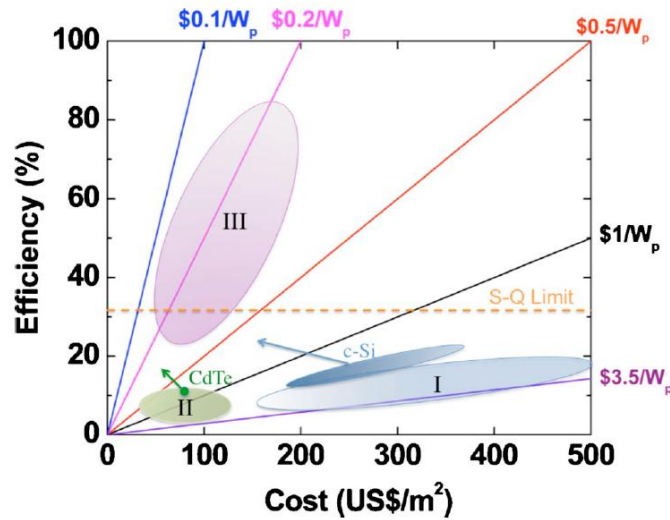


Fig. 1.10. Green's 2001 classification of PV technologies superimposed with the current status (solid and projected evolution) (Wolden 2011).

One of the key points that came out of the workshop discussions was the idea that these accepted boundaries have become outdated. It has become clear that CdTe and c-Si are not bound by the limits imposed by Green's original figure. The current status and projected future of these two technologies have been added to Fig. 1.10. The point for CdTe reflects the present status of First Solar's technology, which is based on 11.2% modules and self-reported production costs of  $\$0.77/W_p$ , putting it on the fringe of the second generation domain. The arrow indicates the expected potential of this technology based on the discussions above. Through improvements in efficiency and further integration of manufacturing it is not unreasonable to expect CdTe manufacturing costs to drop below  $\$0.5/W_p$  within the next decade.



The diversity of products makes the situation for c-Si more complex to analyze, but the revised oval for c-Si also sits on the edge of the initial bounds proposed by Green. Module efficiencies range from 15% to 22%, with leading production costs as low as \$1.10/W<sub>p</sub> reported by Trina Solar in the second quarter of 2010. Again, the arrow leaving the oval represents the future potential of this technology as discussed above. Here, the largest gains are related to further reduction in the production costs through reduction in Si requirements, as well as boosting module efficiency closer to 25%. This combination provides a pathway that approaches \$0.5/W<sub>p</sub>. Some may find this projection overly optimistic. However, one of the enlightening consequences of First Solar's emergence has been the ability of the c-Si industry to rapidly respond and reduce its costs. It is also important to note that silicon does not have to move as far as CdTe. As module costs drop below \$1/W<sub>p</sub> they become increasingly less important as balance of system issues including inverters, racks, installation, and space become important cost drivers. These costs drop with module efficiency, and thus silicon can afford to remain competitive despite higher manufacturing costs than CdTe. It is too early to project what may happen to CIGS, though it is plausible to expect that it might end up in a similar region, most likely somewhere between CdTe and c-Si.

## Chapter 2. Dye sensitized solar cells

*This chapter introduces dye-sensitized solar cell technology: from the working principle to the materials in use. Advantages and drawbacks related to this class of device are put in evidence to introduce the results presented in the following chapters.*

### 2.1 STRUCTURE AND WORKING PRINCIPLE

A dye-sensitized solar cell can be considered as a hybrid of photogalvanic cells and solar cells based on semiconductor electrodes (K. Kalyanasundaram 1998). It consists of a dye-coated semiconductor electrode and a counter electrode arranged in a sandwich configuration, the inter-electrode space being filled with an electrolyte containing a redox mediator (Fig. 2.1).

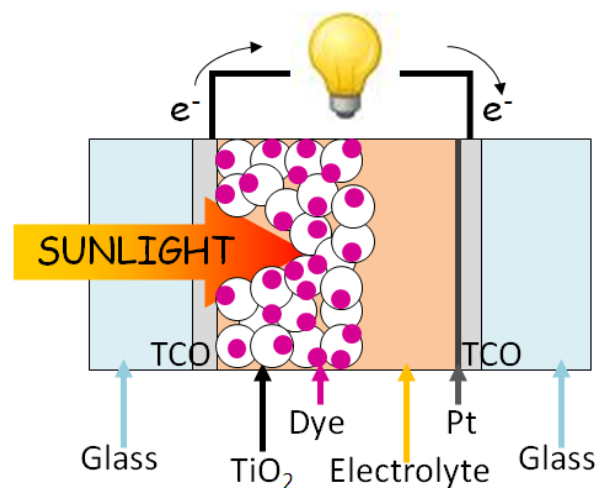


Fig. 2.1: Schematic structure of a DSSC.

Under light irradiation, the dye molecule are photo-excited, and in time of the order of femtoseconds injects an electron into the conduction band of the semiconductor electrode; the original state of the dye is subsequently restored by electron donation from the electrolyte, usually an organic or ionic liquid solvent containing the  $I_3^-/I^-$  redox system (F. - T. Kong 2007), (A. Luque 2003). The iodide is regenerated, in turn, by reduction of triiodide at the counter electrode, the circuit being completed through the external load. The voltage generated under illumination corresponds to the difference between the Fermi level of the electron in the semiconductor electrode and the redox potential of the electrolyte. Overall, electric power is generated without permanent chemical transformation. These primary processes can be schematically summarized (see Fig. 2.2) by the following reactions (A. Luque 2003) (J. Halme 2010).

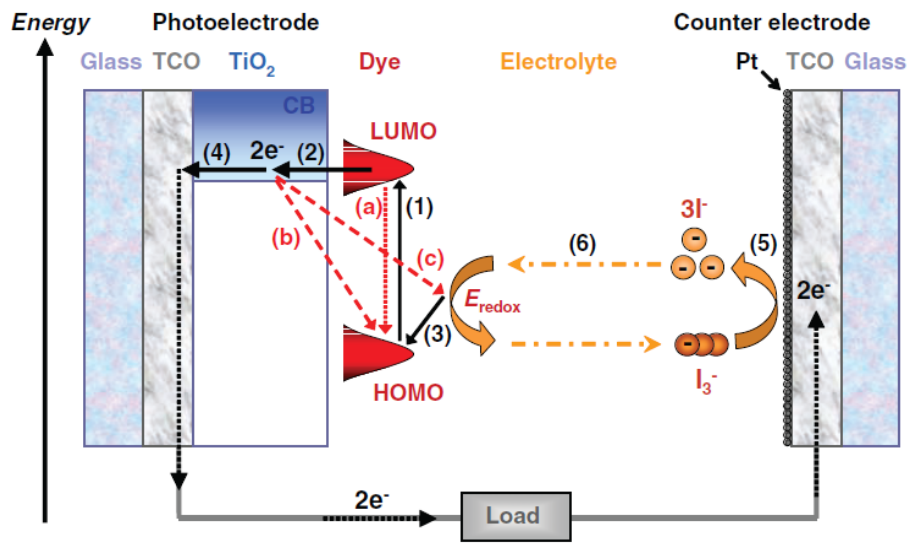


Fig. 2.2: Operating principle of a DSSC (J. Halme 2010). The black and red arrows show the forward and back reactions, respectively.

At the photoanode (PA):

1) The photosensitizers (typically Ru complex) adsorbed on the porous semiconductor material surface (TiO<sub>2</sub>) absorb incident photon flux. The photosensitizer is excited from the ground state S to the excited state S\* due to the metal-ligand charge transfer transition.

$S + h\nu \rightarrow S^*$  - light absorption by the dye -

2) The excited electrons are injected into the conduction band of the TiO<sub>2</sub> electrode, resulting in the oxidation of the photosensitizer.

$S^* \rightarrow S^+ + e^-(TiO_2)$  - electron injection-

3) The oxidized photosensitizer S<sup>+</sup> accepts one electron from the I<sup>-</sup> ion redox mediator, regenerating the ground state S, while I<sup>-</sup> is oxidized to I<sub>3</sub><sup>-</sup>.

$2S^+ + 3I^-(PA) \rightarrow 2S + I_3^-(PA)$  -dye regeneration-

4) Injected electrons in the conduction band of TiO<sub>2</sub> are transported in TiO<sub>2</sub> toward the front contact (TCO) and consequently reach the counter electrode through the external load and wiring.

$e^-(TiO_2) \rightarrow e^-(PA)$  -electron transport

At the counter electrode (CE):

5) The oxidized redox mediator I<sub>3</sub><sup>-</sup> diffuses toward the counter electrode and is again reduced to I<sup>-</sup> ion (the electrons are returned to the cell)

$I_3^-(CE) + 2e^-(CE) \rightarrow 3I^-(CE)$  -overall charge transfer reaction-

At the electrolyte:

6) The electrical circuit of the cell is completed by ionic transport of the redox pair in the electrolyte,

$3I^-(CE) \rightarrow 3I^-(PA)$  -iodide diffusion-

$I_3^-(PA) \rightarrow I_3^-(CE)$  -tri-iodide diffusion-

The total reaction is given by:

$3I^-(PA) + 2h\nu \rightarrow I_3^-(PA) + 2e^-(TiO_2)$  -photoanode

$e^-(CE) + h\nu \rightarrow e^-(PA)$  -cell-

The back reactions limiting the photocurrent (fig. 2.2) are:

a) the non radiative relaxation of the excited state of the dye

b) the recombination of the electrons with the oxidized dye

c) the recombination of the electrons with the tri-iodide in the electrolyte.

The performance of a DSSC is predominantly based on four energy levels of the components (A. Luque 2003): the excited state (approximately LUMO-Lowest Unoccupied Molecular Orbital) and the ground state (HOMO-Highest Occupied Molecular Orbital) of the photosensitizer, the Fermi level of the  $\text{TiO}_2$  electrode, which is located near the conduction-band level, and the redox potential of the mediator ( $\text{I}^-/\text{I}_3^-$ ) in the electrolyte (Fig.2.3).

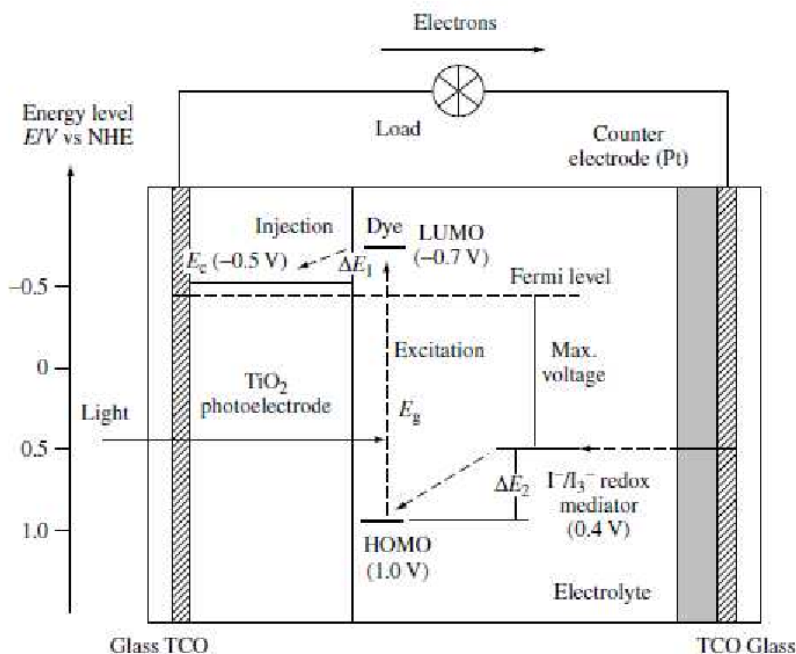


Fig. 2.3: Schematic energy diagram of a DSSC (A. Luque 2003).

The photocurrent obtained from a DSSC is largely determined by the energy difference between the HOMO and the LUMO of the photosensitizer, analogously to the band gap,  $E_g$ , for inorganic semiconductor materials. The smaller the HOMO-LUMO energy gap, the larger the photocurrent will be because of the utilization of the long-wavelength region in

the solar spectrum. The energy gap between the LUMO level and the conduction-band level of  $\text{TiO}_2$ ,  $\Delta E_1$ , is important, and the energy level of the LUMO must be sufficiently negative with respect to the conduction band of  $\text{TiO}_2$  to inject electrons effectively. In addition, substantial electronic coupling between the LUMO and the conduction band of  $\text{TiO}_2$  also leads to effective electron injection. The HOMO level of the complex must be sufficiently more positive than the redox potential of the  $\text{I}^-/\text{I}_3^-$  redox mediator to accept electrons effectively ( $\Delta E_2$ ). The energy gaps,  $\Delta E_1$  and  $\Delta E_2$ , must be larger than approximately 200 mV as driving force for each of the electron-transfer reactions to take place with optimal efficiency.

The voltage in the DSSC is developed by the energy gap between the Fermi level of a  $\text{TiO}_2$  electrode and the redox potential of the  $\text{I}^-/\text{I}_3^-$  in the electrolyte. The conduction-band level of the  $\text{TiO}_2$  electrode and the redox potential of  $\text{I}^-/\text{I}_3^-$  were estimated to be respectively -0.5 V and 0.4 V versus normal hydrogen electrode (NHE). Thus the maximum voltage is expected to be approximately 0.9 V, because the Fermi level of the  $\text{TiO}_2$  electrode depends on the electrolyte components and their concentrations.

In contrast to a conventional p-n type solar cell, the mechanism of a DSSC does not involve a charge-recombination process between electrons and holes, because electrons are only injected from the photosensitizer into the semiconductor and a hole is not formed in the valence band of the semiconductor. In addition, charge transport takes place in the  $\text{TiO}_2$  film, that is separated from the photon absorption site (i.e. the photosensitizer); thus, effective charge separation is expected. The photon-to-current conversion mechanism in a DSSC is similar to the mechanism for photosynthesis in nature, in which chlorophyll functions as the photosensitizer and charge transport occurs in the membrane.

In conventional p-n type solar cells and classical solar cells using polycrystalline or single crystal photoelectrodes, the establishment of equilibrium between the Fermi level of the materials from the photovoltaic junction leads to space charge formation. Photogenerated charges are separated by the electric field in the space charge layer. In DSSC, however, the individual particle size is too small to form a space charge layer. Charge separation in DSSC has been discussed relative to an electrical field at the electrolyte/semiconductor

interface (A. Zaban 1998). Small cations, such as  $\text{Li}^+$ , in the electrolyte and  $\text{H}^+$  released from the dyes upon binding, can adsorb (or intercalate) on the semiconductor surface (A. Luque, Handbook of Photovoltaic Science and Engineering 2003). A dipole is formed across the Helmholtz layer between these cations and negatively charged species (iodide ions and the dye). The electrical potential drop across the Helmholtz layer can help to separate the charges and reduce recombination with the dye cations or the redox mediator. Under illumination, this potential will decrease, as the electrons injected in the semiconductor will neutralize some of the positive charge at the surface.

## 2.1. DSSC MATERIALS

The basic structure of a DSSC presented above is based upon some important materials: the TCO (Transparent Conductive Oxide)-glass substrate, the  $\text{TiO}_2$ , the dye sensitizer, the electrolyte and the counter electrode.

### 2.1.1. TCO-conductive glass substrate

The TCO-coated glass is used as the substrate for the electrodes (A. Luque, Handbook of Photovoltaic Science and Engineering 2003). For high solar cell performance, the substrate must have low sheet resistance and high transparency. In addition, the material should be heat resistant up to  $500\text{ }^\circ\text{C}$  because this temperature is reached during the standard cell fabrication process.

Indium–Tin oxide (ITO) is one of the most famous TCO materials. In spite of having low resistance at room temperature, ITO resistance increases significantly after high temperature treatment in air. Therefore, the more stable fluorine-doped  $\text{SnO}_2$  (FTO) is used as the TCO substrate for DSSCs.

### **2.1.2. TiO<sub>2</sub> semiconductor electrode**

Photoelectrodes made of common semiconductors as Si, GaAs, InP, and CdS decompose under irradiation in solution owing to photocorrosion. In contrast, oxide semiconductor materials have good chemical stability under visible irradiation in solution. Semiconductor oxides used in dye-sensitized solar cell include TiO<sub>2</sub>, ZnO, SnO<sub>2</sub>, Nb<sub>2</sub>O<sub>5</sub>, and so forth, which serve as the carrier for the monolayers of the sensitizer using their huge surface and the medium of electron transfer to the conducting substrate (F. -T. Kong 2007) . So far, TiO<sub>2</sub> is the best choice in semiconductor due to low price, abundance in the market, nontoxicity, and biocompatibility, (it is also used widely in health care products as well as in paints). DSSC photoanodes will be extensively discussed in chapter 5.

### **2.1.3. Dye photo-sensitizer**

Dye sensitizers serve as solar energy absorber in DSSC, whose properties have much effect on the light harvesting efficiency and the overall photoelectric conversion efficiency (F. -T. Kong 2007). The ideal sensitizer for dye-sensitized solar cells should absorb all light below a threshold wavelength of about 920 nm. In addition, it should be firmly grafted to the semiconductor oxide surface and inject electrons to the conduction band with a quantum yield of unity. Its redox potential should be sufficiently high that it can be regenerated rapidly via electron donation from the electrolyte or a hole conductor. Finally, it should be stable enough to sustain at least 10<sup>8</sup> redox turnovers under illumination, corresponding to about 20 years of exposure to natural light. The best photovoltaic performance in terms of both conversion yield and long-term stability has been so far achieved with polypyridyl complexes of ruthenium and osmium. The sensitizers used in DSSC are divided into two types: organic dyes and inorganic dyes, according to their structure. Inorganic dyes include metal complexes, such as polypyridyl complexes of ruthenium and osmium, metal porphyrin, phthalocyanine and inorganic quantum dots, while organic dyes include natural organic dyes and synthetic organic dyes. Compared with organic dyes, inorganic complexes dyes have higher thermal stability and chemical stability.



Among these complexes, polypyridyl ruthenium sensitizers were widely used and investigated for their high stability and outstanding redox properties and good response to natural visible sunlight. The sensitizers are anchored on the surface of the semiconductor electrode with carboxylate groups or phosphonate groups, that enable the electron injection into the conduction band of the semiconductor. Polypyridyl ruthenium dyes may be divided into carboxylate polypyridyl ruthenium dyes, phosphonate ruthenium dyes, and polynuclear bipyridyl ruthenium dyes. The difference between the first two types of sensitizers lies in the adsorption group. The first two types of sensitizers differ from the last type of sensitizer in the number of metal centres. The carboxylate polypyridyl ruthenium dye is in level structure, which enables the electron injection into the conduction band of the semiconductor quantitatively. Among these sensitizers, N3 and its tetrabutylammonium salt N719, black dye (fig. 2.9, 2.10) showed unmatched performance.

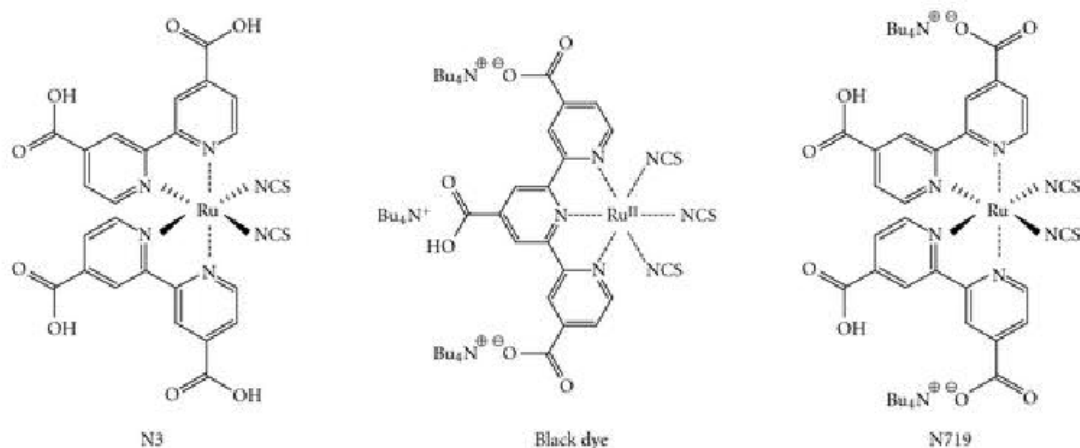


Fig.2.4.Molecular structure of the most used dyes.

Carboxylate polypyridyl ruthenium sensitizers are easily desorbed from the surface in aqueous solution when the pH value is lower than 5, though they have a lot of advantages. The phosphonate polypyridyl ruthenium sensitizers use phosphonate group to be anchored to the surface of the semiconductor, that is hardly desorbed from the semiconductor surface

even at high pH value, however, phosphonate group is not in conjugation with the polypyridyl plane due to their non-plane structures, which is in disadvantage to the injection of electrons. Organic dyes are easy to be designed and vary in style with molar extinction coefficient and low cost. In recent years, the development of DSSC based on organic dye is very rapid and the conversion efficiency of the solar cells that based is comparable to that based on polypyridyl ruthenium dye. Generally, an organic dye has the general structure of “Donor (D)- $\pi$  conjugation bridge-acceptor (A).” With the electron withdrawing and donating effects of acceptor and the donor moieties, the absorption response of the visible light are red-shifted, which improves the light harvesting and short circuit photocurrent of the solar cells. Sensitization with one single dye was restricted for its absorption spectrum hardly matches with the solar emission spectrum. Cosensitization of several dyes with different spectral response instead of one single dye was used for wide-band-gap semiconductor. By cosensitization of squaraine dye and polypyridyl ruthenium dye in a proper ratio, the spectral response scope was widened and the photovoltaic performance of solar cells was improved (W. Zhao 1999).

#### **2.1.4. Electrolyte**

The electrolyte is one of key components for dye-sensitized solar cells and its properties strongly affect the conversion efficiency and stability of the solar cells (F. -T. Kong 2007). The electrolytes used in DSSC are divided into three types: liquid electrolytes, quasi-solid state electrolytes and solid electrolytes.

Liquid electrolytes can be divided into organic solvent electrolytes and ionic liquid electrolytes, according to the solvent used.

Organic solvent electrolytes were widely used and investigated in dye-sensitized solar cells for their low viscosity, fast ion diffusion, high efficiency, easy to be designed, and high pervasion into nanocrystalline film electrode (M. Grätzel 2001). The composition of the electrolytes includes organic solvent, redox couple, and additive (F. -T. Kong 2007). Organic solvents used in organic liquid electrolytes include nitrile such as acetonitrile,

valeronitrile, 3-methoxypropionitrile, and esters such as ethylene carbonate (EC), propylene carbonate (PC),  $\gamma$ -butyrolactone.

The major redox couple is the  $I_3^-/I^-$  couple. Alkyl imidazolium cations and lithium cations are usually used as the counterions of  $I_3^-/I^-$  couple in DSSC. Alkyl imidazolium cations may be adsorbed on the surface of semiconductor film to form the Helmholtz layer, which restricts the contact of triiodide and semiconductor films, for the recombination between triiodide and electron in the conduction band of semiconductor. As a result, the fill factor and conversion efficiency of the solar cells are improved. Furthermore, the high solubility of alkyl imidazolium cations in organic solvent and the high activity of iodide increase the light harvesting efficiency and photocurrent as well as the stability of the sensitizer.

Unfortunately,  $I_3^-/I^-$  is not the most desirable mediator due to the following negative features:

- i.  $I_2$  is corrosive toward most metals;
- ii.  $I_2$  has a substantial vapour pressure, which causes an instability in the conversion efficiency unless the cell can be perfectly sealed;
- iii. the  $I_3^-/I^-$  redox couple can absorb a significant amount of visible light;
- iv. the redox potential of the  $I_3^-/I^-$  redox couple limits further improvements of the maximum open circuit photovoltage.

For these reasons a new colorless redox couple consisting of tetramethylthiourea and its oxidized dimer tetramethylformaminium disulfide dication has been applied to DSSCs (D. Li 2010). This redox couple exhibits some attractive advantages such as low cost, easy handling, non-corrosiveness, and lack of visible-light absorption. An important alternative to the  $I_3^-/I^-$  couple is  $CoII/CoIII$  that, in conjunction with a dye cosensitization (porphyrin and aliphatic chains), permits to have 12.4% on small area DSSC (Grätzel 2011).

The commonly used additive used in the electrolytes for dye-sensitized solar cells contains 4-tert-butylpyridine (TBP) (F. -T. Kong 2007). The addition of these additives could suppress the dark current and improve the photoelectric conversion efficiency. TBP could reduce the recombination of electrons in the conduction band of the semiconductor and the electron acceptor in the electrolyte through the coordination between N atom and the Ti ion

in incomplete coordination state on the surface of  $\text{TiO}_2$  film. Then, the photovoltage fill factor and the conversion efficiency increase dramatically.

The efficiency record of DSSC was obtained on solar cells based on organic solvent electrolyte, especially the highly volatile organic solvent electrolyte, due to the efficient infiltration of organic electrolyte in nanocrystalline films. However, the solar cells based on organic electrolytes have disadvantages such as less long-term stability, difficulty in robust sealing and consequent leakage of electrolyte due to the volatility of organic solvent.

Ionic liquid electrolytes were developed in recent year in view of the disadvantage of organic solvent electrolytes. Compared with normal organic solvent electrolytes, ionic liquids have many advantages, such as good chemical and thermal stability, negligible vapour pressure, non flammability, high ionic conductivity and high solubility for organic or inorganic materials, and a wide electrochemical window, that has been intensively pursued as alternative electrolytes for DSSC and other electrochemical devices. In recent years, ionic liquid electrolytes were developed rapidly. The electrolyte with 1-hexyl-3-methylimidazolium iodide gave the highest photoelectric conversion efficiency. Among these ionic liquids, alkyl imidazolium-based ionic liquids are both iodide sources and solvents of electrolytes in solar cells; they are viscous liquids, whose viscosity is much higher than that of organic-solvent-based liquid electrolytes. Then the transport of  $\text{I}^{3-}$  in the electrolyte is very slow and the mass transfer process occupies the leading position. To improve the mobility of redox couple in the electrolyte and the photovoltaic performance, various ionic liquid with low viscosity were developed.

The evaporation of the liquid electrolyte often causes some practical limitations of sealing and long-term operation. Recently some attempts were made to improve the long term stability by using a p-type semiconductor (G. R. A. Kumara 2002) or hole transporting organic materials (U. Bach 1998) to replace a liquid electrolyte. However, their conversion efficiencies are not comparable with those of the liquid solar cells (F. -T. Kong 2007). Thus, it can be seen that quasi-solid state ionic liquid electrolytes might be a better choice to increase stability. Owing to their unique physicochemical properties such as high

thermal stability, negligible vapour pressure, relatively high ionic conductivity and good stability, ionic liquids were widely used in dye sensitized solar cells. In general, quasi-solid-state ionic liquid electrolyte consists of  $I_3^-/I^-$  couple such as 1-methyl-3-propylimidazolium iodine (MPII) and framework materials. In quasi-solid electrolytes, framework materials (polymers, gelator and silica nanoparticles) play an important role in offering a liquid channel for the  $I_3^-/I^-$  diffusion.

#### **2.1.5 The counter-electrode**

Solar cell studies employ usually a F-doped  $SnO_2$  as the conducting glass electrodes (K. Kalyanasundaram 1998). Such electrodes are known to be poor choice for efficient reduction of triiodide. To reduce the overvoltage losses for reduction of the redox couple, a very fine Pt-layer or islands of Pt are deposited onto the conducting glass electrode ( $5-10 \mu g cm^{-2}$  or approximately 200 nm thickness). This ensures high exchange current densities at the counter electrode and thus the processes at the counter electrode do not become rate limiting in the light energy harvesting process. Hence, the counter electrode serves to transfer electrons arriving from the external circuit back to the redox electrolyte. It also has to carry the photocurrent over the width of each solar cell (A. Kay 1996). DSSC cathodes will be discussed in chapter 4 in detail.

#### **2.1.6. The sealants**

As mentioned above, DSSC generates the power by chemical reaction between dye and electrolyte (K. Kishi 2005). As electrolytes are liquid, in order to use DSSC as a stable power supply, sealing technology is required to prevent electrolyte from leaking. Electrolyte consists of high-polarity organic solvents, iodides, and additives. Organic solvent composition depends on required cell performance, but organic nitrile-based solvents are mainly used. These solvents have a high polarity and dissolve most organic compounds. Unfortunately the high adhesiveness required for the sealants involves a high polarity and hence sealants with good adherence are more prone to be corroded by the

solvent. In other words, relationship between sealing property and electrolyte resistance property is a trade-off. However, reliability of cells strictly depends on the quality of the seal and therefore the highest priority as a performance required for sealing agents for DSSC is to control leakage of electrolyte. To prevent leakage of iodide electrolyte in liquid phase as well as in vapour phase, the chemical structure of the resin must be hard to corrode to polar solvent and iodine.

## 2.2. ADVANTAGES OF THE DSSCS

The fashionable characteristics of the DSSC can be summarized in several points (A. Luque 2003).

- i) High energy conversion efficiency: A DSSC efficiency equal to that of the amorphous-Si solar cell has been obtained during laboratory development and efficiencies greater than 10% may be possible.
- ii) Low-cost fabrication: The DSSC is very simple to construct and is made of low-cost materials. Fabrication costs will therefore be less than that for conventional solar cells. For example, a cost of US\$ 0.60/W that may be competitive for conventional solar cells, has been estimated for a DSSC with 10% efficiency (G. Smestad 1994).
- iii) Abundant supply of component materials: Oxide semiconductors such as  $\text{TiO}_2$ , dye, and iodine are abundantly available. Although metal deposits of Ru are limited, organic dye photosensitizers could be used rather than Ru complexes if resource limitation is a problem.
- iv) Good potential for colourful, adaptable consumer products: multicoloured semi-transparent solar cells can be made using various kinds of dyes, depending on the use of the cell. Transparent solar cells could be used in place of windowpanes. Additionally, the use of a plastic substrate, rather than glass, is possible if low temperature processing of the  $\text{TiO}_2$  film preparation ( $<250^\circ\text{C}$ ) is available and would expand the use of DSSC.

For transparency they should transmit a significant fraction of visible light. This requirement cannot be reconciled with the optical characteristics of conventional p-n junction solar cells. As semi-conductors are threshold absorbers harvesting practically all the photons with energy above their band gap, they are opaque in the visible. By contrast, for the DSSC it is feasible to employ sensitizers absorbing selectively the near IR and UV part of the solar spectrum, while visible light passes through the cell. Dyes such as naphthocyanines fulfil the optical requirement for such applications. In particular, they have a very strong absorption feature in the  $700\pm 920$  nm region, where the solar photon flux is very intense. A device that would capture all the photons in this wavelength interval alone could produce a short circuit current of  $14 \text{ mA/cm}^2$  and the contribution from the absorption of UV light by the  $\text{TiO}_2$  would raise this to  $15 \text{ mA/cm}^2$ . Using the standard iodide-based redox electrolyte, solar conversion efficiencies of  $7\pm 8\%$  appear feasible. This is sufficient to make the system economically attractive as the cell is integrated in the existing glass elements of the building. Conventional PV modules are mounted on a metal support, contributing substantially to the overall price of photovoltaic installations. Integrating the cells into building facades would reduce this cost significantly. Thus, power windows based on the DSSC concept have, in principle, the potential to be realized, opening up an enormous potential for future architectural exploitation of photovoltaic cells.

v) Low potential for environmental pollution: The  $\text{TiO}_2$ , dyes, and iodine used in the DSSC are nontoxic. The only component that could potentially cause harm is the organic solvents used in the electrolyte solution. Future research should be directed toward developing a solid-state electrolyte.

vi) Good recyclability: The organic dye photosensitizers adsorbed on the electrode can be removed by washing the electrode with alkali solutions or combustion, providing recyclability of the DSSC.

## Chapter 3. Practical cell assembly and characterization

*In order to use the novel nanostructured materials developed as DSSC electrodes, it was necessary to assess the procedure to fabricate small lab-scale device. A great effort was therefore devoted to the standardization of the protocols to prepare photoanodes and cathodes, and to assemble the complete device, in order to allow meaningful comparison of performances. This chapter describes the procedures set up for the realization of the electrodes, the assembly of devices and their characterization using current- voltage measurements under illumination.*

### 3.1. DEVICE COMPONENTS

#### 3.1.1. Titania photoanodes

Pilkington TEC8 fluorine doped tin oxide coated glasses were purchased; a SEM picture details of the FTO surface is shown in Fig. 3.1. A glass thickness of 2 mm was chosen in order to have a robust support withstanding the pressure needed for the sealing procedure. The glasses were cut in 2cmX2cm squares. Substrates for the PA were washed in acetone and then in ethanol in ultrasonic bath for 15 minutes before use. The cleaning procedure was concluded by a UV-O<sub>3</sub> cleaning step obtained by placing the FTO for 30 minutes under a UV light producing a small amount of highly oxidizing O<sub>3</sub>. The clean substrates



were immersed for 30' in an aqueous solution 0.4mM of  $\text{TiCl}_4$  at  $70^\circ\text{C}$ , then they were rinsed in water and ethanol and left to dry.

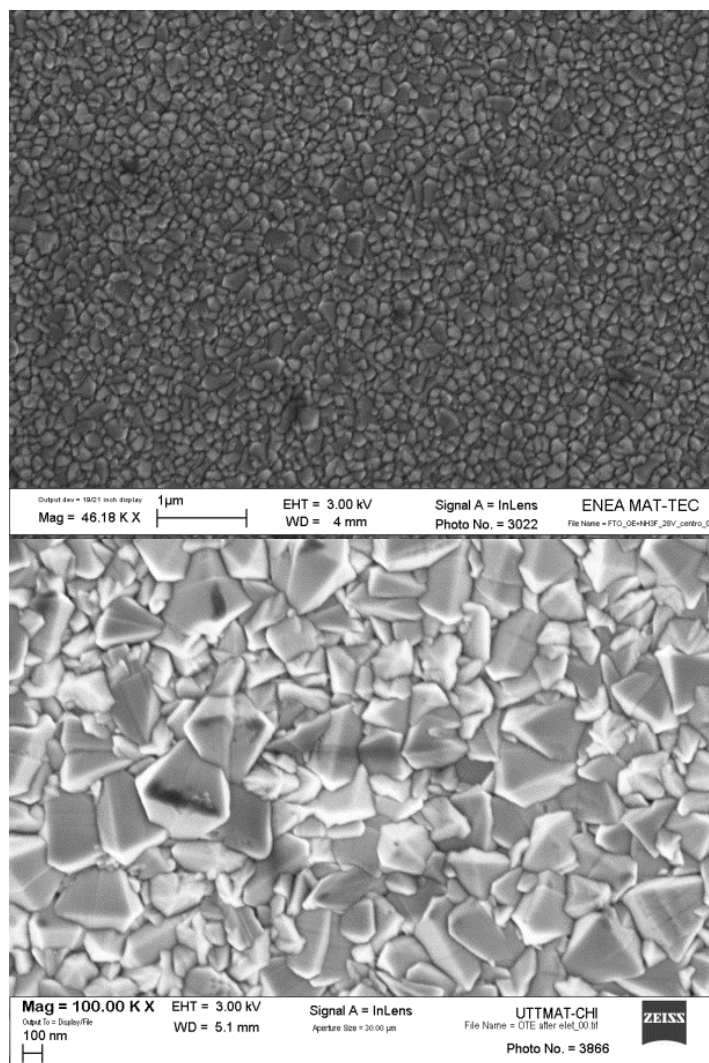


Fig. 3.1. SEM micrograph of a bare FTO substrate.

A commercial titania paste, Solaronix D/SP, was used as starting material for the preparation of the mesoporous titania electrode. The paste contains ~18 % wt. of nanocrystalline anatase titanium dioxide (diameter of 15-20 nm) mixed with optically

dispersing particles (diameter > 100 nm). The paste also contains terpineol and organic binders (<http://www.solaronix.com/products/screenprintingtitania/tinanoxidedsp/> s.d.).

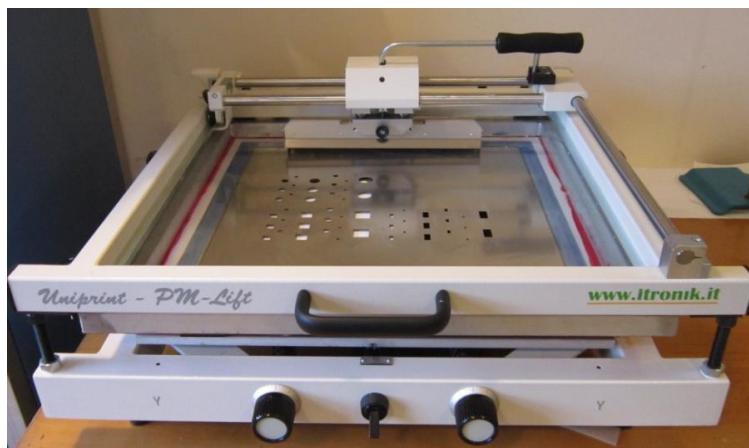


Fig. 3.2. Picture of the screen printer used for the preparation of DSSC electrodes.

The deposition of the titania layer was done by screen printing, a method that ensures a good reproducibility of the layer thickness. The screen printer apparatus, shown in Fig. 3.3 was purchased from Itronik, and it is equipped with a 100 micron thick, stainless steel mask with 0.5cmx0.5cm square windows. The paste was spread on the substrates using a Teflon blade; after this operation the electrodes were heated in air in order to obtain the evaporation of the solvents, the sintering of the particles and the total combustion of the organic binders. An oven with a programmable controller was used to this aim; several attempts were carried on in order to optimize the heating ramp up to 500°C. Several isothermal periods are necessary to leave the decompositions of the different components that induces mechanic tension in the film with the formation of cracks and even delamination. It was observed that even the cooling rate of the sintered electrodes needs to be very slow in order to minimize the mechanical stress at the interface FTO/TiO<sub>2</sub>. A careful control of the real temperature in the oven was obtained by using a thermocouple fixed just near the pyrex sample holder, instead of the one originally installed in the oven.

Temperature overshooting phenomena were damped by fine tuning of the parameters of the programmable oven controller. The optimized temperature profile of the thermal treatment of the titania electrodes is shown in Fig. 3.3.

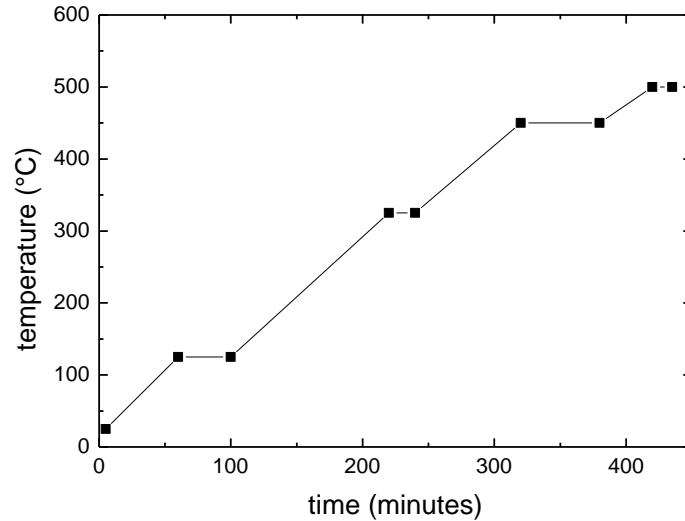


Fig. 3.3. Temperature program for sintering of screen-printed titania films.

The thickness of the titania layers, measured with a mechanical profilometer (Tencor Alphastep), was 6.5  $\mu\text{m}$ , with a standard deviation of less than 0.5 micron, for electrodes prepared in different batches. Moreover the absence of microscopic cracks and peeling off was verified by inspection at the optical microscope, confirming the suitability of the screen printing method for reproducible preparation of good-quality electrodes.

The typical morphology of a titania electrode, at different magnifications, is shown in Fig.3.4.

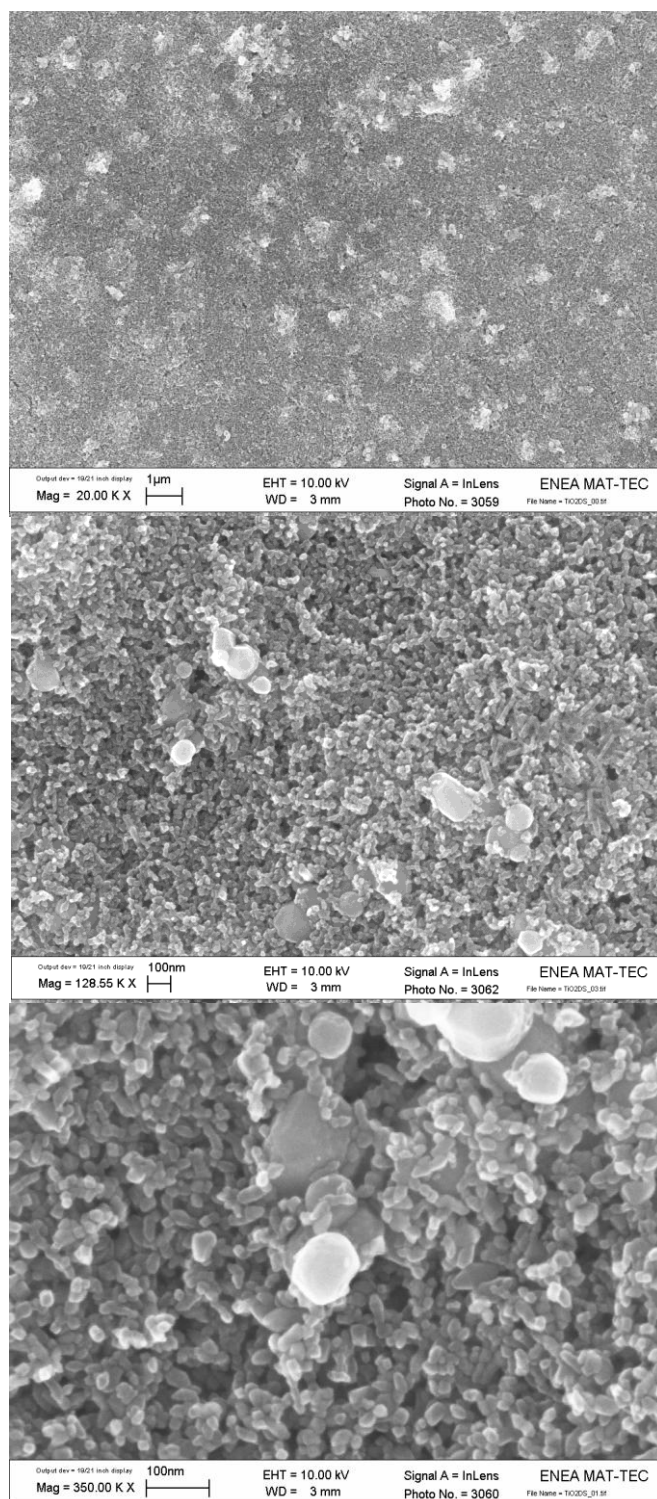


Fig. 3.4. SEM images of a sintered titania electrode.

After the sintering process the electrodes were immersed in aqueous  $\text{TiCl}_4$  solution (0.4 mM) at  $70^\circ\text{C}$  for 30 minutes, then rinsed in water and ethanol and left to dry before heating up to  $500^\circ\text{C}$  in air with a linear temperature ramp of 6 hours. They finally were left to slowly cool till  $70^\circ\text{C}$  and then were immersed and left overnight in the dye solution at room temperature in a sealed glass can. The dye used in this work is *cis*-diisothiocyanato-bis(2,2'-bipyridyl-4,4'-dicarboxylato) ruthenium(II) bis(tetrabutylammonium), known as N719, purchased from Solaronix. The 0.5 mM dipping solution was prepared in absolute ethanol; all reagents were used as received. Before use, the solution was sonicated for 3 minutes to favour elimination of dye aggregates, which could be absorbed on the electrode with consequent degradation of device performance. After the dye soaking, the electrodes were thoroughly rinsed in absolute ethanol to remove excess dye molecules not properly adsorbed to titania nanoparticles, then the device was assembled and sealed to avoid the exposure of the dye to air and moisture. In Fig. 3.5 a titania electrode is shown, before and after sensitization.

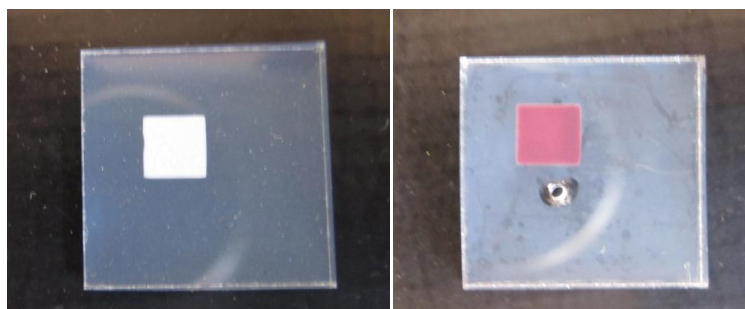


Fig. 3.5. Picture of a titania electrode before and after dye-sensitization.

### 3.1.2. Catalyzed cathodes

TCO-coated glasses (Pilkinton TEC8) 2mm thick cut in 2cmx2cm squares were used as standard cathode support. In order to fill the cell with the liquid electrolyte it is necessary to make at least one hole in the substrate. A single hole (diameter 1mm) was drilled in the

glass immersed in water by a diamond tip. After the hole was drilled the back side of the coated glass was sanded to make the surface rough and favour the adhesion of the sealing foil after electrolyte filling. Then the electrode was washed in acetone and ethanol before Pt deposition.

Deposition of catalytic Pt clusters was obtained by thermal decomposition of a screen-printable Pt-containing paste, purchased from Solaronix. The paste was spread by using a 100 micron thick stainless steel mask on a 1.8x1.8cm square. Then the electrodes were put in an oven in the dark (to avoid light-induced Pt catalyst precursor damages), heated to 400°C for 30 minutes, and finally cooled slowly to room temperature. Small clusters of metallic platinum form.

### **3.1.3. Electrolyte**

A well known literature recipe was followed to prepare the electrolyte solution in acetonitrile containing LiI (Sigma Aldrich) 2M, I<sub>2</sub> (Sigma Aldrich) 0.22M, 4-*tert*-butylpyridine (Sigma Aldrich) 0.5M. All the materials were used without further purification.

## **3.2.DEVICE ASSEMBLY AND SEALING**

The electrodes must be sealed slightly displaced to leave sufficient room for the cell contacts. As sealing material, Surlyn<sup>®</sup> hot melt foils from Dupont was employed. Gaskets were punched in 60 micron thick foils and inserted between the facing electrodes; a small patch of Surlyn<sup>®</sup> was also used to seal the hole drilled in the cathode as mentioned above. The sealing process consisted in pressing the electrodes at 120°C. The process ensures the melting of Surlyn<sup>®</sup> that perfectly adheres to the F-doped tin oxide inside the cell and on the sanded external glass. The Surlyn<sup>®</sup> patch was then cut by a lancet and the slot is used to fill the electrolyte in the cell with the vacuum method. A syringe containing small amount of electrolyte was used to evacuate the volume of the cell and then to inject the liquid. A hot

drop of glue (ethylene-vinyl acetate) was then oozed to seal the slot in the Surlyn<sup>®</sup> patch. The electrical contacts of the cell were made by crocodile clips inserting a copper thin foil on the FTO to improve the contact and prevent the oxide surface from scratching. The cell is eventually complete and ready to be characterized.

### 3.3.CELL CHARACTERIZATION

The I-V characteristics of a solar cell are usually measured under standard illumination conditions, that is AM1.5 spectrum with incident power density of  $100\text{mW/cm}^2$ . In our lab the standard illumination conditions were simulated by a Xenon lamp (Oriel) with a AM1.5 optical filter, and verifying that the power density on the device was the required  $100\text{ W/cm}^2$ . Illuminated and dark current-voltage curves were acquired using a PARSTAT 2273 galvanostat/potentiostat applying a bias potential ranging from -0.2 up to 0.8 V.

A commercial cell purchased from Solaronix, with photovoltaic performance certified from the vendor, was tested both with our equipment and with a ClassA solar simulator. The J-V characteristics are shown in Fig. 3.4.and the photovoltaic parameters reported in Tab. 3-1; the small discrepancies between the parameters derived from the characteristic certified by Solaronix and that obtained using a solar simulator are of the same entity of the ones obtained comparing characteristic measured in our laboratory by using a “low cost” solar simulator. So that our equipment can be considered affordable to characterize our cells, especially considering that our devices are not optimized and the photovoltaic characteristic is just a way to validate the functional properties of our novel materials or to assess the validity of optical model developed in this work.

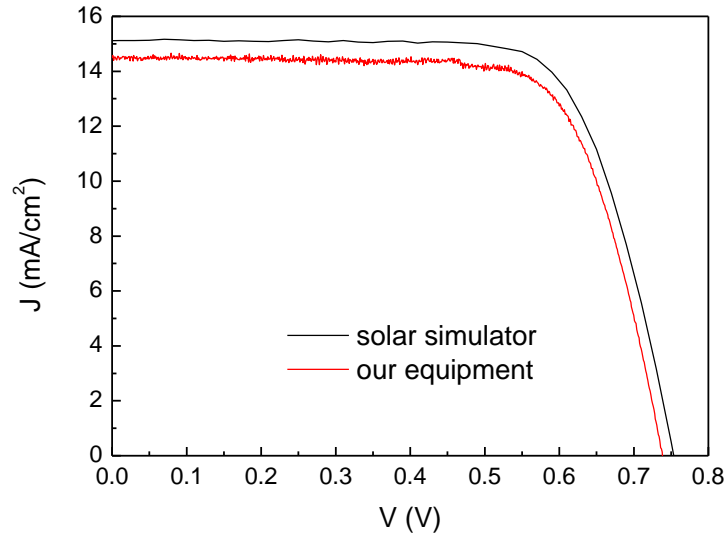


Fig. 3.4. Current density to voltage characteristic of a commercial DSSC measured under different illumination conditions.

	$V_{oc}$ (V)	$J_{sc}$ (mA/cm <sup>2</sup> )	$p_{MAX}$ (mW/cm <sup>2</sup> )	FF	$\eta$ (%)
<b>Our equipment</b>	0.74	14.5	7.8	0.72	7.8
<b>Solar simulator</b>	0.75	15.1	8.2	0.73	8.2
<b>Solaronix</b>	0.70	15.1	7.5	0.70	7.5

Tab. 3-1. PV parameters obtained by characterizing the same commercial DSSC under different illumination conditions, parameters declared by the vendor (Solaronix) are also reported.

	$V_{oc}$ (V)	$J_{sc}$ (mA/cm <sup>2</sup> )	$p_{MAX}$ (mW/cm <sup>2</sup> )	FF	$\eta$ (%)
<b>Pioneer cell</b>	0.56	10.8	2.96	0.49	3.0
<b>Recent cell</b>	0.60	12.4	4.06	0.54	4.1

Tab. 3-2. PV parameters of one of the first DSSC assembled during this thesis and one of the best recent device.



As previously reported, a great care was devoted to the standardization and optimization of preparation and characterization of devices, that enabled to obtain meaningful data to be used as a feedback for the synthesis of novel electrodes, supported by the development of models. The photovoltaic parameters of a standard cell prepared at the very beginning of this work and one of the last devices assembled as described in this chapter are reported in Tab. 3-2 for comparison. It is clearly evident that, even if the optimization of device in terms of components choice and assembly is beyond the aim of this work, sizeable improvements were obtained, so that the more recently assembled devices are less affected by trivial defects that, causing high losses in efficiency can mask the phenomena due to functional properties of the materials under investigations.

## Chapter 4. Carbon nanostructures as cathode materials

*The electrocatalysis process at cathode in DSSC is provided by Pt films or nanoparticles. One of the key steps in order to diffuse DSSC into the market is the replacement of Pt, since it is a rare and expensive material. Carbon is the ideal candidate to this aim, and a lot of efforts are devoted to the preparation and characterization of carbon based nanomaterials for application in DSSC cathodes. In this framework, depicted in the first paragraph with a review of the state of the art, graphitic nanostructures, carbon nanowalls can be interesting as cathode material. In this chapter synthesis and characterization of several samples is described and results obtained in application in complete devices are presented, with a discussion of the results and a sketch on the possible future work.*

### 4.1. STATE OF THE ART

Carbon is one of the most abundant elements in the earth's crust and is found in many allotropes. The different combinations in which carbon atoms can be arranged produce a wide variety of compounds that have unique and interesting physical, chemical, and electronic properties (M. P. Ramuz, 2012) (Hirsch, 2001) (T. Dinadayalane, 2010). Carbon allotropes include fullerenes, carbon nanotubes (CNT), and graphene. Depending on the chemical nature, some have been shown to be conducting, while others are semiconducting. Therefore, it is potentially possible to use these materials in combination

to fabricate devices composed completely of carbon-based components. Indeed, carbon-based devices offer several attractive features for use in next-generation electronics. First, due to the abundance of carbon, carbon-based devices can be potentially made cheaply and in large quantities. The production of carbon nanotubes, graphene, and fullerenes has increased exponentially over the past several years, and new methods and processes are continuously being developed to improve upon the scalability and cost (R.V.Noorden, 2011) (H. Murayama, 2005). Second, these materials can be dispersed and deposited using solution processes, and they are integrable into tools and processes already developed for established materials, such as roll to roll manufacturing. Third, due to the highly tunable electrical and optical properties that can be obtained from these materials, they can be used in many different types of devices such as transistors, solar cells, displays, and supercapacitors (R. H. Baughman, 2002). Finally, they have long-term chemical and temperature stability potentially unmatched by any other materials. In fact, researchers have already demonstrated all carbon-based devices, in which both the electrodes and the active components are all made with carbon materials (H.J. Jeong, 2011). The advantages of using a carbon-based device can be demonstrated by its high flexibility and environmental stability when compared to devices composed of other materials. All-carbon transistors composed of semiconducting single-walled carbon nanotubes (SWNT) or graphene nanoribbons with graphene or CNT electrodes and all-carbon supercapacitors have also been demonstrated. More recently, the use of carbon allotropes in photovoltaics has been demonstrated. Fullerenes have been incorporated in organic photovoltaics (OPV) since 1995. Fullerene derivatives, in particular [6,6]-phenyl-C61-butyric acid methyl ester (PC60BM), are the most commonly used acceptor material in OPVs due to their high electron affinity, although there has been a demonstration of using C60 as the primary active element in an OPV (N. S. Sariciftci, 1993) (L. J.Chen, 2011). Graphene and graphene oxide (GO) have predominately been used in PV as electrodes and hole transport layers, respectively. The thin 2D structure of graphene in addition to its high transparency and conductivity has made it an ideal candidate for electrode material for OPV. Similarly, CNT have primarily been used only as electrodes in PV and then incorporated in the active

layer of solar cells in hybrid structures as an additive to improve charge transport, such as in organic, silicon, and other inorganic PV structures. Recently, Arnold et al. (M. S. Arnold, 2009) reported a solar cell device consisting of an all-carbon active layer with semiconducting nanotubes as both the light-absorbing and donor material with C60 as the acceptor. Tung et al. (V. C. Tung, 2012) fabricated solar cells with active layers composed of a mixture of solution-processed C60, SWCNT, and reduced graphene oxide. Graphene oxide was used as a surfactant to aid with the dispersion. The maximum IPCE of these devices was 0.21% under AM1.5 80mW/cm<sup>2</sup> illumination.

In the particular case of DSSC, the cathode serves to transfer electrons arriving from the external circuit back to the redox electrolyte and to catalyze the reduction of iodine, so, the ideal material should possess low sheet resistance, high catalytic activity, as well as good chemical stability and low production cost. Because of its excellent electrocatalytic activity for iodine reduction, high electric conductivity and good chemical stability, platinum is widely used. However, the high cost of Pt and its limited reserves in nature are driving the research efforts in the direction of its replacement. Ever since 1996, Kay and Graetzel (A.Kay, 1996) proposed the use of carbon at the cathode in DSSC, because it combines sufficient conductivity and electrocatalytic activity as well as corrosion resistance. With respect to a platinum cathode the conductive glasses covered with carbon presented higher ohmic resistance that reduced the fill factor, but the overall conversion efficiency was demonstrated to be encouraging, as shown in Fig. 4.1. Afterwards, carbon nanoparticles and carbon nanotubes were extensively studied (T. N. Murakami, 2006) (S. Gagliardi, 2009 ) as well as graphene-based and doped graphene-based materials (Y. Xue, 2012) (L. Giorgi, 2007) (E. Ramasamy, 2007).

Kay and Graetzel proposed to fabricate a porous carbon based cathode starting from graphite powder, made of of platelike crystals that, on deposition from liquid suspension and drying, preferentially align in the plane resulting highly conductive. The catalytic activity was considerably enhanced by adding 20% of carbon black. For good adhesion between the graphite particles and carbon black as well as the adhesion to the substrate, a binder to be fired at 450°C in air was necessary. Successively, several authors proposed

carbon based inks to be used without any firing (S. Gagliardi, 2009 ) or after firing at low temperatures (T. N. Murakami, 2006).

### EPFL nano-crystalline dye cell

Sample: 4

Aug 17, 1995 12:28 PM

ASTM E 892-87 Global

Temperature = 25.0°C

Area = 0.4000 cm<sup>2</sup>

Irradiance: 1000.0 Wm<sup>-2</sup>

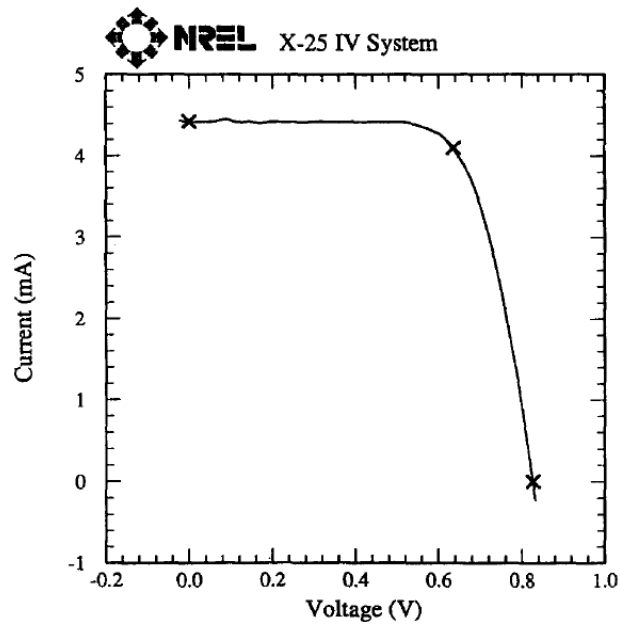


Fig. 4.1. I-V characteristic of a DSSC with a carbon-based cathode (A.Kay, 1996).

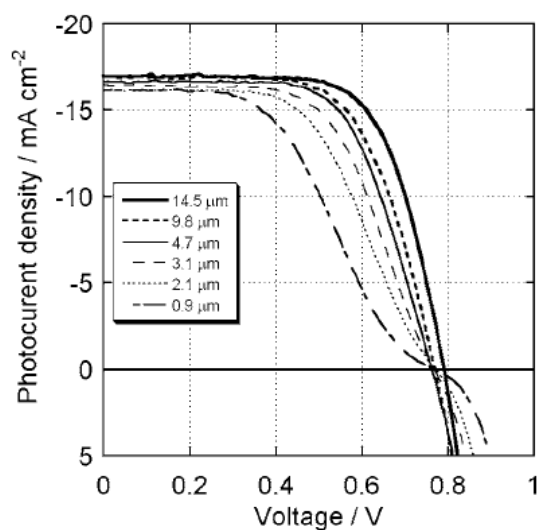


Fig. 4.2. Photocurrent-voltage curves of cells with carbon based cathodes. Different thicknesses of the carbon layers were tested (T. N. Murakami, 2006).

Indeed, Imoto et al. (K. Imoto, 2003) demonstrated that carbon activated based electrodes can be superior to a Pt sputtered electrodes as cathode in DSC. In particular, even if all the carbon-based cathodes were more resistive than the Pt one, the cells assembled with very high specific surface carbon materials showed a conversion efficiency even higher than the Pt-cathode ones. The good performance of such a material in devices has driven the research on the long term stability. The aging effects were studied both by monitoring the photovoltaic parameters and by impedance spectroscopy (E. Ramasamy, 2007) (W.J. Lee, 2008); after 60 days, even if the electrochemical spectroscopy measurements demonstrated the robustness of the carbon based cathodes, the overall conversion efficiency decreases more rapidly for carbon based cells rather than the Pt based ones. The faster degradation of carbon cathode DSSC in comparison to similar Pt ones was attributed to moisture content in carbon.

Among the carbon based materials, CNT are promising as the counter electrode of DSSC, thanks to their good catalytic activity and high electrical conductivity. The redox reaction

of iodide and triiodide has a low overpotential on CNT. Both single-walled CNTs (SWCNT) and multi-walled CNT (MWCNT) were reported as the counter electrode of DSSC (X. Mei, (2010) ). Two types of methods, dry and wet, were exploited to fabricate the CNT films on a conductive substrate, which is usually fluorine tin oxide (FTO) glass. The dry methods are based on the direct growth of CNT films on conductive substrate, whereas in the wet methods CNT are dispersed in a solvent with the assistance of a surfactant or a polymer and the films are fabricated by solution processing, such as spraying, vacuum filtration or a doctor blade. The wet processing method is more convenient and effective in making films over a large area; however, the CNT films in this case have a poor adhesion to substrates (L. Hu, 2009) (Y. Wang, 2008) (J.N. Bariscia, 2004) (M. Pacios, 2008) (X. Zhao, 2009) and detach from the substrates when immersed in an electrolyte. Hence, binders, such as epoxy and other polymers, are usually used to stabilize CNT films on substrates. But these inert binders can lower the catalytic and conductive capabilities of the CNT films since they reduce the contact area between CNT and electrolyte and block the inter-nanotube charge transport (B. Fan, 2008 ). Recently, it was discovered that CNT could form gels with some liquid organic compounds and binder-free CNT films could be fabricated by coating the CNT gels onto various substrates and then subsequently removing the organic compounds through heating (X. Mei, 2010). Those CNT films have good adhesion to substrates. The application of gel-coated binder-free films of both SWCNT and MWCNT, as the counter electrode of DSSC was presented in 2010 by Mei et al. (X. Mei, 2010). A power conversion efficiency over 8% and excellent stability over time were achieved on DSSC with a SWCNT film as the counter electrode, as shown in Fig. 4.3.

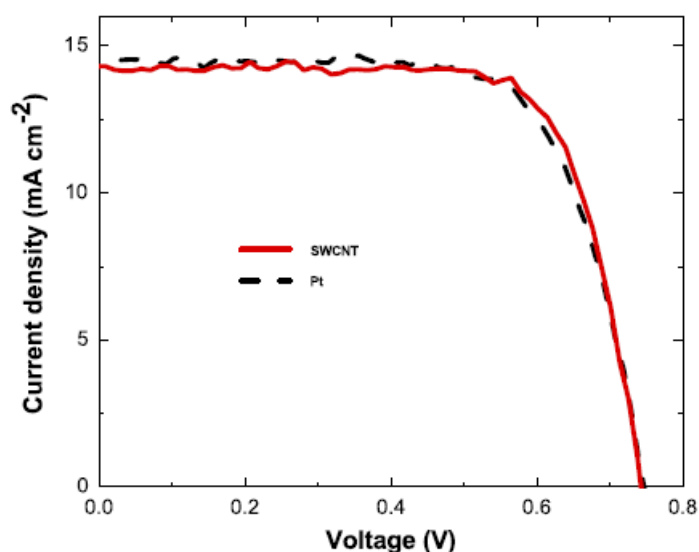


Fig. 4.3. current voltage curves of DSSC with Pt and SWCNT thick film as the cathode, under AM 1.5 illumination (X. Mei, 2010).

The functional properties of carbon materials employed at cathodes, e.g. the electrocatalytic activity, can be investigated by electrochemical techniques such as cyclic voltammetry (CV) and electrochemical impedance spectroscopy (EIS), as proposed in (K. Li, 2009).

The cyclic voltammogram for a SWCNT electrode is quite similar to that with Pt as the work electrode, as reported in Fig. 4.4. Two oxidation/reduction pairs can be observed in the CV. The pair in the potential range of 0.1–0.5 V versus  $\text{Ag}/\text{Ag}^+$  corresponds to the redox reduction of iodine and triiodide,  $3\text{I}_2 + 2e \rightarrow 2\text{I}_3^-$ , and the other pair in the potential range of –0.3 to 0.1 V versus  $\text{Ag}/\text{Ag}^+$  is the redox oxidation of iodide and triiodide,  $\text{I}_3^- + 2e \rightarrow 3\text{I}^-$  (K. Li, 2009). The species in the latter are the redox species in DSSC. The peak potential for the reduction of triiodide is the same for the two work electrodes, while the peak current with the SWCNT work electrode is even higher than that with the Pt work electrode. This indicates that the SWCNT film can effectively catalyze the redox of iodide and triiodide the same as Pt. Several papers report on both MWCNT and SWCNT as the counter electrode of DSSC. High photovoltaic performances of DSSC with CNT counter



electrode can be attributed to the high catalytic activity and electrical conductivity of those films prepared without any binders.

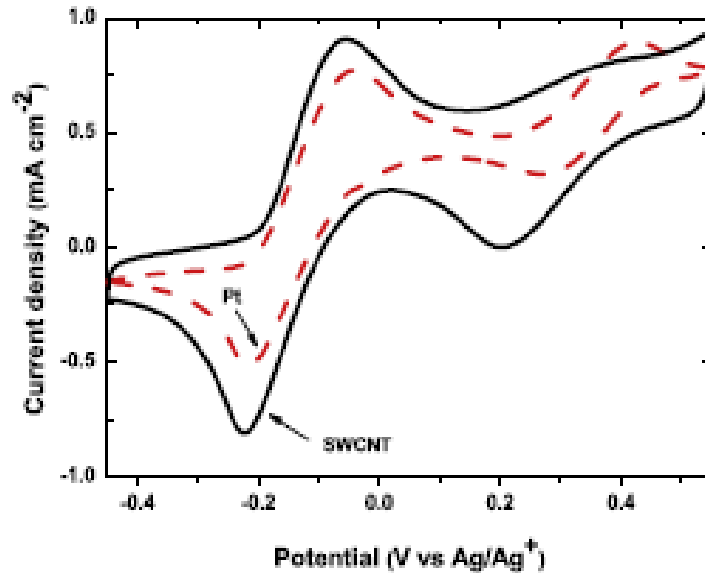


Fig. 4.4. CV of I2/I3- of Pt and SWCNT working electrodes [28].

The DSSCs with the SWCNT counter electrode exhibited good stability. No detachment of the SWCNT films from FTO glass was observed after one month. The photovoltaic stability was studied by testing the DSSC during an aging period of one month after the device fabrication. Results show an increase in the  $V_{OC}$  that caused an increase of the efficiency  $\eta$ , while the results obtained on a Pt based control DSSC exhibited a remarkable decrease in the efficiency. These results were explained in terms of higher stability of SWCNT electrode compared to the Pt one. CV was also used to test cathode stability: voltammograms of SWCNT electrode remain the same even after 100 cycles while a decrease in the current is appreciable in measurements on the Pt electrode. Finally, the paper reports on the better performance of the thicker CNT layer, confirming the necessity of using a several micron porous film thickness to achieve good performances. Murakami

et al. (T. N. Murakami, 2006) demonstrated that increasing the cathode carbon film thickness, the short circuit current was constant, while the fill factor in the I-V characteristics increased from 0.45 up to 0.7, as shown in **Fig. 4.2**. In the case of the thinner carbon layer, a “double diode” shape of the characteristic is the fingerprint of a improper catalytic cathode, leading the value of the FF below 0.45. In order to evaluate the catalytic performance of carbon electrodes, the charge transfer resistance for tri-iodide reduction can be measured by impedance spectroscopy. The authors modelled the impedance spectra by using an equivalent circuit made of a series of three parts, each describing an interface of the device. The values of the charge transfer resistance ( $R_{CT}$ ) at the cathode were found to decrease from 118 to 0.7  $\text{Ohm}\cdot\text{cm}^2$  increasing the thickness of the carbon layer. Because several phenomena in the complete device can occur at the same frequency, additional insight can be gained by measuring impedance spectra of dummy cells, that is in symmetric thin layer cell configuration, which consists of two identical carbon electrodes and interelectrode space filled with liquid electrolyte. The different values of the  $R_{CT}$  for carbon-based cathodes reported in literature, due to the different thickness, porosity, specific surface and binders vary from several tenths up to 20  $\text{Ohm}\cdot\text{cm}^2$ , often lower of Pt based cathodes, demonstrating that carbon nanomaterials have functional properties even better than Pt. Different experimental values are found by the different authors, but the most demonstrates the encouraging performance of carbon-based cathodes (S. Gagliardi, 2009) (E. Ramasamy, 2007) (W.J. Lee, 2008).

Very recently, graphene and graphene-based materials have emerged as potential catalysts for DSSC cathodes, due to graphene's high surface area and conductivity (J. D. Roy-Mayhew, 2010) (Y. Xu, 2008) (H. Choi, 2011). Hong et al. (W. Hong, 2008), for example, have used a chemically reduced graphite oxide derived graphene/poly-(3,4-ethylenedioxythiophene)-poly-(styrenesulfonate)(PEDOT:PSS) composite and achieved efficiencies of 4.5%, comparable to their platinum control cell at 6.3%. It has been suggested that oxygen-containing functional groups might be responsible for the observed catalytic performance of carbonaceous electrode materials, while the impact of the degree of material functionalization on apparent electrocatalytic performance has not been studied

in detail (B. Fang, 2010) (K. Suzuki, 2003) (J. G. Nam, 2010) (T. N. Murakami, 2008) (T. Denaro & A. S. Arico, 2009). Recently, a paper reported a thorough analysis of DSSC cathodes based on functionalized graphene sheets, which is a type of defective graphene currently synthesized at the industrial scale (B. Fang, 2010) via the thermal exfoliation of graphite oxide (GO), (M.J. McAllister, 2007) (H. C. Schniepp, 2006). Functionalized graphene sheets have a large surface area (up to  $2630 \text{ m}^2 \text{ g}^{-1}$ ) and contain lattice defects and oxygen-containing functional groups, such as hydroxyls, carbonyls, and epoxides, as shown in Fig. 4.5 The amount of oxygen-containing groups can be tuned by thermal processing of the material, thereby changing its carbon to oxygen (C/O) ratio. Thermal treatment up to  $1000^\circ\text{C}$  decreases the number of oxygen containing functional groups on the surface of the sheets and increases the graphene sheets conductivity. Furthermore, annealing at temperatures above  $1500^\circ\text{C}$  causes healing of lattice defects. The C/O ratio of the materials was varied systematically to examine its effect on the catalytic activity of the material.

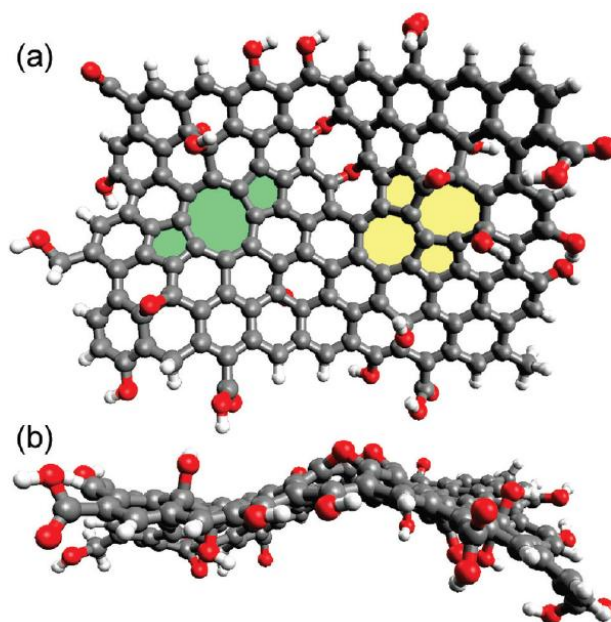


Fig. 4.5. Schematic of functional groups and lattice defects in graphene sheets. Epoxides and hydroxyls are on both size of graphene plane, while carbonyl and hydroxyl groups are at the edge. C atoms in grey, oxygen in red and hydrogen in white. Lattice defects of different nature are in yellow and green (J. D. Roy-Mayhew, 2010).

Roy et al. (J. D. Roy-Mayhew, 2010) demonstrated that DSSC assembled by employing graphene sheets as cathode material reach a conversion efficiency of 4.99%, which is more than 90% that of platinum-based control cell (5.48%). In view of the encouraging results with functionalized efficiency the graphene electrodes were electrochemically characterized in order to quantify their catalytic activity. The charge transfer resistance derived from impedance spectroscopy measurements were not consistent with photovoltaic performance: the values found for graphene electrodes were lower than that relative to Pt one; this results would imply higher fill factor and subsequently higher efficiency that was not verified. This evidence was attributed to the porous structure of graphene electrodes, that make the surface not always accessible. Cyclic voltammograms in more diluted electrolyte were then performed in order to disentangle surface accessibility from intrinsic catalytic properties (see fig. Fig. 4.6, Fig. 4.7).

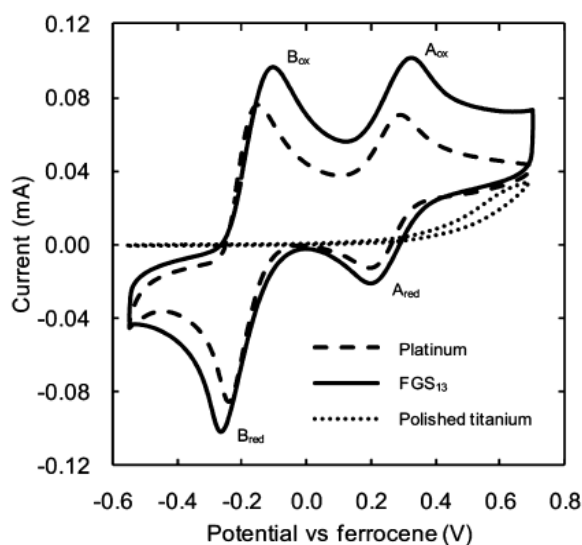


Fig. 4.6. CV of a Pt and a graphene film (FGS) on Ti foil, whose CV. Aox and Ared indicate oxidative and reductive peaks for  $I_2/I_3^-$  while Box and Bred indicate peaks relative to  $I^-/I_3^-$  (J. D. Roy-Mayhew, 2010).

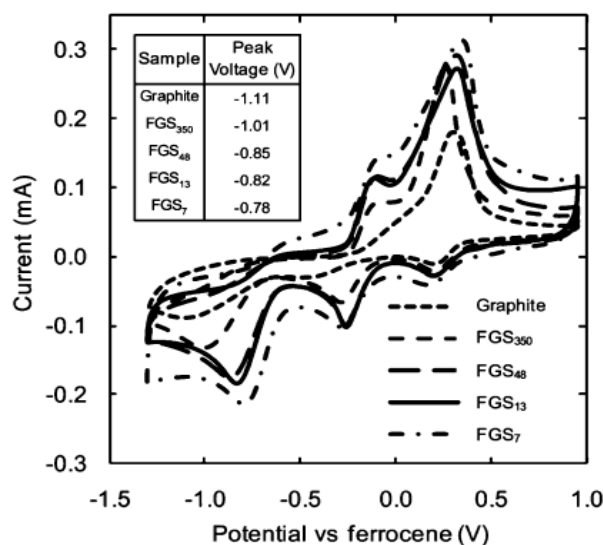


Fig. 4.7. Cv of graphene films with different C/O ratios; 7,13, 48 and 350. Cv of a sample of graphite is also reported. (J. D. Roy-Mayhew, 2010).

From the voltammograms the platinum-based electrode results to be more catalytic toward the reaction due to a lower overpotential, which supports EIS model and can explain the higher device efficiencies. The catalytic activity of graphene may be due to its large density of lattice defects and oxygen-containing functional groups. Therefore, it may be possible to further improve the catalytic activity of graphene based electrodes by tuning these potentially catalytic sites or even doping the graphene sheets with nitrogen, as proposed by several authors (Y. Xue, 2012). Doping graphene network with heteroatoms (as N, B or P) could introduce electrocatalytic sites with a minimized change of the conjugation length (D. Yu, 2010) and hence maintaining the electronic conductivity, unlike a chemical functionalization. Foam-like nitrogen doped graphene was tested as cathode material in DSSC, resulting in devices with conversion efficiency of 7.07%, compared to a Pt based control cell efficiency of 7.44%.

Two dimensional graphene based structures, usually identified as carbon nanowalls (CNW) or nanoflakes, are interesting for several possible applications due to their large

surface to volume ratio. In particular, they have shown a potential as functional supports of metallic clusters in electrochemical fuel cells (L. Giorgi, 2007) where different CNW morphologies were observed to have a large effect on the chemical activation of the supported metallic clusters.

In the framework of an existing research activity in ENEA UTTMAT-SUP laboratories on carbon-based nanostructures, several samples of CNW were synthesized, characterized and finally applied as cathode materials in DSSC.

## 4.2. SYNTHESIS AND CHARACTERIZATION OF CARBON NANOWALLS

Chemical vapour deposition techniques are widely used for the production of carbon nanostructures: from nanotubes to graphene and graphene-based materials such as nanoribbons and nanowalls. Starting from different carbon precursors ( $\text{CH}_4$ ,  $\text{C}_2\text{H}_2$ ...), without any catalyst, different methods of assisted chemical vapour deposition (CVD) can be used to grow nanowalls of graphene (M. Hiramatsu, 2010) (N. Lisi, 2011) such as hot filament plasma enhanced (HFCVD), dc and rf plasma enhanced, hydrogen arc discharge. Several authors showed that petal-like carbon nanostructures perpendicularly oriented to the substrate could be obtained by HFCVD from a mixture of  $\text{CH}_4$ ,  $\text{H}_2$  and Ar, applying a dc bias between the substrate and the filament; the effect of varying the filament temperature from 1800 to 2100 °C on the material surface morphology was also investigated, and it was pointed out that morphology can vary from small disordered needle-like clusters to a network of worm-like structures, and to larger and straight plates or foils. The growth mechanism of CNW remains not entirely understood.

Since graphitic carbon nanostructures have been successfully used as catalyst in DSSC, the possibility to achieve carbon coatings by HFCVD synthesis on conductive substrates for

such application was explored. In previous unreported experiments, some CNW grown on different substrates with thickness of several hundreds of nm were tested in DSSC that showed poor conversion efficiencies. The failure of this material was attributed prevalently to the low specific surface area, so that in this work only very thick samples (several  $\mu\text{m}$ ) of sponge-like carbon nanowalls were employed. The samples were grown in the Hot Filament CVD (HFCVD) reactor shown in Fig. 4.8. It consists of a vacuum chamber, a gas feeding apparatus, a substrate heater including a bias system and the filament assembly, as reported in Fig. 4.9.

In order to obtain very thick coatings the Ta filaments were then substituted by a single rod of graphite, 100 mm long, with 3 mm of diameter that allowed maintaining of high power conditions over long period.



Fig. 4.8. Picture of the HFCVD reactor.

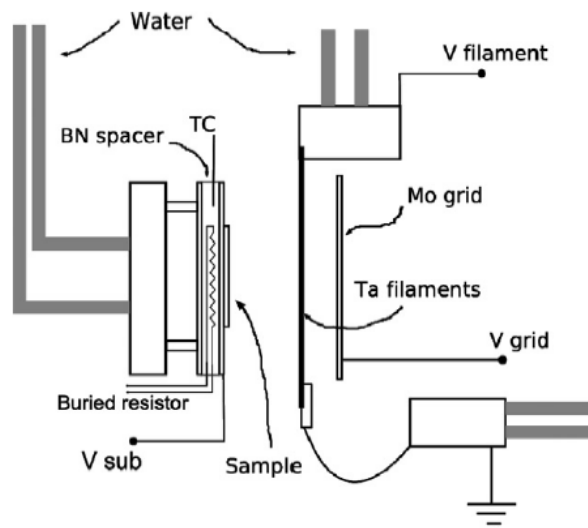


Fig. 4.9. Scheme of the filament grid assembly of the HFCVD reactor (N. Lisi, 2011).

The gas mixture ( $\text{He}$  and  $\text{CH}_4$ ) was fed into the reactor at 120 sccm by means of digitally controller flow meters, and the pressure was kept at 30mbar. All the samples were grown at 3% of  $\text{CH}_4$  the substrate was heated up to the growth temperature and the filament temperature was raised over  $2200^\circ\text{C}$ . Finally, a DC discharge was initiated between the filaments (ground) and the substrate (negative) with the help of an additional grid electrode (positive). The plasma power was kept at 240W during the process. All the deposition processes were performed at constant substrate current. In this thesis the synthesis and the characterizations of three different samples are reported, jointly to the results obtained by the application to real devices. Two of the samples tested were grown in the same process conditions (NW102, NW104), changing the deposition time and consequently the thickness. One more sample (NW103) was grown at higher temperature, but a severe deformation of the substrate occurred. Table 4-1 summarizes sample thickness, process temperatures and deposition time.



Sample	Thickness ( $\mu\text{m}$ )	Substrate temperature ( $^{\circ}\text{C}$ )	Deposition time (h)
TiC	-	600	0.25
NW102	7	600	7
NW103	3.2	800	3
NW104	3.6	600	3.5

**Table 4-1. CNW samples.**

Ti foils (0.3 mm thick, 5 cm diameter, 99.6% pure, from GoodFellow) were used as substrates. The choice was driven by the necessity to employ a flat, heat resistant, conductive substrate, resistant to corrosion phenomena occurring in the electrolyte. The samples were characterized by Raman spectroscopy and SEM before the employment in device. The thickness of the samples was calculated from the knowledge of the deposition rate (0.9  $\mu\text{m}/\text{h}$ ). A “control” cathode (TiC) was also prepared by stopping the growth after only 5 minute of process. The control sample has a very thin carbon coating and is used as non-catalyzed cathode for DSSC. A very thin film of carbon has not a proper electrocatalytic activity and the I-V characteristics of DSSC employing such a cathode have very low FF, as reported by Murakami *et al.* (Murakami 2006).

SEM micrographs were obtained using a field emission gun SEM LEO 1530, equipped with an in-lens detector. The morphology of the samples, very similar for all the samples, is uniform over the whole substrate area. Few stacked graphene layers form a disordered honeycomb structure perpendicular to the substrate. In order to better distinguish the tips of the samples, they were tilted by  $53^{\circ}$  (Fig. 4.10b, Fig. 4.11b, Fig. 4.12b), the transparency putting in evidence the thinness. The “control” sample (image not reported) showed the absence of a carbon film, or a totally electron-transparent thin layer, on the Ti foil.

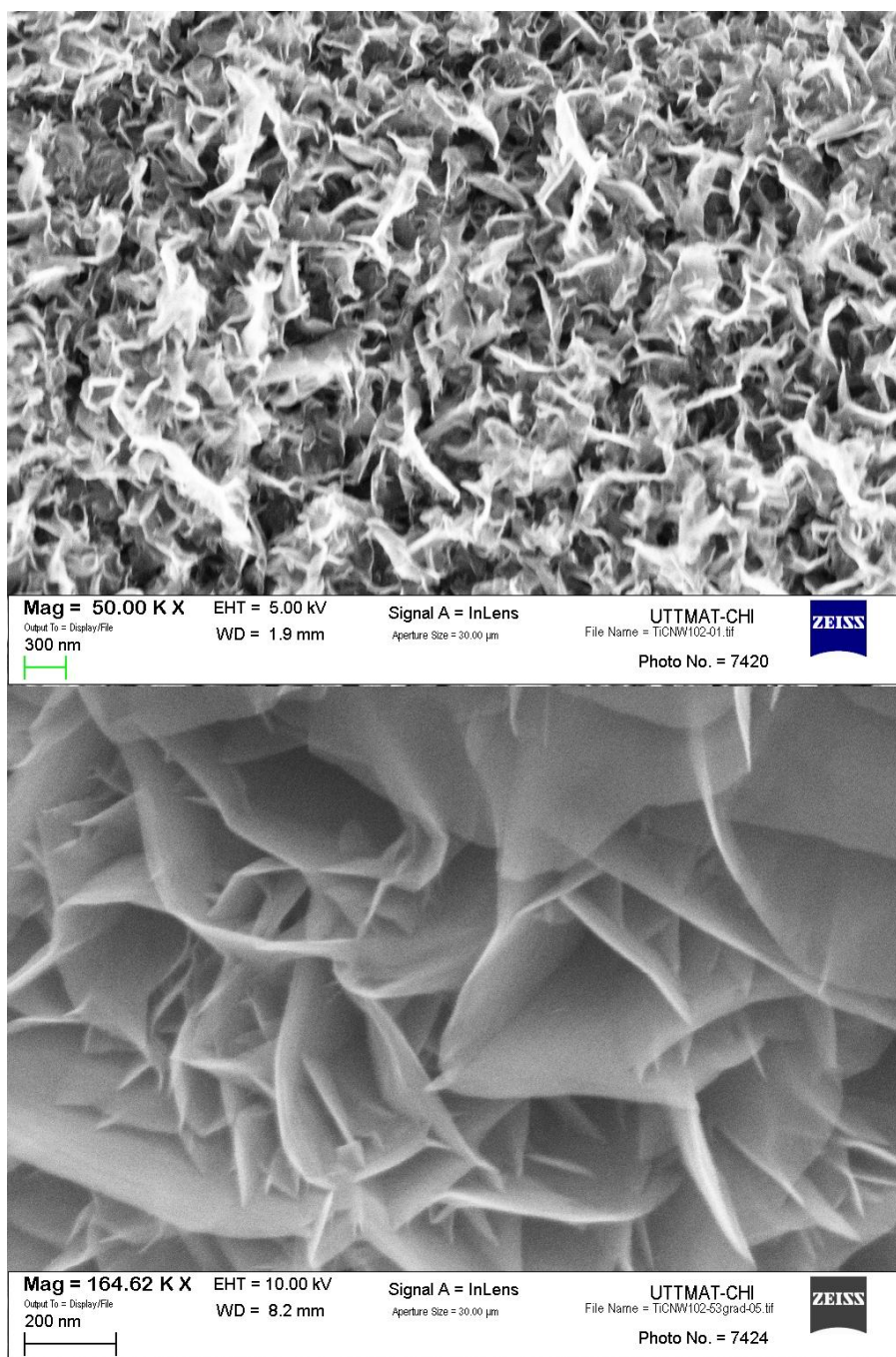


Fig. 4.10. SEM micrographs of sample NW102, CNW on Ti, taken perpendicular to the substrate (a) and after 53° tilting (b).

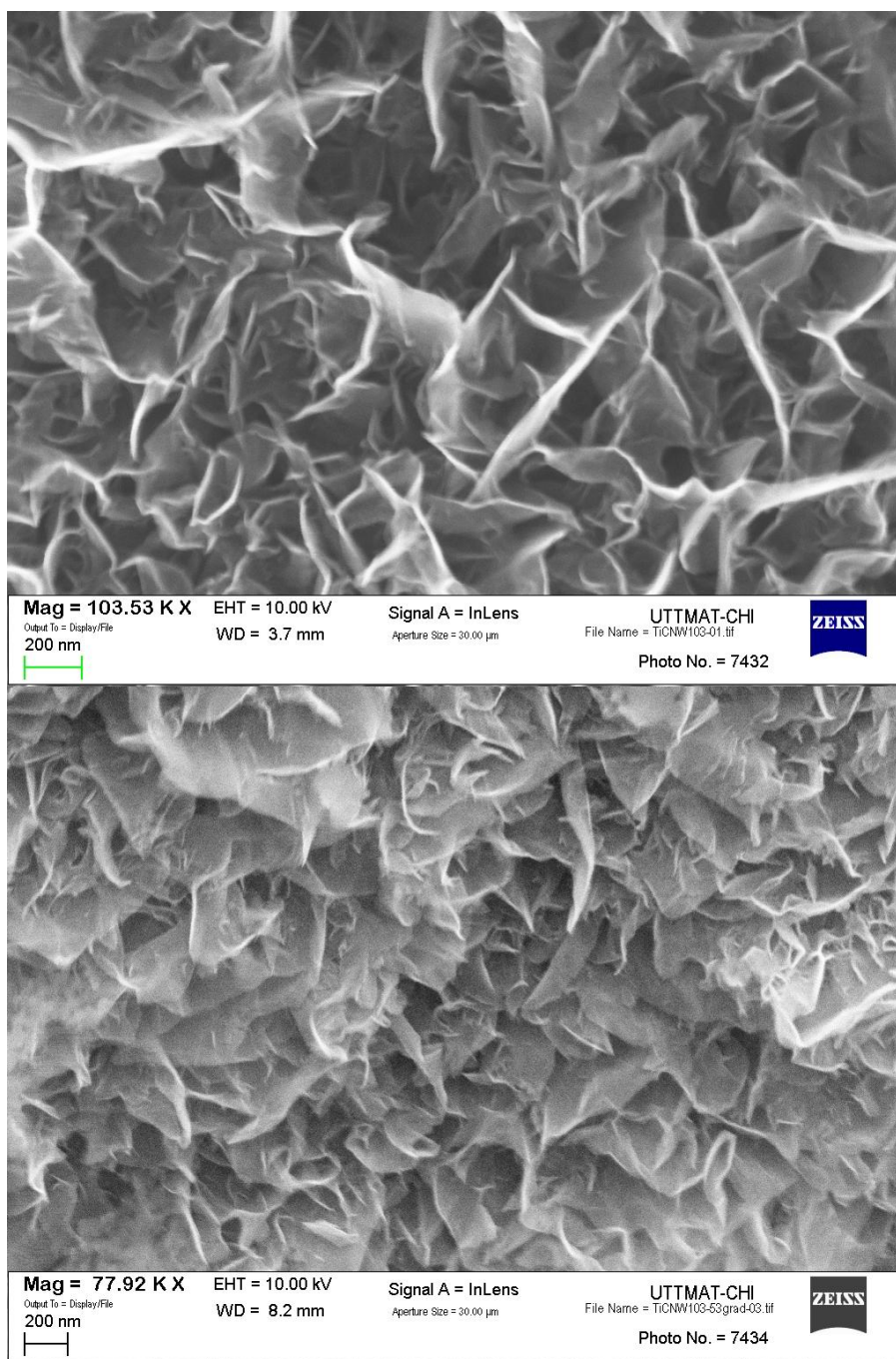


Fig. 4.11. SEM micrographs of sample NW103, CNW on Ti, taken perpendicular to the substrate (a) and after 53° tilting (b).



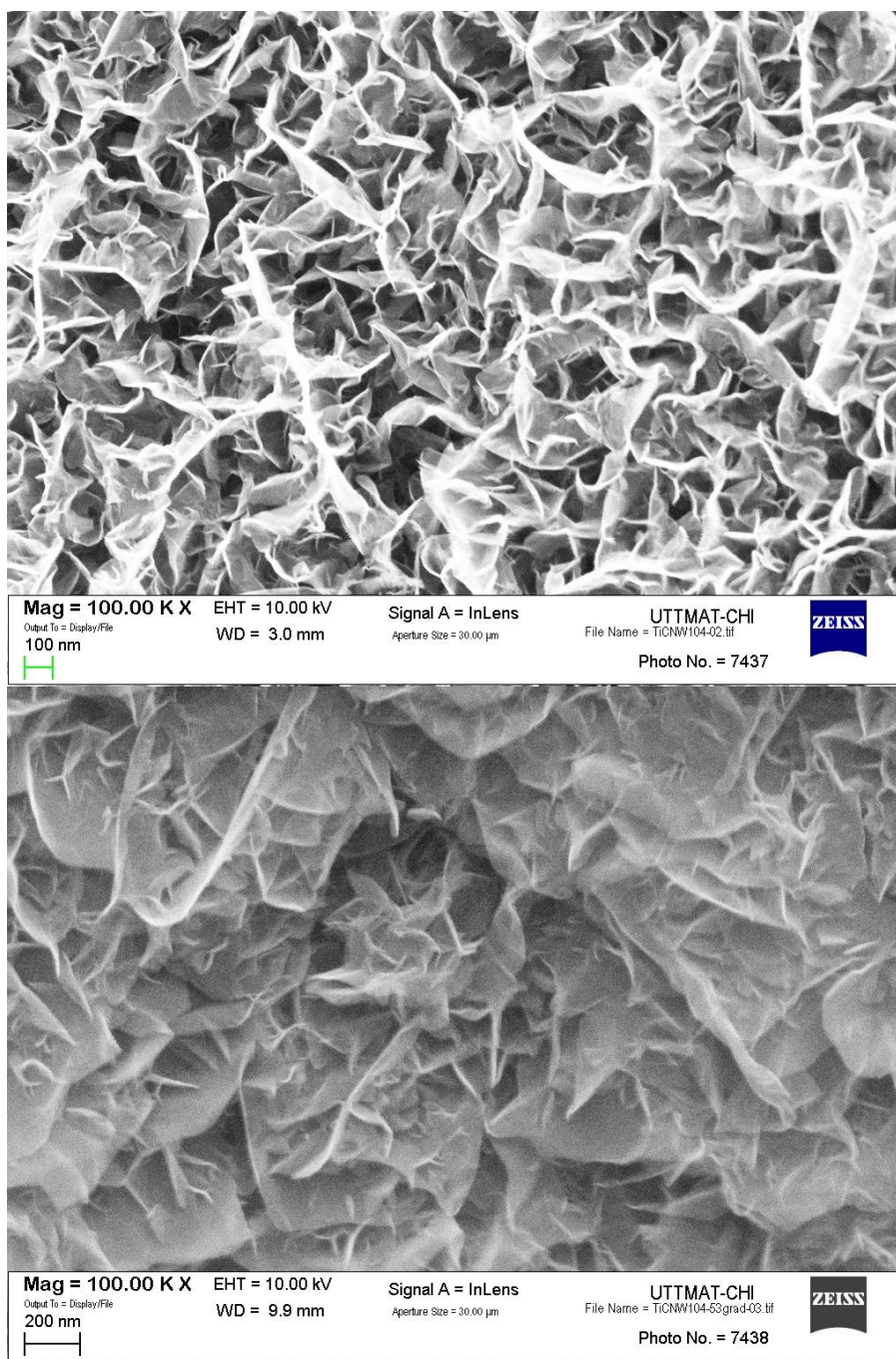


Fig. 4.12. SEM micrographs of sample NW104, CNW on Ti, taken perpendicular to the substrate (a) and after 53° tilting (b).

Raman spectroscopy is widely used to characterize carbon and nanocarbon specimens, due to its capability to distinguish the  $sp^3$  (diamond-like) or  $sp^2$  (graphite-like) bonds between C atoms. The graphite spectrum is characterized by two quite sharp modes, the so-called G-band, centred at about  $1600\text{ cm}^{-1}$ , associated with the doubly degenerate (iTO and LO) phonon mode ( $E_{2g}$  symmetry) at the Brillouin zone centre; the G' band usually called 2D band at about  $2700\text{ cm}^{-1}$  involving two iTO phonons near the K point in a second-order process; in the case of a disordered sample or at the edge of a graphene sample, the so-called disorder-induced D-band appears at about half of the frequency of the G' band (about  $1350\text{ cm}^{-1}$ ) originating also from a second-order process, involving one iTO phonon and one defect. Another disorder-related weak feature appears at about  $1620\text{ cm}^{-1}$ . The ratio of the intensity of the D band to that of the G band is a direct measure of the dimension of the average crystalline domains as demonstrated by Cancado (L.G. Cancado, 2008) (F. Tunistra, 1970) (A.C.Ferrari, 2000).

The Raman spectrometer is based on a 550 mm grating monochromator (Jobin-Yvon TRIAX 550) coupled to a liquid nitrogen cooled CCD detector. The sampling head is a home-built micro-Raman setup equipped with a notch filter for rejection of elastically scattered light, and coupled to the monochromator-detector assembly by an optical fibre. The objective is a 32x long-working-distance device allowing to focus the 532 nm laser excitation light to an approximately  $3\text{ }\mu\text{m}$  large spot.

Results for the samples produced using different reaction conditions are shown in Fig.4.13, after normalization to the G-peak of each spectrum.

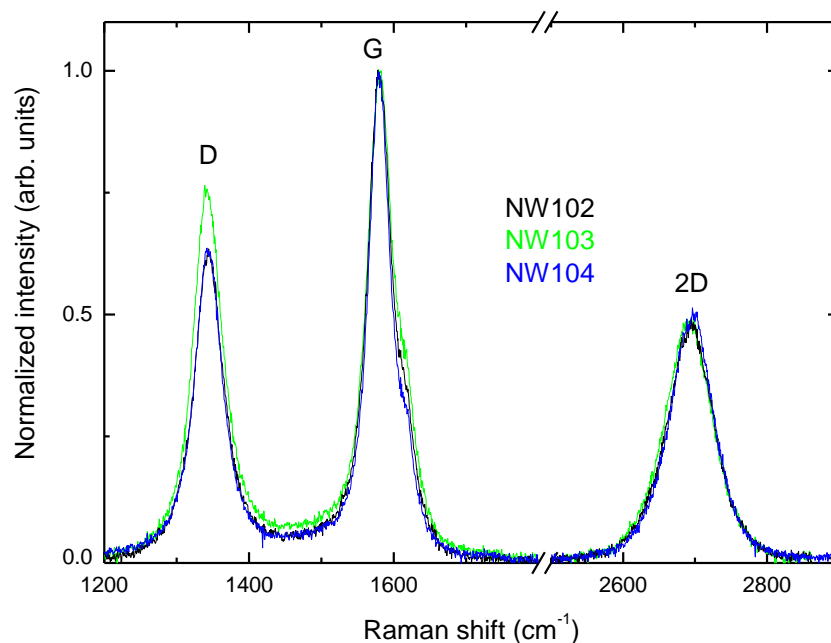


Fig. 4.13. Raman spectra of CNW samples.

The spectra are similar to that of carbon nanotubes and quite different from that of highly oriented pyrolytic graphite, according to the literature results, showing the highly disordered graphitic nature of the samples. In particular, from the structural point of view, sample NW102 and NW104 resulted to be identical, while NW103 has a larger number of defects, as evident from the higher intensity of the D band and of the shoulder at  $1620\text{ cm}^{-1}$ . The slightly higher structural disorder appearing in NW103 cannot be not trivially related to the differences appraised in SEM micrograph and further investigations have to be carried out in order to clarify the nature of the difference. Finally, the control sample has a Raman spectrum (not reported) that puts in evidence the presence of D and G peaks hardly emerging from the noise fluctuations, confirming the presence of very thin disordered graphitic coating. The samples were then tested as material for cathodes in real DSSC.

### 4.3.DEVICE CHARACTERIZATION

The CNW samples after non destructive characterizations were employed as cathodes to realize complete DSSC without any further treatments. Two twin complete cells were realized by employing each sample as cathode. In order to refill the cell, to avoid drilling Ti foils, the hole was drilled in the photoanode supporting FTO. The procedure to prepare standard photoanodes and to assemble the cell was described in chapter 3. At the sealing step, some difficulties were encountered, since Surlyn<sup>®</sup> foil could not adhere to the NW surface. As a consequence, Surlyn<sup>®</sup> frames were inserted in the cell as spacers between the electrodes and the sealing was obtained by EVA glue, usually used only for the final sealing of the filling hole in the electrode.

The cells were characterized under standard AM1.5 solar illumination and the characteristics are shown in Fig.14 a, b, c.

The relevant photovoltaic average parameters are summarized in Table 4-2 and the average curves are reported for comparison in the same plot 4.15 with a “control” cell, where a Ti foil without nanocarbon coating was used as cathode.

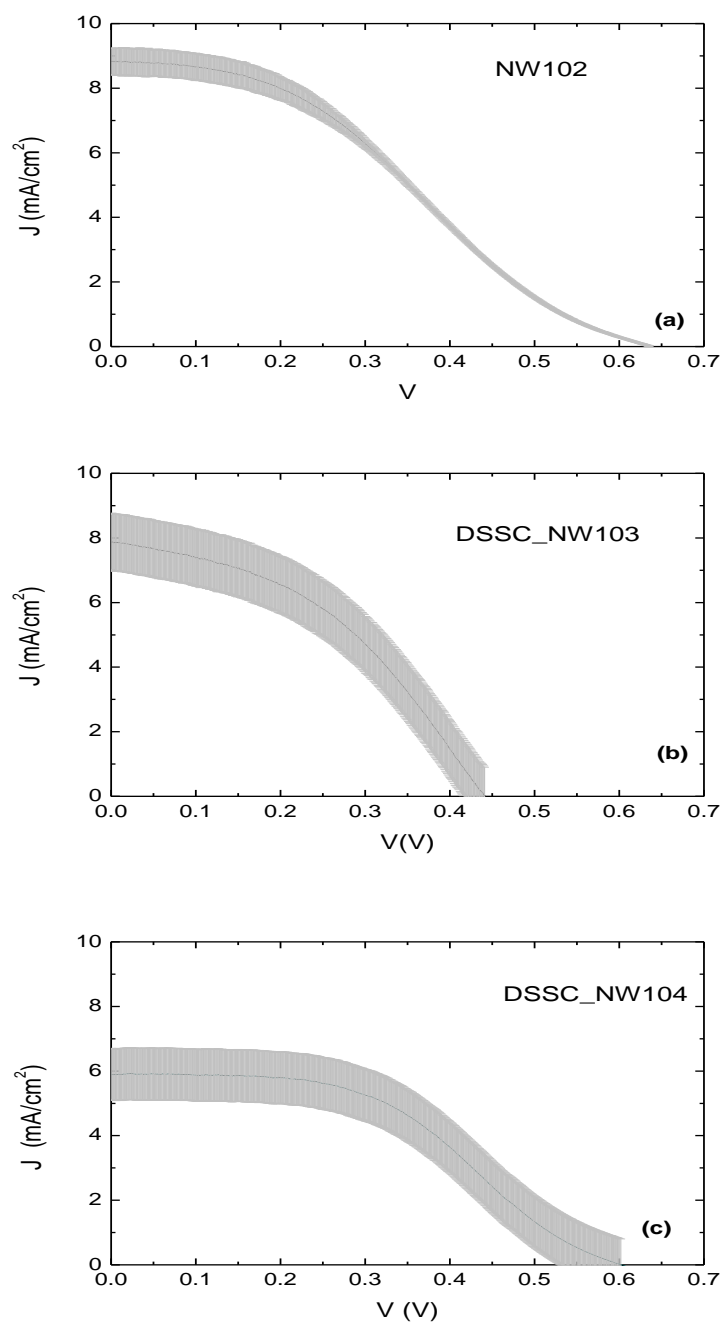


Fig. 4.14. Current density to voltage characteristics under illumination of DSSC with CNW based cathodes. Black line represents an average value of different samples. Error bars are reported in grey.



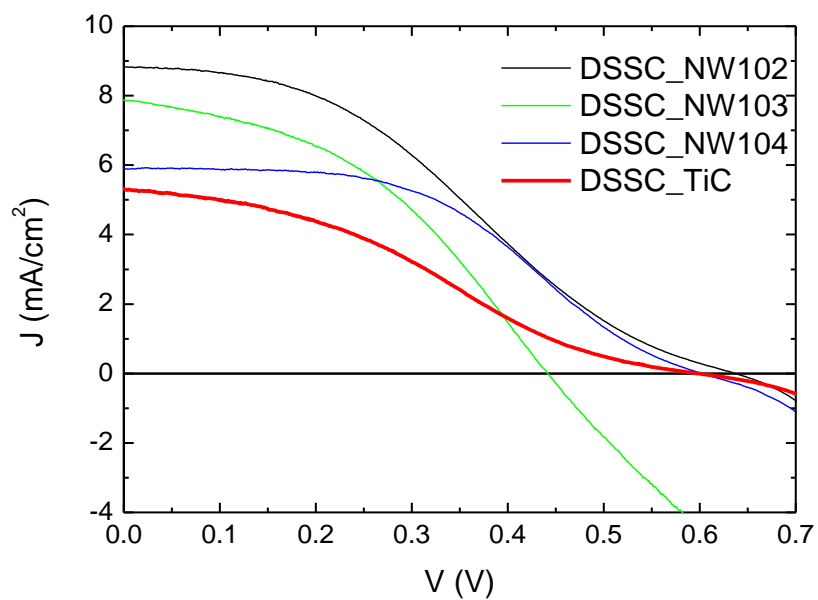


Fig. 4.15. Comparison between J-V characteristics of different DSSC.

Sample	$V_{oc}$ (V)	$J_{sc}$ (mA/cm <sup>2</sup> )	FF	$\eta$ (%)
DSSC_NW102	0.64	8.8	0.3	1.9
DSSC_NW103	0.44	7.8	0.4	1.5
DSSC_NW104	0.60	5.9	0.5	1.6
DSSC_TiC	0.60	5.3	0.3	1.0

Tab. 4-2. Relevant average photovoltaic parameters of the DSSC tested.

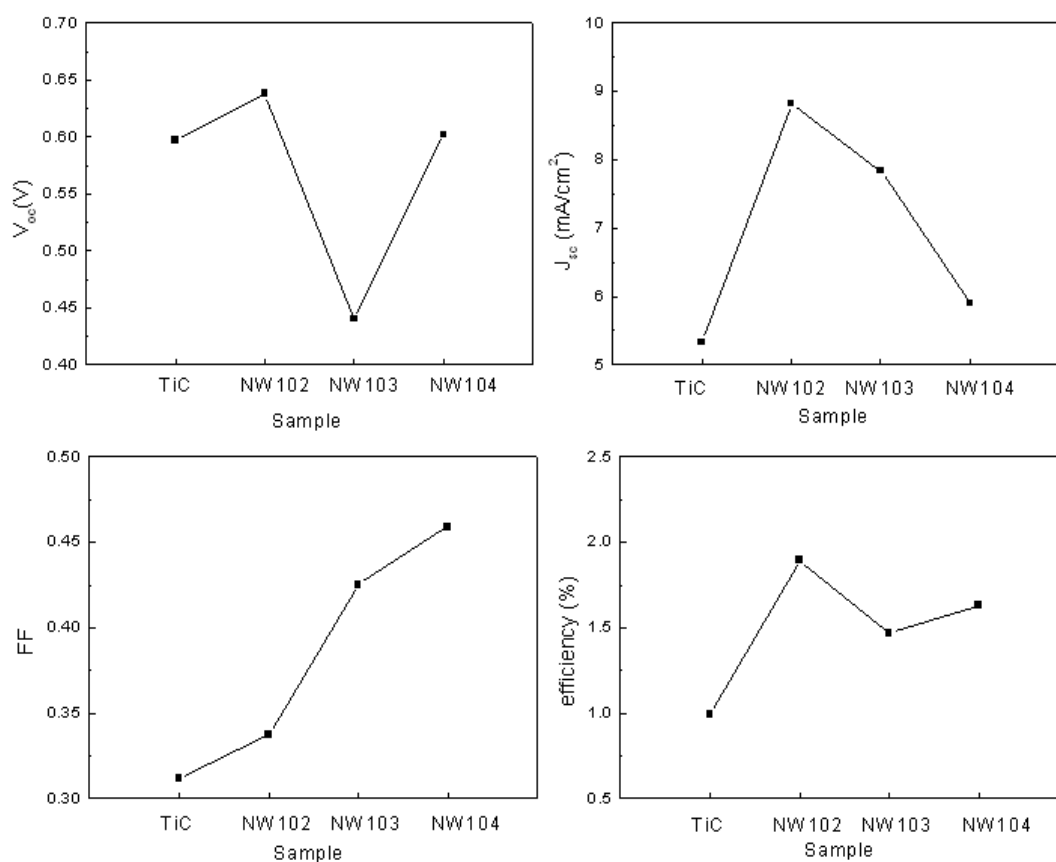


Fig. 4.16. Relevant photovoltaic parameters assigned to the corresponding cathode.

#### 4.4.DISCUSSION

The J-V curves showed in fig. 4.15 have quite different shape, even if all of them present a “double diode” shape common to DSSC that have cathode not properly catalyzed. An attempt to compare the relevant photovoltaic parameters as a function of the different cathodes (Fig.4.16) is reported in fig 4.16. As expected from the common nature of all the cathodes (carbon nanostructures on Ti) the open circuit voltage is almost the same for all the devices, except in the case of sample NW103, which has a very low  $V_{oc}$ . This case can be explained in relation to the severe deformation of the Ti substrate that affects the proper assembly of the device, and consequently its proper operation. It should be concluded that,

for CNW grown at process temperature above 600°, the deformation of the substrates makes impossible the use of such samples as cathodes in DSSC. Future attempts are to be focused on processes at lower temperature, and possibly allowing the synthesis of porous “low density” graphitic structures.

The shape of the J-V curves, diverging from those of properly catalyzed DSSC, can be “quantified” by the value of the FF, that remains well below 0.5 for all the cells and that of course affects the overall conversion efficiency of the device. Samples NW102 and NW104, grown at the same temperature (600°C) have a poor catalytic activity (FF<0.5, and “double diode shape”) but with the overall efficiency that is higher for the thicker cathode (NW102), as expected, encouraging on the route of structured and thick (e.g. high surface area) cathodes.

The short circuit current density should be independent from the cathodes (as extensively treated in chapter 5), being principally dependent on the absorption characteristics of the photoanode. Nevertheless, the very low values obtained with the non-catalyzed cathode (TiC) and even with samples NW102 and NW104, show that the processes occurring at the cathode severely influence even the photocurrent.

It is clearly evident at this stage that several functional and morphological characterizations of the carbon nanomaterials are necessary to properly assess their suitability for DSSC application, before the final testing in a complete device.

In conclusion, CVD synthesized carbon nanowalls have been tested as materials for DSSC cathodes. Samples were grown as thick films on Ti. This choice exploits both the high conductivity of the substrate and a potential high surface area necessary for efficient operation; however, the material, tested in real devices does not show a high catalytic activity. Studies are in progress in order to change the deposition parameters in order to achieve samples with higher specific surface area; in parallel possible treatments post-grown capable to activate catalytic reaction centres are under studies; a series of functional characterizations, such as measurements of electrocatalytic surface area and electrocatalytic activity, have to be exploited to optimize the material before the use in a real device.

## Chapter 5. Photophysics of conventional anodes

*The interaction between solar radiation and photoactive layer in photovoltaic cells plays a crucial role in the device conversion efficiency. A proper knowledge of the optical characteristics of the photoanode is critical for the comprehension of the whole device performance and constitutes one of the starting points when innovative materials are studied and developed. In this chapter the light trapping phenomena occurring in photovoltaic cells are discussed in term of the advantages in conversion efficiency and recent results on light management strategies are reported.*

*The main content of this chapter is the assessment of the optical functionality of the DSSC photoanode, based on a joint theoretical and experimental approach. The validity of the results deriving from the pure optical description is discussed in comparison to the results obtained in I-V characterization of real complete devices.*

### 5.1.THEORETICAL BACKGROUND AND REVIEW

The photocurrent collected at each wavelength relative to the rate of photons incident on the device at the wavelength determines the spectral response of the cell. The internal spectral response (SR) is defined as the number of electrons per second collected under short circuit conditions divided by the flux of photons entering the active layer, while the

external response (usually called incident photon to electron conversion efficiency, IPCE) is the internal SR modified by the (spectral) reflection of light from the surface of the device,  $R(\lambda)$  (H.Hovel 1975):

$$\text{IPCE}(\lambda) = \text{SR}(\lambda)[1 - R(\lambda)] \quad (1)$$

The reflection of light from the surface as a function of wavelength enters therefore into the experimentally observed spectral response.

In addition to its value as a tool in studying solar cells, the SR can be used to compute the expected short circuit photocurrent,  $J_{sc}$  for any given spectral input. Since the spectral response represents the number of carriers collected per incident photon, the photocurrent density per unit bandwidth at a given wavelength is given by:

$$J(\lambda) = qF(\lambda)\text{IPCE}(\lambda) \quad (2)$$

where  $F(\lambda)$  is the incident light spectral distribution and  $q$  the electron charge. The total photocurrent is obtained by integrating (2):

$$J_{sc} = q \int_0^{\infty} F(\lambda) \text{IPCE}(\lambda) d\lambda \quad (3)$$

The idealized photocurrent that would be obtained by conversion of all incident photons up to a certain wavelength, into collected electrons can be calculated from (3) setting the IPCE equal to unit.

The  $\text{IPCE}(\lambda)$  is determined by three factors: the light harvesting efficiency  $\eta_{LH}$ , the electron injection efficiency  $\eta_{inj}$  and the electron collection efficiency  $\eta_{COL}$ :

$$\text{IPCE}(\lambda) = \eta_{LH}(\lambda) \eta_{inj}(\lambda) \eta_{col}(\lambda) \quad (4)$$

While collection and injection efficiencies can be considered to be independent from the wavelength, light harvesting efficiency strongly depends on the latter and is related to the optical properties of the device. Assuming  $\eta_{inj}(\lambda) = \eta_{col}(\lambda) = 1$ , the light harvesting efficiency is:

$$\eta_{LH}(\lambda) = [1 - R(\lambda)] A(\lambda) = IPCE(\lambda) \quad (5)$$

where  $R(\lambda)$  and  $A(\lambda)$  are respectively the reflectance of the device and the absorbed fraction of the active layer. Equation (4) can be written as:

$$J_{sc} = q \int_{\lambda_{min}}^{\lambda_{MAX}} F(\lambda) (1 - R)A(\lambda) d\lambda \quad (6)$$

Since the efficiency of the solar cell is given by

$$\eta = J_{sc} \times V_{oc} \times FF \quad (7)$$

an increase of  $J_{sc}$ , through the optimization of the optical functionality, leads to an improvement of  $\eta$ .

Thin film solar technology, as previously mentioned, substantially reducing the costs of the device, could allow a wider diffusion of PV as energy production strategy. Unfortunately, the thickness reduction causes a severe loss in device performance, essentially due to the reduction of light absorption inducing a decrease of the photogenerated current. In order to overcome this problem, light trapping technique can be exploited: the dwelling time in the active region of incoming photons has to be prolonged increasing the probability of being absorbed before escaping by transmission or reflection outside the device.

### **Light trapping**

Increased absorption deriving from the tendency of light to be trapped by multiple internal reflections in semiconductors with textured surfaces was first exploited in silicon photodetectors and solar cells (John 1969) (Redfield 1974). In 1981, Yablonovitch (Yablonovitch 1982) proposed the first analytical approach to quantify the effect of light trapping on the interaction of radiation with scattering materials, focussing on the optical properties of media having complicated surface shapes, or random surface structures. He adopted a statistical ray approach assuming that the behaviour of the light rays is ergodic, i.e., at steady state, the temporally averaged, light intensity distribution will be identical with a statistical phase-space intensity distribution. In Yablonovitch's approach an optical slab with refractive index  $n$  is in equilibrium in the external black-body radiation, whose electromagnetic energy density is described by the Planck formula:

$$U = \frac{\hbar\omega}{e^{\hbar\omega/k_B T} - 1} \frac{2d\Omega k^2 dk}{(2\pi)^3} \quad (8)$$

Landau and Lifshitz (D. Landau 1969) demonstrated that in an optical medium Planck formula can be adapted by placing  $k=n\omega/c$ . It can be demonstrated that inside the optical slab the intensity of light ( $I_{\text{int}}$ ) differs from the vacuum blackbody radiation ( $I_{\text{ex}}$ ) by a factor  $n^2$ :

$$I_{\text{int}} = n^2 I_{\text{ext}} \quad (9)$$

The maximum enhancement factor has to be multiplied by a factor 4 when considering bulk absorption, so it can be written as:

$$\gamma = 4 n^2 \quad (10)$$

The ultimate limit to light trapping calculated by Yablonovitch was generalized by Green in 2002 (Green 2002), who formulated the exact analytical solutions for both weakly and strongly light absorbing materials and extended the results both to absorbing and emitting materials, in view of both solar cells and light emitting diodes applications.

Since a major limitation to solar cell efficiency is the long absorption length of long wavelength photons and the small absorber layer thickness, in recent years, many solutions have been suggested to implement light trapping schemes, for overcoming the poor light absorption of thin film solar cells near the band gap (see Fig. 5.4) (D. Zhou 2008), and in particular for the indirect-bandgap semiconductor Si.

Enhancing light-trapping in thin film solar cells is typically achieved by a textured metal backreflector that scatters light within the absorber layer and increases the optical path length of solar photons.

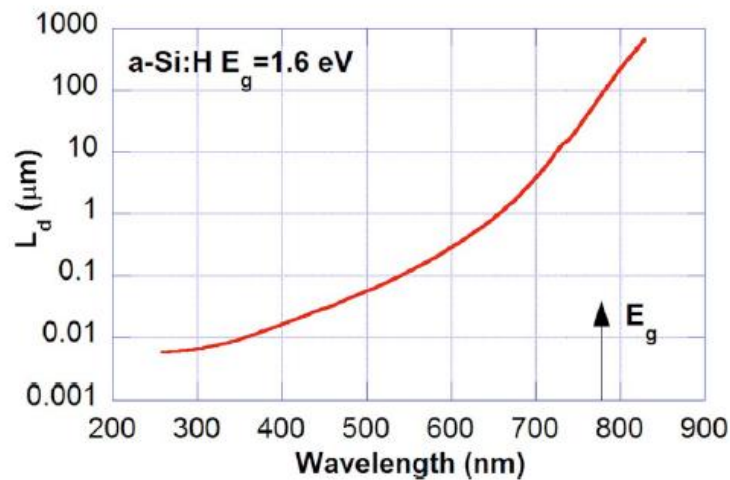


Fig.5.1. Absorption length of photons as a function of wavelength for a-Si:H with band-gap  $E_g=1.6$  eV (D. Zhou 2008).

Besides the exploitation of enhanced light absorption due to disordered surfaces many papers report on use of plasmonic metallic structures (D.M. Callahan 2012) (R. Catchpole 2008) (Polman 2008) (H.A. Polman 2010) (K. Nakayama 2008) (T. Reilly 2008) and



dielectric structures (Bozzola A 2011) (D. Zhou 2008) (D. Zhou 2008) (R. Biswas 2011), (M.D. Kelzemberg 2010). Engineered surface structures, in fact, enable to enhance light absorption in selected range, where the intrinsic absorption of the active material is low, even beyond the ray optic limit.

In DSSC, the most commonly used dye, N719 has a low absorption coefficient for red or longer wavelengths. To compensate for this, it has become a standard practice to use diffuse light scattering to increase the optical path length in the cell at long wavelength.

All the high efficiency cells reported in literature exploit LT both incorporating an additional scattering film (S. Ito 2006) (F. Gao 2008) (Y. Chiba 2006) to reflect back the light not yet absorbed in the active layer, and embedding scattering particles in the active layer to increase by diffusion the light path wavelengths (F. Gálvez 2006) (A.G. Agrios 2006) (K.M. Lee 2006) (F. Huang 2010). Nevertheless, light management strategies are usually exploited on the basis of empirical evidence and accurate systematic approach is not yet applied.

The beneficial presence of light diffusion was first theoretically analyzed by Usami (Usami 1997) (Usami 2000) and Ferber (J. Ferber 1998). The exact solution of light scattering by a particle was obtained by Mie but, since it applies to an isotropic and homogeneous sphere, it is not adequate for the  $\text{TiO}_2$  porous film. Usami examined scattering of a single titania particle, then deduced contributions from multiple particles with the Monte Carlo simulation method. The result indicated that optimal conditions for backscattering were consistent with the total reflection at interface between  $\text{TiO}_2$  thin film and the glass substrate. This led to the conclusion that a useful optical confinement in active layer can be obtained by inserting  $\text{TiO}_2$  (rutile phase) thin film between the FTO and glass substrate, and putting a film with large particles onto the thin film as shown in Fig. 5.2.

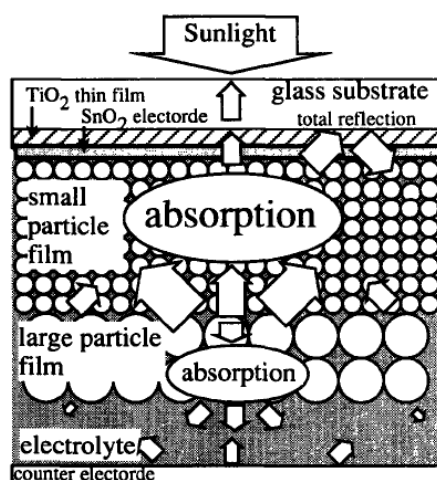


Fig.5.2. Schematic image of the structure proposed by Usami (Usami 1997).

Optical properties of electrodes composed by a mixture of small (10-25 nm) and large (600-800 nm) were analyzed by Ferber. He found that the optimum optical behaviour is obtained adding to a small-particles based electrode 5% of larger particles with radius of 125-150 nm, as can be seen in Fig. 5.3.

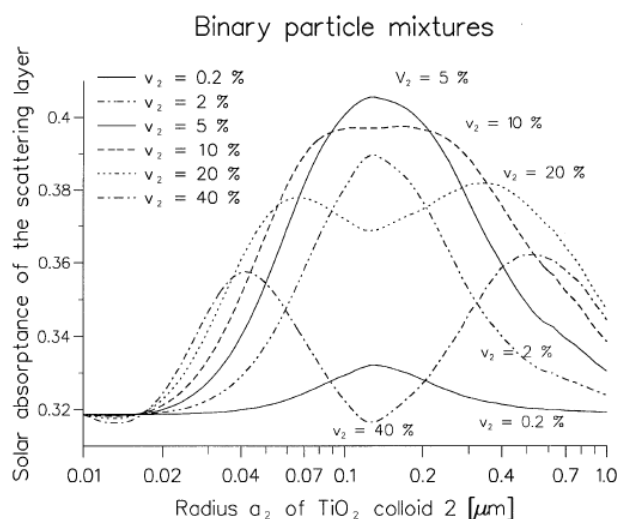


Fig. 5.3. Calculated optical absorption of binary mixture of particle with size  $a_1=10\text{nm}$  and  $a_2$  variable (Ferber 1998).

Finally Rothemberger et al. (Rothemberger 1999) proposed a careful optical characterization of porous thick titania electrodes and an optical model that allows the interpretation of experimental data. Moreover, they calculated a hypothetical maximum photocurrent density, assuming that each absorbed photon yields a collected electron, even if they did not compare the results from optical characterization to the performance of the titania electrodes in device.

## 5.2.PHOTOANODE OPTICAL FUNCTIONALITY

As discussed above, one of the keys in efficient photovoltaic conversion is related to the optical properties of the photoactive material. Moreover, we have briefly discussed how light trapping phenomena occurring in photovoltaic devices, enhancing light absorption, influence the overall conversion efficiency.

The knowledge of the optical functionality can therefore help in the optimization, characterization and design of a material in the framework of its application in PV as active layer.

From the point of view of optical functionality, in a dye sensitized solar cell, the monolayer of dye molecules adsorbed on titania surface constitutes the active material, while the nanostructured  $\text{TiO}_2$  impacts on the light trapping. In the following, a conventional nanobeads-based DSSC PA was studied trying to disentangle absorption these two phenomena, i.e., absorption due to the bare dye load and light trapping due to the bare titania layer.

To this aim, a model electrode composed of titania nanospheres was developed to calculate the specific surface area and hence the number of N719 molecules adsorbed as a monolayer. This allowed to calculate the short circuit photocurrent density of an ideal DSSC ( $\eta_{\text{inj}} = \eta_{\text{col}} = 1$ ) based on the model PA:

- i) neglecting any light trapping phenomenon or
- ii) considering the limit light trapping stated by Yablonovitch.

Light trapping properties of a real conventional PA were experimentally quantified by means of optical spectrophotometry, calculating the light absorbed fraction from reflectance and transmittance measurements, and accounting for the dye load obtained by desorption analysis. The relevant parameter obtained from such experimental characterization is the spectral dependence of the absorption enhancement factor provided by LT.

The results of the optical model and of the characterization of PA are discussed in relation to the I-V characteristics of a real cell.

### 5.2.1. Optical model

The first step was the description of the geometry of the electrode in order to estimate the surface area available for dye anchoring. The electrode was schematized as a parallelepiped, having as base the surface area of the device ( $1\text{cm}^2$ ) and height equal to the thickness of the mesoporous titania film ( $10\text{ }\mu\text{m}$ ).

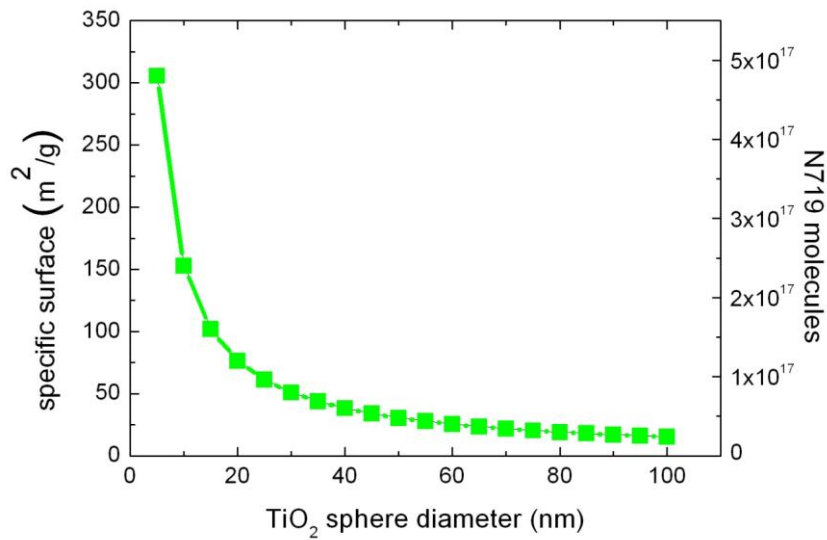


Fig. 5.4. Specific surface and dye load calculated for a  $10\text{ }\mu\text{m}$  thick electrode with geometric surface of  $1\text{cm}^2$ .

In the model the volume of the electrode was then filled with spheres. Given the titania (anatase phase) density ( $\rho=3.9\text{g/cm}^3$ ), and setting the packing density of the sphere equal to 0.64, according to (G. D. Scott 1969), we calculated the specific surface area of particles with diameter varying from 5 to 100 nm. Since a molecule of the dye used in this work, N719, has a footprint of  $160 \text{ \AA}^2$  (M.J.Griffith 2011) we also calculated the number of molecules adsorbed on the titania surface, arranged as a compact monolayer, coating all the available surface. The graph in Fig.5.4 reports the specific surface area and the number of adsorbed N719 molecules calculated as a function of  $\text{TiO}_2$  particles diameter.

The absorbance spectrum of the dye was experimentally determined by measuring in the visible range the transmittance of an alcoholic solution with a known molarity. The experimental spectrum was used to calculate the absorbed fraction of light in the model electrode, for different titania particle size as:

$$A = 1 - e^{-\alpha(\lambda)d} \quad (11)$$

where  $\alpha(\lambda)$  is the absorption coefficient and  $d$  the physical thickness of the electrode. Results are reported in Fig. 5.5.

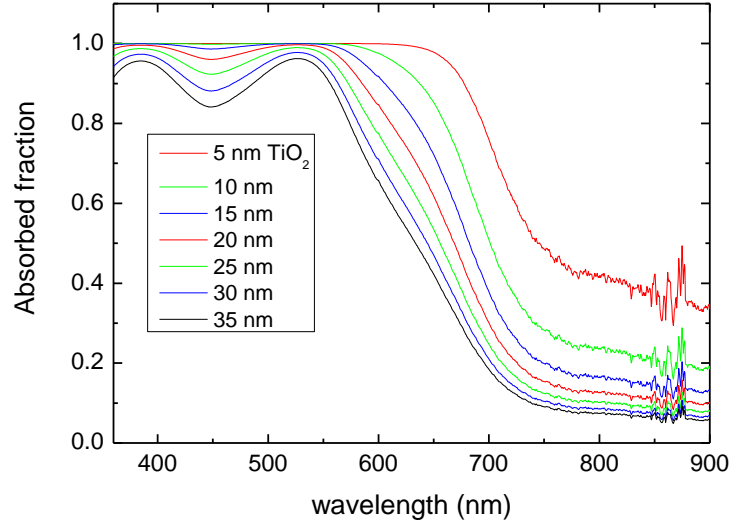


Fig. 5.5. Absorbed fraction of light calculated in model electrode made of different nanoparticles size.

The knowledge of the absorbed light in the device was used in order to calculate (integration range: from 360 to 900 nm) the short circuit current density that varies from 26 mA/cm<sup>2</sup> in case of the smallest nanoparticles (5nm) to 15 mA/cm<sup>2</sup> for larger ones. It is even too evident that, despite the high values in the region below 600nm, the absorption coefficient is low in the red-infrared spectrum, leading poorly efficient devices. Nevertheless, thick layers of nanostructured titania show highly diffusive behaviour, causing light trapping and hence a favourable optical absorption. An upper limit to the light absorption can be calculated by magnifying the optical path by the factor  $\gamma$ , and setting  $n=2.48$ , the refractive index of anatase phase titania:

$$\gamma=4n^2=24.6 \quad (12)$$

In presence of limit light trapping the absorbed fraction was calculated by introducing the enhancement factor:

$$A = 1 - e^{-\gamma\alpha(\lambda)d} \quad (13)$$

For the model electrode, the absorbed fraction is reported in Fig.5.6 for different nanoparticles size. In case of ultimate light trapping, it is noteworthy that light is completely absorbed in the visible spectral region for all the values of dye load considered, and at long wavelength spectral light trapping contributes to efficiently enhance absorption of light. For the model electrode the  $J_{sc}$  was calculated (integration range from 360 to 900 nm) in case of ultimate LT, the results being reported in Fig. 5.7.

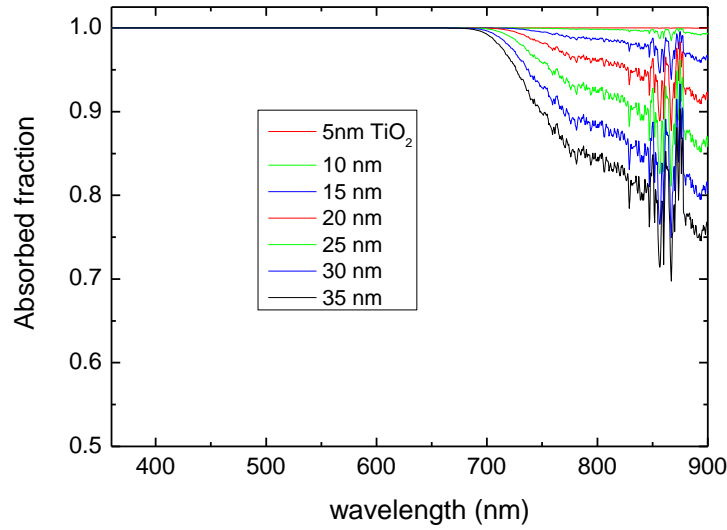


Fig. 5.6 Absorbed fraction of light calculated in model electrode made of different sized nanoparticles when the limit light trapping is considered.

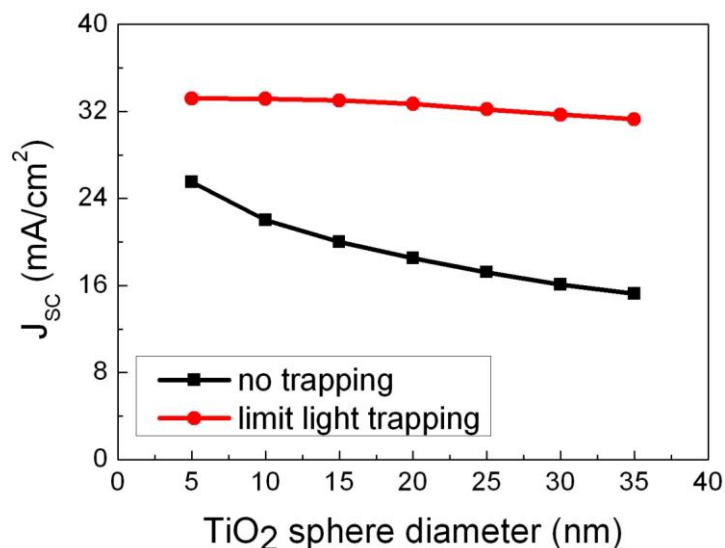


Fig. 5.7. Short circuit current density calculated for the model electrode, varying nanoparticles size; neglecting LT phenomena (black) or considering the limit LT (red).

The large difference of  $J_{sc}$  obtained by considering the light trapping underlines that i) considering light diffusion in porous titania electrodes is mandatory both in modelling device and interpreting experimental current to voltage measurements; ii) using proper light management strategies offers the opportunity of highly improving the conversion efficiency of the device.

### 5.2.2. Optical characterization

For the optical characterizations a PA with geometrical area of  $2.5 \text{ cm}^2$  was prepared as described in chapter 3.

A Perkin Elmer 330 UV-Vis-NIR spectrophotometer equipped with a 60 mm integrating sphere, coated with  $\text{BaSO}_4$ , was used to measure diffusive transmittance and reflectance in the spectral range 400 and 800 nm. The sphere was placed in such a way that the probe beam crosses the sphere without touching it when the entrance and exit ports of the sphere



were open. The total transmittance, i.e. the diffuse and the collinear ones, was measured by closing the integrating sphere with a white diffusive reflector, allowing the collimated part of the transmitted beam to be collected by the detector after multiple reflections in the sphere (Fig. 5.8a). The reflectance spectra were measured with the samples placed at the exit port of the sphere. The diffuse reflectance was determined with the sample oriented perpendicularly to the probe beam (Fig. 5.8b), the specular part of the reflected beam re-crossing the sphere without being detected. The specular reflectance was measured by using a specular reflecting accessory provided of Al mirrors (Fig. 5.9) and hence total reflectance was calculated as the sum of specular and diffuse ones. For transmittance, the 100% T baseline was recorded without the sample; whereas the reflectance spectra were measured

- i) relative to the reflectance of a clean  $\text{BaSO}_4$  pellet, which, according to the manufacturer, has a reflectance greater than 99% in the spectral range of interest, when integrating sphere was employed, or
- ii) relative to the reflectance of an Al mirror when the collinear reflective accessory was used.

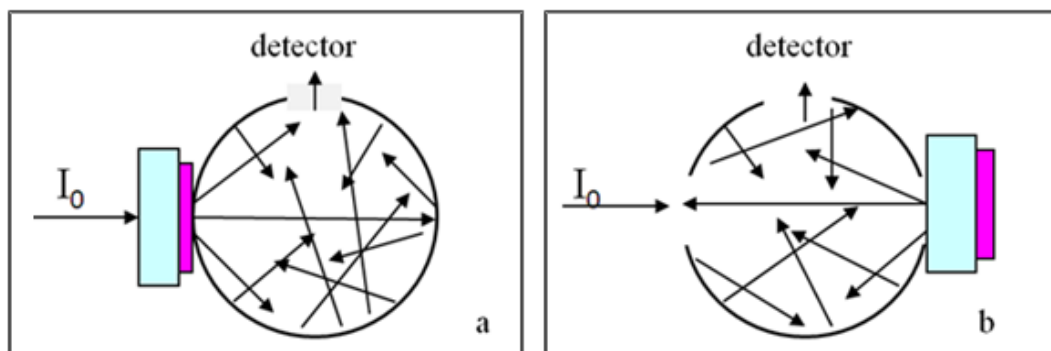


Fig.5.8. Schematics of total (a) transmittance and diffuse reflectance (b) spectra with integrating sphere (substrate in light blue, sensitized electrode in purple).

The reflectance spectra (with and without the integrating sphere) were collected with light incident on the glass side. The reflectance and transmittance spectra are reported in Fig. 5.10.

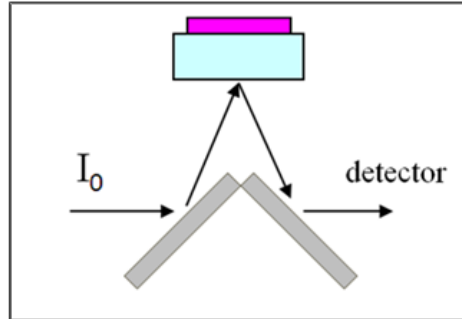


Fig.5.9. Schematic of specular reflectance measurements.

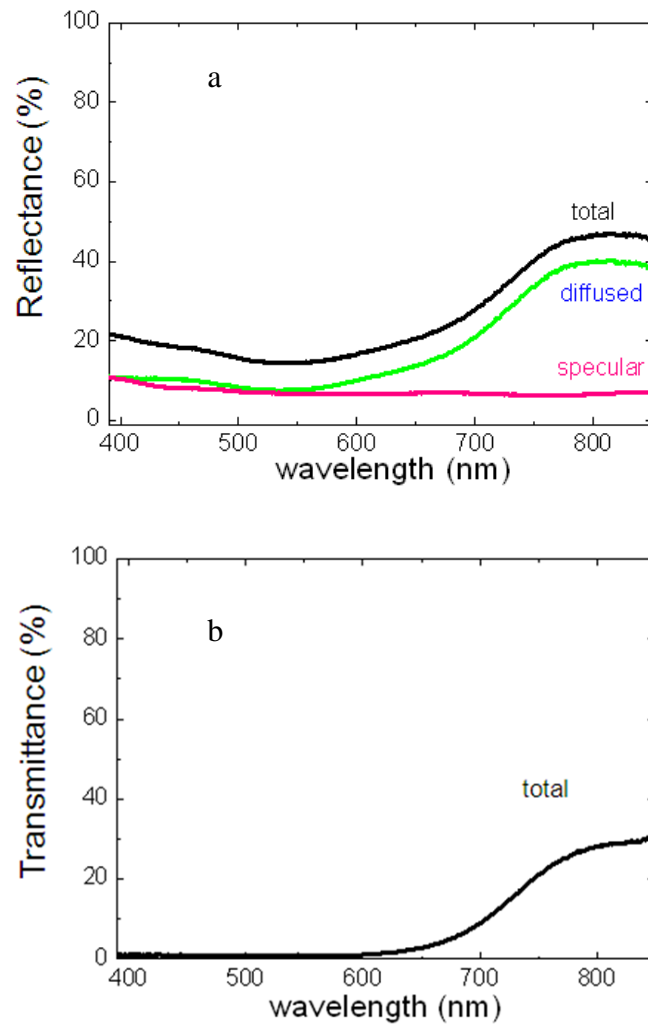


Fig. 5.10. Experimental reflectance (a) spectra and transmittance spectrum (b)

From reflectance and transmittance spectra the absorbed fraction, reported in Fig. 5.11, was calculated using as:

$$A(\lambda) = \frac{100-R(\lambda)-T(\lambda)}{100-R(\lambda)} \quad (14)$$

After spectrophotometric characterizations the dye load of the electrode was determined by desorbing the dye into 10 mM aqueous NaOH solution of known volume, measuring the peak absorbance (at 511 nm) of the solution by UV-vis spectrophotometry.

In order to take into account the absorption occurring in homogeneous non diffusive titania film on FTO, a “blank” sample, made of a transparent (non diffusive) titania layer on FTO, was similarly characterized and its absorbed fraction was subtracted to that of the studied PA.

The absorbed fraction is reported in Fig. 5.11 where a large error bar due to an indetermination of 4% in measured  $T(\lambda)$  is also shown as a grey shaded area. The reason of this uncertainty is that low values of transmittance are affected by systematic errors in our experiment, which employs a small integrating sphere with highly diffusive samples. In order to reduce this instrumental errors it can be observed that the absorbed fraction of light in the sensitized titania electrode cannot be lower than that in a solution of the same amount of dye. Therefore we can safely assume that the minimum value of the absorbed fraction in the electrode equals that of the dye, in the region of strong absorption.

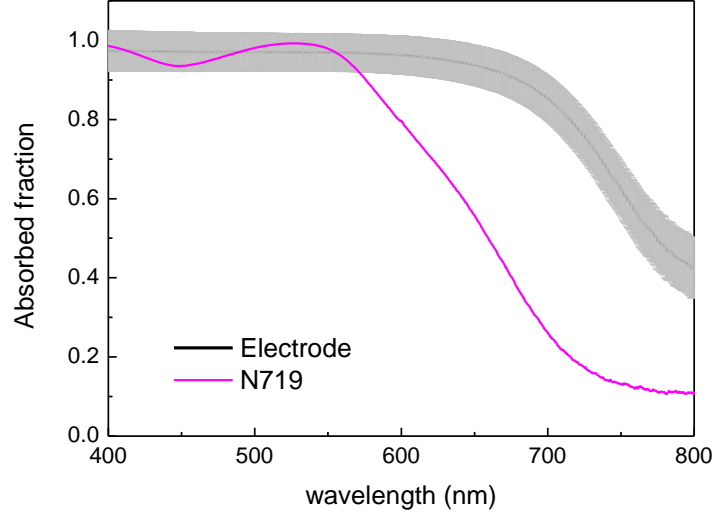


Fig. 5.11. Absorbed fraction of light in the sensitized electrode (black line) reported within its error (grey zone) and in the bare sensitizer (purple line).

### 5.2.3. Determination of the experimental enhancement factor

Naperian absorbance of dye is given by:

$$A_e^{N719} = -\ln[1 - A^{N719}(\lambda)] = \alpha(\lambda)d \quad (15)$$

where  $\alpha(\lambda)$  is the extinction coefficient of N719 and  $d$  the experimental electrode thickness (7  $\mu\text{m}$ , measured with mechanical profilometer). Similarly we define the Naperian absorbance of the electrode as

$$A_e^{electrode} = -\ln[1 - A^{electrode}(\lambda)] = \alpha(\lambda)\gamma(\lambda)d \quad (16)$$

The experimental spectrum of the enhancement of light absorption in diffusive titania is the given by the ratio between the two Naperian absorbances:

$$\gamma(\lambda) = \frac{A_e^{electrode}(\lambda)}{A_e^{N719}(\lambda)} \quad (17)$$

$\gamma(\lambda)$  is reported in Fig. 5.12, compared to the ultimate limit calculated accordingly to Yablonovitch theoretical prediction.

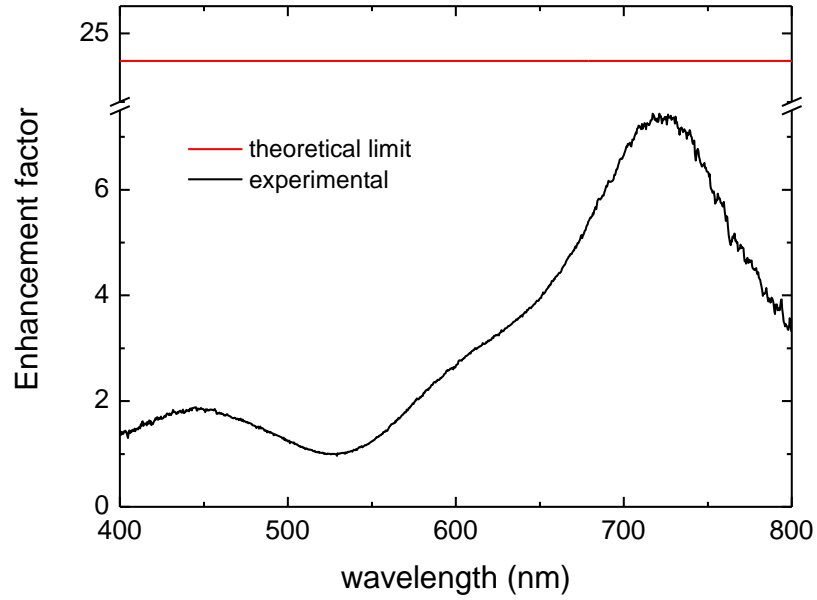


Fig.5.13. Enhancement factor spectral distribution.

### 5.3.DISCUSSION

The short circuit current of an ideal device ( $\eta_{inj}=\eta_{col}=1$ ) was calculated (integration range 400-800 nm) in three different cases:

- i) the absorbed fraction is relative to the bare dye load, neglecting any light trapping phenomena:  $J_{SC}=16 \text{ mA/cm}^2$  ;

- ii) the absorbed fraction is relative to an ideal condition of ultimate light trapping:  
 $J_{sc}=26 \text{ mA/cm}^2$  ;
- iii) the absorbed fraction is determined experimentally:  $J_{sc}=22.65 \text{ mA/cm}^2$  .

Our optical model neglects the physical configuration of a real cell, where

- i) the PA is immersed in the electrolyte, whose presence presumably causes the reduction of the absorption enhancement due to LT;
- ii) the cathode acts as back-reflector, and therefore enhances the optical absorption.

In spite of these approximations, the value of  $J_{sc}$  predicted by our optical considerations is close to the value measured in I-V characterizations of optimized cells (Chiba 2006).

On the other hand, the short circuit current density measured by I-V characterizations of our standard cells (see chapter 3) is  $J_{sc}=12.4 \text{ mA/cm}^2$ , well below the value predicted from pure optical considerations. This mismatch is mostly imputable to electron transport of the cell: the assumption that  $\eta_{inj}=\eta_{col}=1$  is verified only in optimized cells while our devices have poor conduction characteristics that severely affect the overall conversion efficiency. Studies on transport are beyond the argument of this thesis. However we can conclude that the assessment of the optical functionality of the active layer is meaningful and can be an useful tool for the characterization of novel materials for PA of DSSC.

## Chapter 6. Unconventional photoanode

*The potential for future increases in DSSC efficiency is strongly related to the development of new photoanodes producing higher photocurrent values. This deals both with the synthesis of new dyes absorbing over a wider spectral range, and with the development of high conductive nanostructured semiconductors. Highly ordered materials architectures, offering improved electron transport properties with respect to the conventional random network of titania nanoparticles, are under studies. In this framework, depicted in the first paragraph with a review of the state of the art, ordered vertically oriented TiO<sub>2</sub> nanotubes are one of the most promising materials. In this chapter optical modelling, synthesis and characterization of several samples are described and the first results obtained in application in complete devices are presented, with a discussion of the results and a sketch on the possible future work.*

### 6.1. STATE OF THE ART AND MOTIVATIONS

The conventional DSSC photoanode, constituted by small titania nanoparticles sintered together, has a large specific surface area that, allowing a huge dye uptake, ensures good light harvesting efficiency; on the other hand its constitution severely affects electron conduction properties. Electron transport, in fact, is reduced both for scattering at the interface between sintered particles, and for surface states that act as traps. Ordered, strongly interconnected nanoscale architecture offers a potential improvement of electron

transport. In particular, oriented titania nanotubes arrays (TNT) offer an attractive alternative to films of sintered titania nanoparticles because they can combine high surface area with good electron transport properties: i) micrometer length TNT can be grown by anodization of Ti foils (M. Paulose 2006), ii) well defined geometry can be selected by tuning anodization conditions, iii) electron diffusion length was estimated to be of the order of 100  $\mu\text{m}$  (J. R. Jennings 2008). Several papers report on the application of TNT grown on Ti foils in DSSC (K. Shankar 2007) (K.Shankar 2008); in these cases, since the support of the PA is not transparent, the cells must be illuminated from the cathode side (back illumination) with obvious losses due to light reflection from Pt and absorption in the electrolyte. Nevertheless the encouraging results drove the research in the direction of TNT-based transparent PA, obtained by the anodization of Ti films deposited on FTO (G.K. Mor 2006) (J.Y. Kim 2011) (O.K. Varghese 2009).

The main problems in the development of DSSC PA based on TNT, as reported in literature, are related to the technological difficulties in fabrication process: i) depositing Ti film tens of  $\mu\text{m}$  thick on FTO with such a good adhesion to withstand to the anodization process, ii) tuning the anodization process to obtain uniformly transparent TNT thick films without superficial debris (that close the pores); iii) achieving uniform anodization on the sample surface (avoiding faster anodization at the liquid/air interface).

Varghese (Varghese 2009) et al. reported the overcoming of these challenges thanks to the good quality of the metal film grown by sputtering and a proper choice of anodization conditions. They finally obtained TNT debris free films up to 30 $\mu\text{m}$  in length The anodization voltage reported was 60V, causing a TNT growth rate of 10 $\mu\text{m}/\text{h}$ .



## 6.2.OPTICAL MODELLING OF NANOTUBES PHOTOANODE

A simple optical model was developed for the description of a TNT based electrode, on the guideline of the one developed for conventional nanobeads one.

Geometrical parameters used to describe the nanotubes were: the internal radius ( $D/2$ ), the thickness of the wall ( $w$ ), the spacing between adjacent tubes ( $I$ ), the length of tubes ( $L$ ). The surface area of a single tube was then calculated as the sum of that relative to the external and internal tubes, the circle at the bottom of the tube and the upper ring. In order to calculate the number of tubes in the electrode with a surface of  $1\text{cm}^2$  (refers to fig 6.1), it was necessary to set the value of the packing density. SEM images observation suggested that TNT are arranged in a honeycomb lattice; hence the question of packing was reduced to a 2-dimensional problem of circles densely packed in a given boundary. An equivalent circle, with radius

$$R=D/2+w+I/2$$

was considered, and the packing density was fixed at 0.9 (<http://mathworld.wolfram.com/CirclePacking.html>). As for the nanospheres-based model electrode, the specific surface and the dye uptake were calculated as functions of the morphological parameters. Some results are summarized in Fig. 6.2 and 6.3.

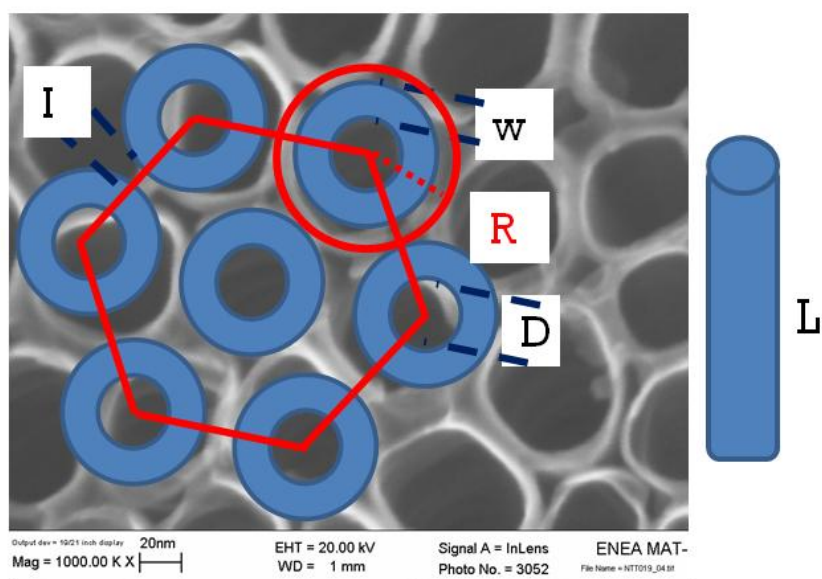


Fig. 6.1. SEM image of a TNT array. The sketch superimposed outlines the morphological parameters used in modelling.

The results show that at a fixed length of tubes (thickness of titania electrode), the dye uptake is considerably lower than that of a spherical nanoparticles-based electrode. The typical TNT obtained have internal diameter 90-120 nm, external diameter 130-150 nm and spacing between adjacent tubes  $\approx 0$ . The optical model allows to formulate a clear requirement for the TNT morphology: for the typical tubes reported in literature, a length of 50  $\mu\text{m}$  is necessary to equal the dye uptake of a conventional PA  $\mu\text{m}$  10 thick. Similar thickness can result in high efficient solar cells only if the electron diffusion length in TNT is much higher than in conventional PA, as predicted by Jennings et al., ensuring high collection efficiency.

On the other hand, the model suggests that the most promising morphology is that made of dense “nanowires”: closed long tubes with no spacing in between, hence driving different synthesis routes.

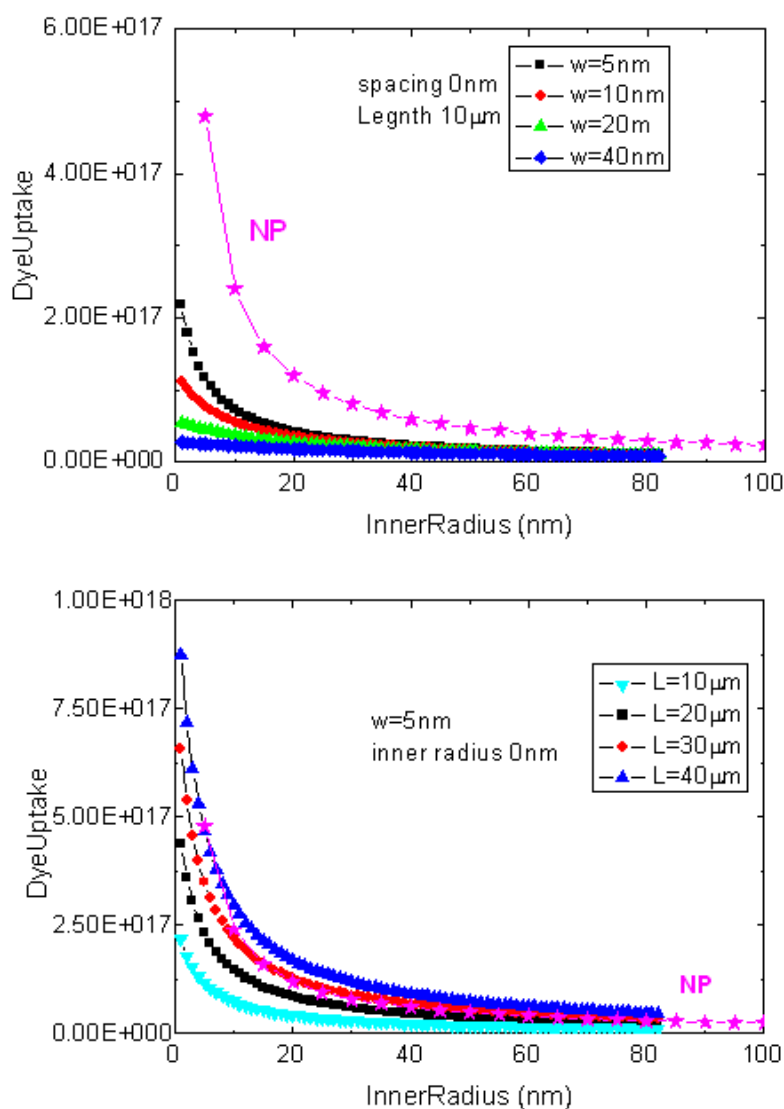


Fig 6.2. Dye uptake of TNT-based model electrode with different morphologies.

Purple stars: dye uptake of a nanoparticles based titania electrode.

In a preliminary study up to  $3\text{ }\mu\text{m}$  thick were grown on glass, resulting in highly transparent non diffusive samples. Then, even if proper optical characterizations have not been performed yet, we can reasonably assume a light absorption enhancement due to LT could be neglected and strategies for light management should be studied afterwards.

### 6.3.TITANIA NANOTUBES SYNTHESIS AND CHARACTERIZATION

In the framework of an existing research activity in ENEA laboratories on synthesis of titania nanostructures, several samples of TNT on FTO were synthesized, characterized and finally applied as PA in DSSC. Since the anodization process was optimized on Ti foils, the route for synthesis of TNT on FTO was at a preliminary step. The first results are reported below.

Titanium dioxide nanotubes form from metallic Ti in electrolytic solutions of  $F^-$  ions and water in a current driven electrochemical anodization process. A state of the art procedure was followed for production of TNT from Ti films on FTO (O.K. Varghese 2009). Ti films were sputtered without any external heating of the sample. Ti compact reflective samples were obtained of controlled thickness (see Tab. 6-1). Two electrode vertical cell was realized on purpose for the anodization of Ti films on FTO. The sample is the bottom shutter, fixed to the cell with mechanical clumps, an o-ring ensuring the electrolyte tight. This geometry avoids the existence of the air/electrolyte on the anodizing surface, overcoming one of the major problems in synthesis route. The electrical contact was made on the surface of the sample externally to the electrolyte. The counter-electrode was made of a disk of graphite facing at 5 mm from the anodizing surface. The electrolyte solution was made of 0.3%wt  $NH_4F$  and 2% water in ethylene glycol. As a starting point, 300nm thick and 1  $\mu m$  thick films were deposited via sputtering. While it is possible to scan a wide range of potentials for anodizing Ti foils, only a narrow window of potentials could be applied to Ti films on FTO, because in most of the conditions a severe damage of interface caused detachment of TNT from the substrate. Moreover, we found that the higher was the Ti thickness the more breakable resulted the interface. Even though technological problems related to the synthesis of long TNT remain unsolved, some samples, listed in Tab. 6-1 were prepared, characterized and tested in DSSC.

Tab. 6-1 summarises samples presented in this work: Ti films thickness, anodization voltage, anodization time and TNT length; all the samples having surface area of 0.28 cm<sup>2</sup>. The anodization processes were interrupted when the samples appeared transparent. SEM images of a typical sample are reported in Fig. 6.3. The as grown TNT film was covered by TiO<sub>2</sub> debris (Fig.6.3a) due to the initial anodization stage. The presence of debris is detrimental in applications since it causes the occlusion of the pores (neither the dye in the sensitizing process nor electrolyte in operating device access to a large fraction of surface). A brief sonication process in water enabled to remove all the debris and clear the internal tubes surface (Fig.6.3b) without producing any damage in the TNT film. In scratched samples the long tubular structure is evident (Fig. 6.3c). As grown TNT are amorphous, but crystalline anatase phase is required for applications in DSSC, so the samples were annealed at 450°C for 30'. SEM imaging confirmed that the tubular structure was not altered during the thermal treatment, while Raman spectra (experimental details described in chapter 4), reported in Fig 6.4 confirm the anatase crystalline phase (U. Balachandran 1982) obtained by annealing the as prepared amorphous sample. The morphological parameters of TNT samples were measured by SEM imaging; no appreciable differences are evident for samples anodized at different voltages: D=60 nm; w=24 nm; I≈0.

Sample	Ti film thickness (μm)	Anodization voltage (V)	Anodization time (min)	TNT length (μm)
TNT88	0.3	40	15	1
TNT90	0.3	50	6	1
TNT91	0.3	60	3	1
TNT99	1	60	5	3

Tab. 6-1. Electrolyte composition, anodization voltage, growth rate.

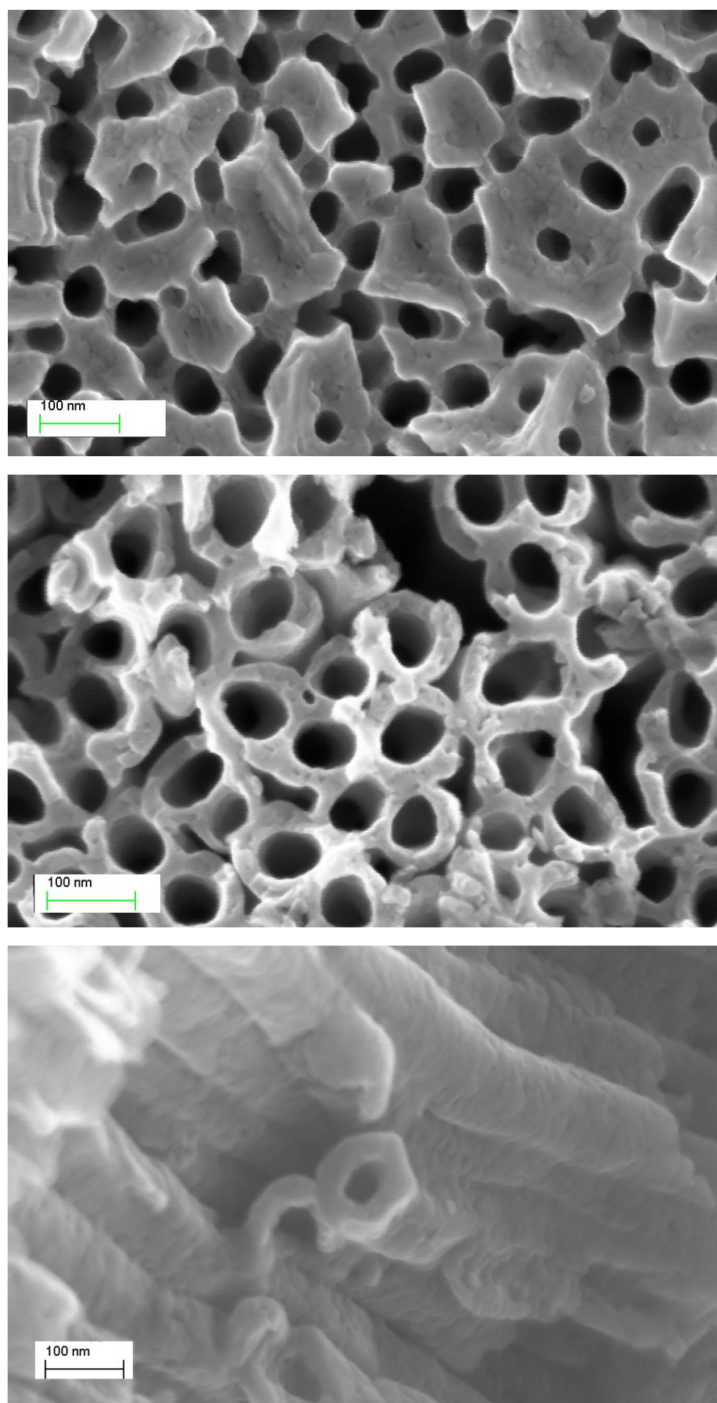


Fig. 6.3. SEM images of TNT films, before (a) and after (b,c) sonication.

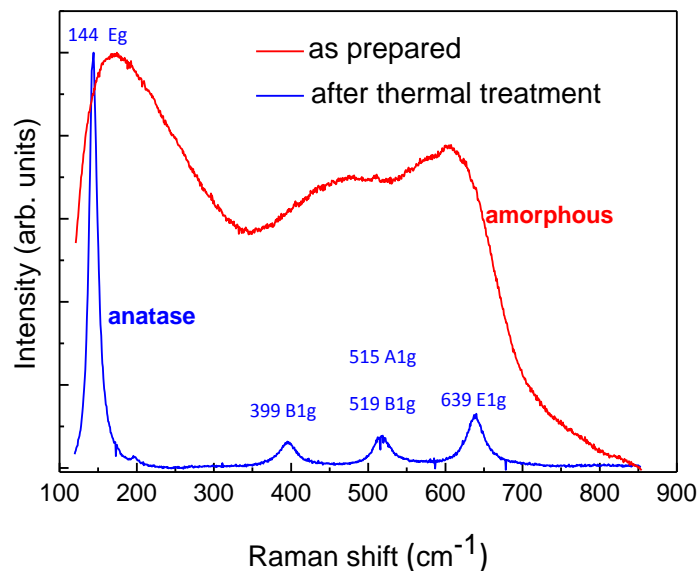


Fig 6.4. Raman spectra of a TNT sample as prepared and after annealing.

The small sample surface did not allow a measurement of their transmittance and reflectance, but they were coarsely transparent and we assume that LT could be negligible. The TNT samples grown on FTO after non destructive characterizations were dipped in dye solution (as described in chapter 3 for the conventional titania electrodes) to be successively used in DSSC.

## 6.4. DEVICE CHARACTERIZATIONS

The procedure to assembly the cells was described in chapter 3. The cells were characterized under standard AM1.5 solar illumination and the J-V curves are reported in Fig. 6.5.

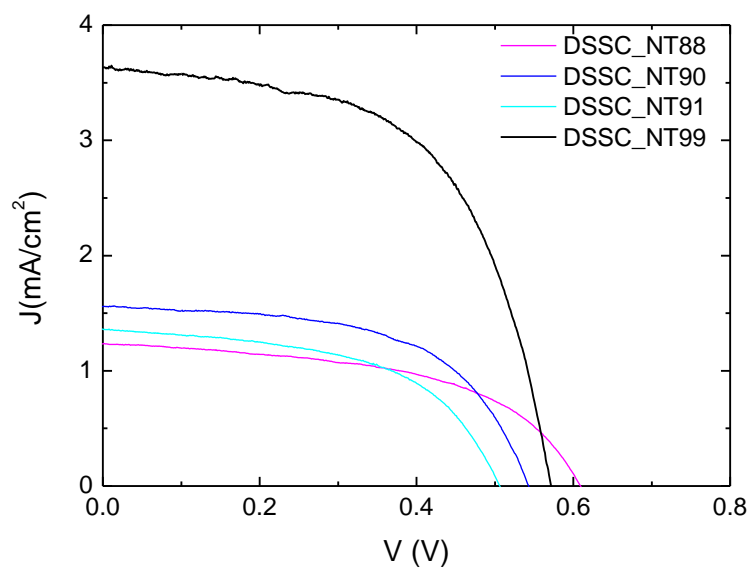


Fig. 6.5. Current density to voltage characteristics under illumination of DSSC with TNT-based photoanodes.

The photovoltaic parameters obtained from J-V curves are listed in Tab. 6-2.

Sample	$V_{oc}$ (V)	$J_{sc}$ (mA/cm <sup>2</sup> )	FF	$\eta$ (%)
DSSC_NT88	0.609	1.3	0.5	0.4
DSSC_NT90	0.544	1.6	0.6	0.5
DSSC_NT91	0.508	1.4	0.5	0.4
DSSC_NT99	0.573	3.7	0.6	1.2

Tab. 6-2. Relevant photovoltaic parameters of the DSSC tested.



## 6.5. DISCUSSION

The J-V curves reported in Fig. 6.5 show short circuit current density values in good agreement with literature results referred to comparable TNT lengths: the longer were the TNT the higher were the collected photocurrents. The values of  $J_{sc}$  are in agreement with the optical functionality of TNT-based PA, mainly due to the bare dye load, absorption enhancement due to LT being negligible.

The open circuit voltage values ( $\sim 500$  mV) of DSSC-TNT90, DSSC-TNT91, DSSC-TNT99 are lower than that relative to DSSC-TNT88 ( $V_{OC}=609$  mV). It is noteworthy that TNT88 was anodized at the lowest potential (40 V) for a longer time (15 minutes). This result seems to indicate that a TNT-based PA produced with low-voltage, slow anodization process has better performances when applied in DSSC. These preliminary results pointed out that an overall improvement of the functionality of novel PA can be achieved by technological optimization of the synthesis processes: from Ti film deposition to anodization conditions. Ti films sputtering conditions should be finely tuned to obtain i) good quality interface in terms of strong adhesion to substrate also when undergone to the anodization process; ii) densely packed homogeneous thick films.

As early discussed, many factors affect the anodization process and also minor variations can lead to effective improvements: our experiments demonstrated that a careful choice of the electrolytic cell design avoids the detrimental effects of air/electrolyte interface and that post-grown sonication cleaning allows a safe debris removal. Further works are still necessary, and it looks worthwhile, to tune other parameters such as voltage and processing time.

## LIST ACHRONISMS

BIPV	Buiding Integrated Photovoltaic
CE	Counter Electrode
CIGS	Copper Indium Gallium Selenide
CIS	Copper Indium Selenide
CNT	Carbon Nanotubes
CNW	Carbon Nanowalls
DSSC	Dye Sensitized Solar Cells
FF	Fill Factor
FTO	Fluorine-Doped Tin Oxide
HOMO	Highest Occupied Molecular Orbital
IC	Integrated Circuit
IPCE	Incident Photon-To-Electron Conversion Efficiency
ITO	Indium Tin Oxide
LT	Light Trapping
LUMO	Lowest Unoccupied Molecular Orbital
MWCNT	Multi Wall Carbon Nanotubes
NHE	Normal Hydrogen Electrode
OPV	Organic Photovoltaic
PA	Photoanode
PV	Photovoltaic
SQ	Shockley Queysson
SR	Spectral Response
SWCNT	Single Wall Carbon Nanotubes
TCO	Transparent Conductive Oxide
TNT	Titania Nanotubes

## REFERENCES

- Agrios A.G., I. Cesar, P. Comte, M. Nazeeruddin, M. Grätzel, . «Nanostructured Composite Films for Dye-Sensitized Solar Cells by Electrostatic Layer-by-Layer Deposition.» *Chem. Mater.*, 2006: 5395–5397.
- Andersson, B. A. *Prog. Photovoltaics* 8 (2000): 61.
- Arnold M. S., J. D. Zimmerman, C. K. Renshaw, X. Xu, R. R. Lunt, C. M. Austin, S. R. Forrest. «Broad Spectral Response Using Carbon Nanotube/Organic Semiconductor/C60 Photodetector.» *Nano Lett.* 9 (2009): 3354–3358.
- Bach U., D. Lupo, P. Comte, J. E. Moser, F. Weissörtel, J. Salbeck, H. Spreitzer, M. Grätzel 583. *Nature*, 1998: 395.
- Balachandran U., N.G. Eror. «Raman spectra of titanium dioxide.» *J. Solid State Chem.*, 1982: 276–282.
- Bariscia J.N., G.G Wallace, D.R MacFarlane, R.H Baughman. «Investigation of ionic liquids as electrolytes for carbon nanotube electrodes.» *Electrochem. Commun.* 6, n. 22 (2004).
- Baughman R. H., A.A. Zakhidov, W.A. de Heer. «Carbon Nanotubes: the Route toward Applications.» *Science* 297 (2002): 787-792.
- Biswas R., C. Xu. «Nano-crystalline silicon solar cell architecture with absorption at the classical  $4n^2$  limit.» *Optics Express* 19, n. S4 (2011): A664.
- Bozzola A, M. Liscidini, L. C. Andreani. «Light Trapping in Thin Film Silicon Solar Cells with Mono and Bidimensional Photonic Patterns.» Austin, Texas: Optical Nanostructures and Advanced Materials for Photovoltaics, 2011.
- Brabec C. J., S. Gowrisanker, J. J. M. Halls, D. Laird, S. J. Jia, S. P. Williams. *Adv. Mater* 22 (2010): 3839.

Britt J., C. Ferekides. Appl. Phys. Lett. 62 (1993): 2851.

Cahen D., G.Hodes, M. Graetzel, J.F. Guillemoles, I. Riess. J. Phys.Chem. B 104.

Callahan D.M., J.N. Munday, and H. A. Atwater. «Solar Cell Light Trapping beyond the Ray Optic Limit.» NanoLett. 12 (2012): 214-218.

Cancado L.G., K. Takai, T. Enoki, M. Endo, Y.A. Kim, H. Mizusaki,N.L. Speziali, A. Jorio, M.A. Pimenta. «Measuring the degree of stacking order in graphite by Raman Spectroscopy.» Carbon 46 (2008): 272-275.

Cappelli E., S. Orlando, G. Mattei, C. Scilletta, F. Corticelli, P. Ascarelli,. Applied Physics A 79 (2004): 2063-2068.

Carlson D. E., C. R. Wronski. Appl. Phys. Lett. 28 (1976): 671.

Catchpole R., A. Polman. «Design principles for particle plasmon enhanced solar cells.» Appl. Phys. Lett. 93 (2008): 191113.

Chen L. J., Q. L. Song, Z. H. Xiong, J. H. Huang, F. He. «Environment-Friendly Energy from All-Carbon Solar Cells Based on Fullerene-C60.» Sol. Energy Mater. Sol. Cells 95 (2011): 1138-1140.

Chiba Y., A. Islam, R. Komiya, N. Koide, L. Han. «C efficiency of 10.8% by a dye-sensitized solar cell using a TiO<sub>2</sub> electrode with high haze.» App. Phys. Lett., 2006: 223505–1–223505–3.

Choi H., H. Kim, H. S. Hwang, W. Choi, M. Jeon. «Dye-Sensitized Solar Cells Using Graphene-Based Carbon Nano Composite as Counter Electrode.» Sol. Energy Mater. Sol.Cells vol. 95, n. 1 (2011): 323-325.

Ciszek T. F., J. L. Hurd, and M. Schietzelt. J. Electrochem. Soc. 129 (1982): 2838.

Ciszek, T. F. Mater. Res. Bull. 7 (1972): 731.

Compaan, A. Gupta, S. Lee, S. Wang, J. Drayton. Sol. Energy 77 (2004): 815.

Contreras M. A., B. Egaas, K. Ramanathan, J. Hiltner, F. Hasoon, R. Noufi. Prog. Photovoltaics 7 (1999): 311.

Cusano, D. A. Solid-State Electron. 6 (1963): 217.

D. Li, H. Li, Y. Luo, K. Li, Q. Meng, M. Armand, L. Chen. Advanced Functional Materials, 2010: 3358.

del Coso G., I. Tobias, C. Canizo, A. Luque, J. Cryst. Growth 299 (2007): 165.

Denaro T., V. Baglio, M. Girolamo, V. Antonucci, e F. Matteucci, R. Ornelas A. S. Arico. «Investigation of Low Cost Carbonaceous Materials for Application as Counter Electrode in Dye-Sensitized Solar Cells.» J. Appl. Electrochem. 39 (2009): 2173–2179.

Desilvestro, R. Harikisun and H. Sol. Energy, 2011 : in press.

Dinadayalan T., J. Leszczynski. «Remarkable Diversity of.» Struct. Chem. 21 (2010): 1155-1169.

Dros F. s, J. Robbelein, B. Vandeveld, E. Van Kerschaver, I. Gordon, G. Beaucarne, J. Poortmans. Appl. Phys. A: Mater. Sci. Process 89 (2007): 149.

Dros F. s, J. Robbelein, B. Vandeveld, E. Van Kerschaver, I. Gordon, G. Beaucarne, J. Poortmans. Appl. Phys. A: Mater. Sci. Process 89 (2007): 149.

F. -T. Kong, S. -Y. Dai, K. -J. Wang. Advances in Optoelectronics (1), 2007.

Fan B., X. Mei, K. Sun, J. Ouyang. «Conducting polymer/carbon nanotube composite as counter electrode of dye-sensitized solar cells.» Appl. Phys. Lett. 93 (2008): 143103.

Fang B., S.Q. Fan, J. H. Kim, M.S. Kim, M. Kim, N. K. Chaudhari, J. Ko, J.S. Yu. «Incorporating Hierarchical Nanostructured Carbon Counter Electrode into Metal-Free Organic Dye-Sensitized Solar Cell.» Langmuir 26 (2010).

Ferber J., J. Luther. «Computer simulations of light scattering and absorption in dye-sensitized solar cells.» Sol. Energy Mater. and So. Cells, 1998: 265D275.

Ferrari A.C., J. Robertson. «Interpretation of Raman Spectra of Disordered and Amorphous Carbon.» Phys. Rev. B 61 (2000): 14095-14107.

Gabor A. M., J. R. Tuttle, D. S. Albin, M. A. Contreras, R. Noufi, A. M. Herman. Appl. Phys. Lett. 65 (1994): 198.

Gagliardi S., L. Giorgi, R. Giorgi, N. Lisi, Th. Dikonimos Makris, E. Salernitano, A. Rufoloni. «Impedance analysis of nanocarbon DSSC electrodes.» Superlattices and Microstructures 46 (2009): 205-208.

Gálvez F., E. Kemppainen, H. Miguez, J. Halme. «Effect of Diffuse Light Scattering Designs on the Efficiency of Dye Solar Cells: An Integral Optical and Electrical Description.» J. Phys. Chem. C, 2006: 11426-11433.

Gao F., Y.Wang, D.Shi, J.Zhang, M.Wang, X. Jing, R.Humphrey-Baker, P. Wang, S.M. Zakeerudin, M. Graetzel. «Enhance the Optical Absorptivity of Nanocrystalline TiO<sub>2</sub> with High Molar Extinction Coefficient Ruthenium Sensitizers for High Performance Dye-Sensitized Solar Cells.» *J. Am. Chem. Soc.*, 2008: 10720-10728.

Giorgi L., Th. Dikonimos Makris, R. Giorgi, N. Lisi, E. Salernitano. «Electrochemical properties of carbon nanowalls synthesized by HF-CVD.» *Sensors and Actuators B* 126 (2007): 144–152.

Goetzberger, C. Hebling, H. W. Schock. *Mater. Sci. Eng. R.* 40 (2003): 1.

Graff G. L., R. E. Williford P. E. Burrows. *J. Appl. Phys.* 96 (2004): 1840.

Grätzel M., 414, 338. *Nature*, 2001.

Grätzel, M. Hybrid and Organic Photovoltaics Conference. Valencia (Spain), 2011.

Green M. A., K. Emery, Y. Hishikawa, W. Warta. *Prog. Photovoltaics* 18 (2010): 346.

Green, M. «Lambertian Light Trapping in Textured Solar Cells and Light-Emitting Diodes: Analytical Solutions.» *Prog. Photovolt. Res. Appl.* 10 (2002): 235-241.

Green, M. A. «Third generation photovoltaics: Ultra-high conversion efficiency at low cost.» *Prog. Photovoltaics* 9 (2001): 123.

Green, M. A. *Prog. Photovoltaics* 17 (2009): 347.

Green, M. A. *Prog. Photovoltaics* 7 (1999): 327.

Griffith M.J., M. James, J. Triani, P. Wagner, G.G. Wallace, D.L. Officer,. «Determining the Orientation and Molecular Packing of Organic Dyes on a TiO<sub>2</sub> Surface Using X-ray Reflectometry.» *Langmuir* 27 , n. 21 (2011): 12944-12950.

Hagfeldt, G. Boschloo, L. Sun, L. Kloo, and H. Pettersson. *Chem. Rev.* 110 (2010): 6595.

Halme J., P. Vahermaa, K. Miettunen, P. Lund. *Advanced Energy Materials* E210 (2010): 22.

Heliatek. 1 December 2010. <http://www.heliatek.com/news-19>.

Hibberd C. J., E. Chassaing, W. Liu, D. B. Mitzi, D. Lincot, A. N. Tiwari. *Prog. Photovoltaics* 18 (2010): 434.

Hiramatsu M., M. Hori. *Carbon Nanowalls, Synthesis and Emerging Applications*. Wien: Springer-Verlag, 2010.

- Hirsch, A. «The Era of Carbon Allotropes.» *Nat. Mater.* 9 (2001): 868-871.
- Hong W., Y. Xu, G. Lu, C. Li, G. Shi. «Transparent graphene/PEDOT–PSS composite films as counter electrodes of dye-sensitized solar cells.» *Electrochemistry Communications* 10 (2008): 1555–1558.
- Hovel Semiconductors and semimetals, vol.11. New York: Academic Press, 1975.
- <http://www.solaronix.com/products/screenprintingtitania/tinanoxidedsp/>.
- Hu L., W. Yuan, P. Brochu, G. Gruner, Q. Pei. «Highly stretchable, conductive, and transparent nanotube thin films.» *Appl. Phys. Lett.* 94 (2009): 161108.
- Huang F., D. Chen, X. L. Zhang, R. A. Caruso, Y. B. Cheng. «Dual-Function Scattering Layer of Submicrometer-Sized Mesoporous TiO<sub>2</sub> Beads for High-Efficiency Dye-Sensitized Solar Cells.» *Adv. Funct. Mater.*, 2010: 1301–1305.
- Imoto K., K. Takahashi, T. Yamaguchi, T. Komura, J. Nakamura, K. Murata. «High-performance carbon counter electrode for dye-sensitized solar cells.» *Sol. Energy Mater. Sol. Cells* 79 (2003): 459-469.
- Ito S., S. M. Zakeeruddin, R. Humphry-Baker, P. Liska, R. Charvet, P. Comte, M. K. Nazeeruddin, P. Péchy, M. Takata, H. Miura, S. Uchida, and M. Grätzel. «High-Efficiency Organic-Dye-Sensitized Solar Cells Controlled by Nanocrystalline-TiO<sub>2</sub> Electrode Thickness.» *Adv. Mater.* 18 (2006): 1202–1205.
- Itoh T., S. Shimabukuro, S. Kawamura, S. Nonomura. «Preparation and electron field emission of carbon nanowall by Cat-CVD.» *Thin Solid Films* 2006 501 (2006): 314–317.
- Jennings J. R., A. Ghicov, L. M. Peter, P. Schmuki, A.B. Walker. «dye-sensitized solar cells based on oriented TiO<sub>2</sub> nanotube array: transport, trapping and transfer of electrons.» *J. Am. Chem. Soc.*, 2008: 13364–13372.
- Jeong H.J., H. D. Jeong, H. Y. Kim, J. S. Kim, S. Y. Jeong. «All-Carbon Nanotube-Based Flexible Field-Emission Devices: From Cathode to Anode.» *Adv. Funct. Mater.* 21 (2011): 1526-1532.
- Jørgensen M., K. Norrman, F. C. Krebs. *Sol. Energy Mater. Sol. Cells* 92 (2008): 686.
- Kalyanasundaram K., M. Grätzel. *Coordination Chemistry Reviews* 77 (1998): 347.
- Kay A., M. Graetzel. «Low cost photovoltaic modules based on dye sensitized

nanocrystalline titanium dioxide and carbon powder.» *Sol. Energy Mater. Sol. Cells* 44 (1996): 99-117.

Kay, M. Grätzel. *Solar Energy Materials & Solar Cells* 44 (1996): 99.

Kazmerski L. L., F. R. White, G. K. Morgan. *Appl. Phys. Lett.* 29 (1976): 268.

Kelzemberg M.D., S.W. Boettcher, J.A. Petykievich, D.B. Turner-Evans, M.C. Putnam, E.L. Warren, J.M. Spurgeon, R.M Briggs, N.S. Lewis, H.A. Atwater. «Enhanced absorption and carrier collection in Si wire Arrays for Photovoltaic applications.» *Nature Materials* 9 (2010): 239-244.

Kerr M. J., J. Schmidt, A. Cuevas. *Proceedings of the 29th IEEE Photovoltaics Specialists Conference*. New Orleans, LA, 2002. 438.

Kim , V. Yelundur, K. Nakayashiki, B. Rounsaville, V. Meemongkolkiat, A. M. Gabor, A. Rohatgi. *Sol. Energy Mater. Sol. Cells* 90 (2006): 1227.

Kim J.Y., J.H. Noh, K. Zhu, A.F.Halverson, N.R. Neale, S. Park, K.S.Hong, A.J. Frank. «General strategy for fabricating transparent TiO<sub>2</sub> nanotube arrays for dye-sensitized photoelectrodes: illumination geometry and transport properties.» *ACS Nano*, 2011: 2647-2656.

Kishi K., H. Katsuhiko. *ThreeBond Technical News*, 2005.

Konarka. 1 December 2010. <http://www.konarka.com/index.php/newsroom/press-releaselist/>.

Kumara G. R. A., S. Kaneko, M. Okuya, and K. Tennakone, 10493. *Langmuir* 18 (2002): 10493.

Landau D., E.M. Lifshitz. *Electrodynamics of Continuous Media*. New York: Pergamon, 1969.

Lee K.M., V. Suryanarayanan, K. C. Ho. «The influence of surface morphology of TiO<sub>2</sub> coating on the performance of dye-sensitized solar cells.» *Sol. Energy Mater. Sol.Cells*, 2006: 2398–2404.

Lee W.J., E. Ramasamy, D.Y.Lee, J.S. Song. «Performance variation of carbon counter electrode based dye-sensitized solar cell.» *Sol. Energy Mater. Sol. Cells* 92 (2008): 814-818.



Lewis, N.S. *Mat. Res. Bull.*, 2007: 76.

Li K., Y. Luo , Z. Yu, M. Deng ,D. Li, Q. Meng. «Low temperature fabrication of efficient porous carbon counter electrode for dye-sensitized solar cells.» *Electrochem. Commun.* 11 (2009): 1346.

Lincot et al., D. *Sol. Energy* 77 (2004): 725.

Lisi N., R. Giorgi , M. Re, T. Dikonimos, L. Giorgi, E. Salernitano, S. Gagliardi,F. Tatti. «Carbon nanowall growth on carbon paper by hot filament chemical vapour deposition and its microstructure.» *Carbon* 49 (2011): 2134-2140.

Luque A., S. Hegedus. *Handbook of Photovoltaic Science and Engineering*, chap. 3,. West Sussex (England): John Wiley & Sons Ltd, 2003.

Luque, S. Hegedus. Cap. 15 in *Handbook of Photovoltaic Science and Engineering*, di S. Hegedus West Sussex : John Wiley & Sons Ltd,, 2003.

M. Taguchi, H. Sakata, Y. Yoshimine, E. Maruyama, A. Terakawa, M. Tanaka, S. Kiyama. *Proceedings of the of the 31st IEEE Photovoltaic Specialists Conference*. Orlando, FL, 2005. 866.

Marecek, S. Veprek and V. *Solid-State Electron* 11 (1968): 683.

McAllister M.J., J.L. Li, D. H. Adamson, H C. Schniepp, A. A. Abdala, J. Liu, M. Herrera-Alonso, , D. L. Miliu, R. Car, R. K. Prud'homme, I. A. Aksay. «Single Sheet Functionalized Graphene by Oxidation and Thermal Expansion of Graphite.» *Chem. Mater.* 19 (2007): 4396–4404.

Mehta, S. 2009 *Global PV Cell andModule Production Analysis*. San Francisco (CA): GTM Research, 2009.

Mei X., J. Ouyang. «Gels of carbon nanotubes and a nonionic surfactant prepared by mechanical grinding.» *Carbon* 48 (2010): 293.

Mei X., S. J. Cho, B. Fan, J. Ouyang. «High-performance dye-sensitized solar cells with gel-coated binder-free carbon nanotube films as counter electrode.» *Nanotechnology* 21 (2010): 395202.

Mor G.K., K. Shankar, M. Paulose, O.K. Varghese, C.A. Grimes. «Use of highly-ordered TiO<sub>2</sub> nanotube arrays in dye-sensitized solar cells.» *NanoLetters*, 2006: 215-218.

Murakami T. N., M. Graetzel. «Counter Electrodes for DSC: Application of Functional Materials as Catalysts.» *Inorg. Chim. Acta* 361 (2008): 572–580.

Murakami T. N., S. Ito, Q. Wang, M.K. Nazeeruddin, T. Bessho, I. Cesar, Paul Liska, Robin Humphry-Baker, P. Comte, P. Pechy and M. Graetzel. «Highly Efficient Dye-Sensitized Solar Cells Based on Carbon Black Counter Electrodes.» *J. Electrochem. Soc.* 153, n. 12 (2006): A2255-A2261.

Murayama H., S. Tomonoh, J. M. Alford, M.E. Karpuk. «Fullerene Production in Tons and More: From Science to.» *Fullerenes, Nanotubes, Carbon Nanostruct.* 12 (2005): 1-9.

N. Kato, K. Higuchi, H. Tanaka, J. Nakajima, T. Sano, T. Toyoda. *Sol. Energy Mater. Sol. Cells* 95 (2011): 301.

Nakayama K., K. Tanabe, H. A. Atwater. «Plasmonic nanoparticle enhanced light absorption in GaAs solar cells.» *Appl. Phys. Lett.* 93 (2008): 121904.

Nam J. G., Y. J. Park, B. S. Kim, J. S. Lee. «Enhancement of the Efficiency of Dye-Sensitized Solar Cell by Utilizing Carbon Nanotube Counter Electrode.» *Scr. Mater.* 62 (2010): 148–150.

Nazeeruddin M. K., A. Kay, I. Rodicio, R. Humphry-Baker, E. Mueller, P. Liska, N. Vlachopoulos, M. Graetzel. *J. Am. Chem. Soc.* 115 (1993): 6382.

Nelson, J. *the Physics of Solar Cells*. Covent Garden: Imperial College Press, 2003.

Noorden. «Chemistry: The Trials of New Carbon.» *Nature* 469 (2011): 14-16.

O'Regan B., M. Gratzel. *Nature* 353 (1991): 737 .

Pacios M., M. del Valle , J. Bartroli and M.J. Esplandiu. «Electrochemical behavior of rigid carbon nanotube composite electrodes.» *J. Electroanal. Chem.* 619-620 (2008): 117-124.

Paulose M., K. Shankar, S. Yoriya, H. E. Prakash, O. K. Varghese, G. K. Mor, T. A. Latempa, A. Fitzgerald, and C.A. Grimes. «Anodic Growth of Highly Ordered TiO<sub>2</sub> Nanotube Arrays to 134  $\mu$ m in Length.» *J. Phys. Chem. B*, 2006: 16179–16184.

Pizzini, S. *Sol. Energy Mater. Sol. Cells* 94 (2010): 1528.

Polman H.A., A. Atwater. «Plasmonics for improved photovoltaic devices.» *Nature Materials* 9 (2010): 205-213.

Polman, K.R. Catchpole and A. «Plasmonic solar Cells.» *Opt. Express* 16 (2008): 21793-21800 .

Ramanathan K., G. Teeter, J. C. Keane, R. Noufi. *Thin Solid Films* 480–481 (2005): 499.

Ramasamy E., W. J. Lee, Y.L. Dong, and J. S. Song. «Nanocarbon counterelectrode for dye sensitized solar cells.» *Appl. Phys. Lett.* 90 (2007): 173103.

Ramuz M. P., M. Vosgueritchian, P. Wei, C. Wang, Y. Gao, Y. Wu. «Evaluation of Solution-Processable Carbon-Based Electrodes for All-Carbon Solar Cells.» *ACS Nano* 6, n. 11 (2012): 10384-10395.

Redfield, D. «Multiple-pass thin-film silicon solar cell.» *Applied Physics Letters* 25 (1974): 647.

Reilly T., J. van de Lagemaat, R. C. Tenent, A. J. Morfa, K. L. Rowlen. «Surface-plasmon enhanced transparent electrodes in organic photovoltaics.» *Appl. Phys. Lett.* 92 (2008): 243304.

Rothemberg G, P. Comte, M. Graetzel. «A contribution to the optical design of dye-sensitized nanocrystalline solar cells.» *Sol. Energy Materi. and Sol. Cells*, 1999: 321-336.

Roy-Mayhew J. D., D. J. Bozym, C. Punckt, and I. A. Aksay. «Functionalized Graphene as a Catalytic Counter electrode in Dye Sensitized Solar Cells.» *ACS Nano* 4 , n. 10 (2010): 6203–6211.

Sariciftci N. S., D. Braun, C. Zhang, V. I. Srdanov, A. J. Heeger, G. Stucky, F. Wudl. «Semiconducting Polymer-Buckminsterfullerene Heterojunctions: Diodes, Photodiodes, and Photovoltaic Cells.» *Appl. Phys. Lett.* 62 (1993): 585-587.

Schniepp H. C., J.L. Li, M. J. McAllister, H. Sai, M. Herrera-Alonso, D. H. Adamson, R. K. Prud'homme, R. Car, D. A. Saville, I. A. Aksay. «Functionalized Single Graphene Sheets Derived from Splitting Graphite Oxide.» *J. Phys. Chem. B* 110 (2006): 8535–8539.

Schott Solar, Albuquerque, . «EFG-Solar Cell Product Specification Sheet». 2010.

Scott G. D., D. M. Kilgour. «The density of random close packing of spheres.» *J. Phys. D: Appl. Phys.* 2 (1969): 863.

Shankar K., J. Bandara, M. Paulose, H. Wietasch, O.K. Varghese, G.K. Mor, T. J. La Tempa, M. Thelakkat, C.A. Grimes. «Highly efficient solar cells using TiO<sub>2</sub> nanotube

arrays sensitized with a donor-antenna dye.» *NanoLetters*, 2008: 1654-1659.

Shockley W., H. J. Queisser. *J. Appl. Phys.* 32 (1961): 510.

Sites J., J. Pan. *Thin Solid Films* 515 (2007): 6099.

Smestad G., C. A. Bignozzi, R. Argazzi. *Solar Energy Materials & Solar Cells* 32 (1994): 259.

Smestad, G. P. *Optoelectronics of Solar Cells*. Bellingham, WA: SPIE, 2002.

*Solar Cells: Operating Principles, Technology, and System Applications*,. Englewood Cliffs (USA) : Prentice Hall, 1982.

Spanggaard H., F. C. Krebs. *Sol. Energy Mater. Sol. Cells* 83 (2004): 125.

St.John, A.E. «Multiple internal reflection structure in a silicon detector wich is obtained by sandblasting.» *US Patent* 3, n. 487 (1969): 223.

St.John, A.E. *Multiple Internal Reflection Structure in a Silicon Detector which is obtained by Sandblasting*. U.S. Patent 3, 487, 223. 1969.

Staebler D. L., C. R. Wronski. *Appl. Phys. Lett.* (31), 1977: 292.

Steinberger, H. *Prog. Photovoltaics* 6 (1998): 99.

Stolt L., J. Hedström, J. Kessler, M. Ruckh, K.-O. Velthaus, H.-W. Schock. *Appl. Phys. Lett.* 62 (1993): 597.

Surek, T. «*J. Crist. Growth*.» 275 (2005): 292.

Suzuki K., M.Yamaguchi, M. Kumagai, S. Yanagida. «Application of Carbon Nanotubes to Counter Electrodes of Dye-Sensitized Solar Cells.» *Chem. Lett.* 32 (2003): 11238–11243.

T. W. Hamann, R. A. Jensen, A. B. F. Martinson, H. Van Ryswyk, J. T. Hupp. *Energy Environ. Sci.* 1 (2008): 66.

Tulloch, G. E. J. *Photochem. Photobiol. A* 164 (2004): 209.

Tung V. C., J.H. Huang, J.Kim, A. J. Smith, C.W. Chu, J. Huang. «Towards Solution Processed All-Carbon Solar Cells: A Perspective.» *Energy Environ. Sci.* 5 (2012): 7810–7818.

Tunisträ F., J.L. Koenig. «Raman Spectrum of Graphite.» *J.Chem Phys.* 53, n. 3 (1970): 1126-1130.

Usami, A. «Theoretical simulations of optical confinement in dye-sensitized nanocrystalline solar cells.» *Sol. Energy Mater. and Sol. Cells* , 2000: 73}83.

Usami, A. «Theoretical study of application of multiple scattering of light to a dye-sensitized nanocrystalline photoelectrochemical cell.» *Chemical Physics Letters* , 1997: 105-108.

Varghese O.K., M. Paulose, C.A. Grimes. «Long vertically aligned titania nanotubes on transparent conducting oxide for highly efficient solar cells.» *Nature Nanotechnology*, 2009: 592-597.

Wang Y., C. Di, Y. Liu, H. Kajiura, S. Ye, L. Cao, D.Wei, H. Zhang, Y. Li, K. Noda. «Optimizing Single-Walled Carbon Nanotube Films for Applications in Electroluminescent Devices.» *Adv. Mater.* 30, n. 23 (2008): 4442-4449.

Wolden, Colin A. J. *Vac. Sci. Technol. A* 29, n. 3 (May/Jun 2011): 30808-1.

Wolf, M. *Proceedings of the 14th IEEE Photovoltaics Conference*. San Diego, CA, 1980. 674.

Wu, X. *Sol. Energy* 77 (2004): 803.

Xu Y., H. Bai, G. Lu, C. Li, G. Shi. «Flexible Graphene Films Via the Filtration of Water-Soluble Noncovalent Functionalized Graphene Sheets.» *J. Am. Chem. Soc.* 130 (2008): 5856–5857.

Xue Y., J. Liu, H. Chen, R.Wang, D. Li, J. Qu,L. Dai. «Nitrogen-Doped Graphene Foams as Metal-Free Counter Electrodes in High-Performance Dye-Sensitized Solar Cells.» *Angew. Chem.* 51 (2012): 12124 –12127.

Yablonovitch, E. «Statistical ray optics.» *J. Opt. Soc. Am.* 72, n. 7 (1981).

Yang J., A. Banerjee, S. Guha. *Appl. Phys. Lett.* 70 (1997): 2975.

Yu D., E. Nagelli, F. Du, L. Dai. «Metal-Free Carbon Nanomaterials Become More Active than Metal Catalysts and Last Longer.» *J. Phys. Chem. Lett.* 1 (2010): 2165–2173.

Zaban A., S. Ferrere, B. Gregg. *Journal of Physical Chemistry B* 102 (1998): 6494.

Zhao W., B. W. Zhang, Y. Cao, X. Xiao, R. Yang 30, 304. *Journal of Functional Materials*, 1999.

Zhao X., B.T. T.Chu, B. Ballesteros, W. Wang, C. Johnston, J.M. Sykes, P.S. Grant P S.

«Spray deposition of steam treated and functionalized single-walled and multi-walled carbon nanotube films for supercapacitors.» *Nanotechnology* 20 (2009): 065605.

Zhou D., R. Biswas. «Photonic crystal enhanced light-trapping in thin film solar cells.» *J. Appl. Phys.* 103 (2008): 093102.

## LIST OF PUBLICATIONS

1. L.Giorgi, R.Giorgi, **S.Gagliardi**, E.Salernitano, T.Dikonimos, N.Lisi, M.F.De Riccardis and M. Alvisi “*Pt alloys on carbon nanostructures as electrocatalysts for direct methanol fuel cell*” *Advances in Science and Technology* Vol. 72 (2010) pp 277-282
2. N. Lisi, R. Giorgi, T. Dikonimos, E. Salernitano, **S. Gagliardi**, L. Giorgi, V. Contini, P. Morales “*Graphitized filament plasma enhanced CVD deposition of nanocrystalline diamond*” *Diamond & Related Materials* 19 (2010) 1382–1386
3. R.Giorgi, L.Giorgi, **S.Gagliardi**, E. Serra, M. Alvisi, M.A. Signore, and E. Piscopiello “*Platinum–Gold Nanoclusters as Catalyst for Direct Methanol Fuel Cells*” *Journal of Nanoscience and Nanotechnology* Vol. 11, 8804–8811, 2011
4. L. Giorgi, E.Salernitano, **S.Gagliardi**, Th. Dikonimos, R.Giorgi, N.Lisi, F. De Riccardis, V. Martina, “*Electrocatalysts for methanol oxidation based on platinum/carbon nanofibers nanocomposite*” *Journal of Nanoscience and Nanotechnology* 11 (10) , pp. 8812-8817, 2011
5. N. Lisi, R. Giorgi, M. Re, T. Dikonimos, L. Giorgi, E. Salernitano, **S. Gagliardi**, F. Tatti, “*Carbon nanowall growth on carbon paper by hot filament chemical vapour deposition and its microstructure*” *Carbon* 49 (6) , pp. 2134-2140, 2011
6. R.Giorgi, L.Giorgi, **S.Gagliardi**, E.Salernitano, M. Alvisi, T. Dikonimos, N. Lisi, E. Serra “*Nanomaterials-based PEM electrodes by combining chemical and physical deposition*” *Journal of Fuel Cell Science and Technology* 8 (4), art. no. 041004, 2011
7. R. D’Amato, M. Falconieri, **S. Gagliardi**, E. Popovici, E. Serra, G. Terranova and E. Borsella “*Synthesis of ceramic nanoparticles by laser pyrolysis: from research to applications*” *J. Analytical Appl. Pyrolysis*, submitted.
8. F. Toschi, A. Paladini, F. Colosi, P. Caffarelli, V. Valentini, M. Falconieri, **S. Gagliardi**, P. Santoro “*A multi-technique approach for the characterization of Roman fresco*” *Appl. Surf. Sci.* submitted
9. M.Falconieri, S. Gagliardi “*Experimental determination of light trapping in DSSC*” manuscript in preparatio

## CONFERENCE PRESENTATIONS

1. **S. Gagliardi**, L. Giorgi, N. Lisi, Th.Dikonimos, E. Salernitano, R. Giorgi, E. Dell'Orto  
*"Carbon Nanowalls as material for DSSC counter-electrodes"* HOPV 2010 Hybrid  
And Organic Photovoltaics Conference, 23-27 May 2010 Assisi, Italy
2. **S. Gagliardi**, L. Giorgi, R. Giorgi, N. Lisi, Th. Dikonimos, E. Salernitano *"DSSC  
counterelectrodes based on nanocarbons"* CIMTEC 2010 5<sup>th</sup> Forum on New Materials,  
13-18 June 2010 Montecatini Terme, Italy
3. L. Giorgi, R. Giorgi, **S. Gagliardi**, E. Salernitano, T. Dikonimos, N. Lisi, M. F. De  
Riccardis and M. Alvisi *"Pt alloys on carbon nanostructures as electrocatalysts for  
direct methanol fuel cell"* CIMTEC 2010 5<sup>th</sup> Forum on New Materials 13-18 June 2010  
Montecatini Terme, Italy
4. L.Giorgi, N.Lisi, Th.Dikonimos, **S.Gagliardi**, E.Salernitano, M. Re, M. Falconieri and  
R. Giorgi *"A nanostructured graphene based material: application to dye sensitized  
solar cell electrodes"* Graphene a one-day workshop on its properties and applications,  
15 July 2010 Portici, Italy
5. Th. Dikonimos, L.Giorgi, M.L. Grilli, **S.Gagliardi**, M.Falconieri, N. Lisi, P.Morales,  
E.Salernitano, G.Conte, R.Giorgi *"Growth, characterization and application in DSSC of  
titania nanotubes"* Materiali nanofasici X Convegno Nazionale, Bologna 6 - 8  
settembre 2011
6. **S.Gagliardi** *"Celle solari a colorante basate su nanotubi di titania"*, Nanoforum VII  
edizione, Roma 14-15 settembre 2011
7. Th.Dikonimos, M.Falconieri, **S.Gagliardi**, L.Giorgi, R.Giorgi, N.Lisi, P.Morales,  
E.Salernitano *"Titania nanotubes: growth and characterization"*, AISEM 2011, 7-9  
February 2011 Rome, Italy
8. R. Giorgi, Th. Dikonimos, M. Falconieri, **S. Gagliardi**, L. Giorgi, N. Lisi, P. Morales,  
L. Pilloni, and E. Salernitano *"Synthesis of graphene films on copper substrates by CVD  
from different precursors"*, Graphita, 15-18 May Gran Sasso National Laboratories,  
L'Aquila, Italy



9. **S. Gagliardi**, T. Dikonimos, M.L.Grilli , E. Salernitano, N. Lisi, M. Falconieri, L. Giorgi, G. Conte and R. Giorgi “*Titania nanotubes for DSC electrodes*” International Workshop on Advances in Photovoltaics and Photocatalysis, 21-22 July 2011 Technische Universität München, Germany
10. R.Giorgi, N. Lisi, T.Dikonimos, E.Salernitano, **S.Gagliardi**, M.Falconieri, M.Vittori, M.S. Sarto, A.Tamburrano, G.De Bellis, G.Messina, S. Santangelo, G. Faggio, V. Morandi, L.Ortolani “*Graphene based coatings*” Nanotech Italy 2011, 23-25 novembre Venezia
11. R.Giorgi, Th.Dikonimos, M.Falconieri, **S.Gagliardi**, N.Lisi, P.Morales, L.Pilloni, E.Salernitano “*Synthesis of graphene films on copper substrates by CVD of different precursors*”, GraphITA 2011 Proceedings, Springer, Luca Ottaviano and Vittorio Morandi Editors, 2012, p.109
12. T. Polichetti, L. Lancellotti, E. Massera, M. L. Miglietta, F. Ricciardella, S. Romano, O. Tari, S. Gnanapragasam and G. Di Francia, R. Giorgi, T. Dikonimos, N. Lisi, E. Salernitano, **S. Gagliardi**, M. Falconieri “*Graphene: different fabrication technologies for solid state devices*”Graphene 2012, April 10-13 2012, Brussels
13. G.Faggio, G. Messina, S. Santangelo, N.Lisi, Th.Dikonimos, E. Salernitano, **S.Gagliardi**, M.Falconieri and R.Giorgi “*Raman spectroscopy of graphene films grown on Cu foils by ethanol chemical vapor deposition*” International Conference on Diamond and Carbon Materials, Granada 3-6 september 2012
14. L. Lancellotti, N. Lisi, E. Bobeico, M. Della Noce, P. Delli Veneri, S. Del Sorbo, Th. Dikonimos, G. Di Francia, **S. Gagliardi**, R. Giorgi, A. Mittiga, T. Polichetti, F. Ricciardella “*Graphene based etherojunction solar cells*” ImagineNano Bilbao, April 23-26, 2013
15. **S. Gagliardi**, C. Paoletti, R. D’Amato, M. Falconieri “*Characterization of electron transport in titania electrodes for photoelectrochemical applications*” submitted to European Congress and Exhibition on Advanced Materials and Processes (Sevilla, September 8-13, 2013

## ACKNOWLEDGMENT

Special thanks to my tutors: Mauro Falconieri, Rossella Giorgi, Gennaro Conte.

ENEA UTTMAT-SUP group: N. Lisi, Th. Dikonimos, L. Giorgi, P. Morales, B. Rapone.

ENEA colleagues: E. Salernitano, F. Rondino, M. Moncada, E. Serra, I. Di Sarcina, F. Menchini, M.L. Grilli, R. Lo Presti.

S<sup>2</sup>DEL University Roma TRE group: in particular S. Spadaro.